Ultra-stable laser based on a cryogenic single-crystal silicon cavity

Von der Fakultät für Mathematik und Physik
der Gottfried Wilhelm Leibniz Universität Hannover
zur Erlangung des Grades

Doktor der Naturwissenschaften
– Dr. rer. nat. –

genehmigte Dissertation
von

Dipl.-Phys. Christian Hagemann
geboren am 23. Juni 1983 in Mölln

2013

Referent: Prof. Dr. Piet Schmidt

Korreferent: Prof. Dr. Ernst Rasel

Tag der Promotion: 8. Februar 2013

Zusammenfassung

Die besten Laser sind heute in ihrer Frequenzstabilität durch thermisches Rauschen der verwendeten Referenzresonatoren begrenzt. Diese Arbeit beschreibt die Entwicklung eines hochstabilen Lasersystems, das eine bislang unerreichte Kurzzeitstabilität durch die Verwendung eines kryogenen Referenzresonators aus einkristallinem Silizium ermöglicht.

Der Siliziumresonator wird bei einer Temperatur von 124 K betrieben, bei der die Wärmeausdehnung des Resonators minimal ist. Sowohl die geringe Betriebstemperatur als auch die mechanischen Eigenschaften von Silizium verringern durch thermisches Rauschen verursachte relative Längenänderungen des Resonators im Vergleich zu konventionell verwendeten Glasresonatoren um zwei Drittel auf etwa 4×10^{-17}. Geometrie und Aufhängung des Resonators wurden mit Hilfe der Finite-Elemente-Methode optimiert, um den Einfluss externer Beschleunigungen auf die Längenstabilität zu minimieren.

Ein aktiver Vibrationsisolationstisch unterdrückt die durch Seismik und Akustik erzeugten Schwingungen auf seiner Plattform. Die erforderliche kryogene Umgebung zur Kühlung des Siliziumresonators wurde durch einen eigens entwickelten vibrationsarmen Kaltgaskryostaten bereitgestellt. Ein Erbium-dotierter Faserlaser mit Emissionswellenlänge von 1.5 µm wurde auf eine Eigenfrequenz des Siliziumresonators stabilisiert. Um eine Verschlechterung der Frequenzstabilität durch Restamplitudenmodulation zu verhindern, wurde sie aktiv ausgeregelt.

Vergleichsmessungen mit zwei konventionellen Lasersystemen wiesen für den Siliziumresonator stabilisierten Laser eine Kurzzeitinstabilität von $mod\,\sigma_y = 1 \times 10^{-16}$ für Mittelungszeiten von 0,1 s bis 1 s nach. Weiterhin konnte gegen den stabileren der beiden Referenzlaser eine Linienbreite von etwa 50 mHz beobachtet werden.

Die Langzeitstabilität des Lasersystems wurde mithilfe eines optischen Frequenzkamms in Frequenzvergleichen mit primären und sekundären Frequenzstandards evaluiert. Gegen die Ytterbiumionenuhr der PTB wurde eine Frequenzinstabilität des Lasersystems von bis zu $\sigma_y(512\ s) \approx 2 \times 10^{-16}$ beobachtet. In Langzeitmessungen gegen eine Caesium-Fontänenuhr der PTB konnten zudem lineare Driftraten der Laserfrequenz von etwa 40 µHz/s über einen Zeitraum von drei Tagen erzielt werden. Die absolute Eigenfrequenz des Siliziumresonators am Punkt des minimalen thermischen Ausdehnungskoeffizienten änderte sich dabei über einen Zeitraum von 45 Tagen relativ um etwa $10^{-20}/s$, und unterschritt dabei die Drift des aktiven Wasserstoffmasers um etwa 50%.

Über den optischen Frequenzkamm wurde der auf einen Glasresonator vorstabilisierte 698 nm Uhrenlaser der Strontiumgitteruhr der PTB an den in dieser Arbeit entwickelten Infrarotlaser angebunden. So konnte der $^1S_0 - ^3P_0$ Uhrenübergang von ^{87}Sr mit einer Fourier-limitierten Linienbreite von 1,5 Hz aufgelöst werden. Weiterhin ließ sich aus zwei alternierenden Stabilisierungen des Uhrenlasers auf den

Uhrenübergang die Stabilität der Uhr mit $\sigma_y(\tau) = 4,5 \times 10^{-16}/\sqrt{\tau/\mathrm{s}}$ abschätzen, ein Wert, der bisher nur am amerikanischem NIST erreicht wurde.

Prinzipiell sind Möglichkeiten der Verbesserung der Stabilität vorhanden, da die aktuelle Frequenzstabilität des Siliziumresonator-stabilisierten Lasers noch nicht durch thermisches Rauschen begrenzt ist. Die erforderlichen Maßnahmen zum Erreichen des thermischen Rauschlimits über weite Zeitskalen werden im Ausblick dieser Arbeit diskutiert.

Stichworte:

- Frequenzstabilisierung
- Optischer Referenzresonator
- Thermisches Rauschen
- Optische Uhren

Abstract

State-of-the-art ultra-stable lasers are limited by the thermal noise of the employed reference resonators. This work describes the development of a laser system with so far unreached short-term stability, enabled by the use of a cryogenic reference resonator machined from single-crystal silicon.

The silicon cavity is operated at a temperature of 124 K, where the thermal-expansion of the resonator is minimized. The low temperature and the mechanical properties of crystalline silicon reduce fractional instabilities of the resonator length originating from thermal noise to a level of 4×10^{-17}. Geometry and support of the resonator were optimized by means of finite element analysis to minimize the impact of external accelerations to the length stability.

Seismic and acoustic accelerations on the setup are suppressed by an active vibration isolation platform. A low-vibrational cryostat that employs cold gas as coolant was developed for operating the silicon cavity at 124 K. An erbium-doped fiber laser emitting laser radiation at 1.5 µm was stabilized to an eigenfrequency of the resonator and residual amplitude modulation was actively cancelled.

In a frequency comparison with two conventional laser systems, the laser stabilized to the silicon cavity provided short-term instabilities of $mod\,\sigma_y = 1 \times 10^{-16}$ for averaging times of 0.1 s – 1 s. Moreover, the beat frequency with the most stable reference laser showed a linewidth of 50 mHz.

The long-term performance of the laser system has been evaluated from frequency comparisons with primary and secondary frequency standards available at PTB, utilizing an optical frequency comb. In the comparison with the ytterbium ion clock at PTB, a frequency instability of $\sigma_y(512\ s) \approx 2 \times 10^{-16}$ has been observed. Long-term measurements against a cesium fountain clock at PTB have revealed a linear drift of about 40 µHz/s in a time interval of three days. The absolute value of the silicon cavity's resonance frequency at the temperature of zero expansion showed a linear drift below $10^{-20}/s$, which was a factor of 2 below the drift of the active hydrogen maser.

The clock laser at 698 nm of PTB's strontium lattice clock is prestabilized to a conventional glass resonator. Utilizing the optical frequency comb as transfer oscillator, this laser was locked to the silicon cavity stabilized-laser. This way, the $^1\mathrm{S}_0 - ^3\mathrm{P}_0$ clock transition of ^{87}Sr was resolved with a Fourier-limited linewidth of 1.5 Hz. Alternating two independent stabilizations of the clock laser frequency to the clock transition, clock instabilities were estimated to average down with $4.5 \times 10^{-16}/\sqrt{\tau/\mathrm{s}}$, competing with the best reported values from NIST.

As the silicon-cavity laser is not yet limited to the thermal noise floor of the cavity, there is still room for further improvements. The required steps to achieve thermal noise limited laser instabilities of $\sigma_y = 4 \times 10^{-17}$ over a wide range of averaging times are discussed.

Keywords:

- Laser frequency stabilization
- Optical reference cavity
- Thermal noise
- Optical clocks

List of abbreviations

AOM	Acousto-optic modulator
ADEV	Allan deviation
ASE	Amplified spontaneous emission
AVAR	Allan variance
CTE	Coefficient of thermal expansion
DC	Direct current
DDS	Direct digital synthesizer
EDFA	Erbium-doped fiber amplifier
EOM	Electro-optic modulator
FDT	Fluctuation-dissipation theorem
FS	Fused silica
FSR	Free spectral range
FWHM	Full width at half maximum
MADEV	Modified Allan deviation
MAVAR	Modified Allan variance
MOT	Magneto-optical trap
NIST	National Institute of Standards and Technology
PTB	Physikalisch-Technische Bundesanstalt
RBW	Resolution bandwidth
RF	Radio frequency
SNR	Signal-to-noise ratio
PDH	Pound-Drever-Hall
ppm	parts per million
PSD	Power spectral density
TEM	Transverse electromagnetic mode
TCH	Three-cornered hat
ULE	Ultra-low expansion
VCO	Voltage-controlled oscillator

Contents

Chapter 1

Introduction

Since the invention of the Michelson interferometer more than a century ago [1], optical interferometers are the working horses for measurements of highest precision. Employed in various fields on the forefront of fundamental research such as optical frequency standards [2–4], gravitational wave detection [5, 6], quantum optomechanics [7, 8], or fundamental tests of physics [9, 10], these devices contribute to a better understanding of physical phenomena, opening new frontiers in science and applications, motivating further explorations and discoveries.

One of the most precise interferometers are Fabry-Pérot-interferometers which have become a standard tool for state-of-the-art laser stabilization, locking the output frequency of a laser to a resonance of a rigid Fabry-Pérot cavity. Ultra-stable lasers are indispensable tools for optical atomic clocks or ultra-high resolution spectroscopy, and improvements of the frequency stability will enable even more precise measurements, for example for the investigation of the temporal variation of the fine-structure constant $\dot{\alpha}/\alpha$ [11]. A milestone in laser stabilization was reported in 1999, where a cavity-stabilized laser demonstrated sub-Hertz linewidths and fractional frequency instabilities of 3×10^{-16} [12]. As the achievable frequency stability is determined by the length stability of the reference resonator, much effort in isolation of external noise sources that affect the length, i.e. seismic noise or temperature fluctuations, was necessary to reduce length fluctuations to 10^{-15} m, the diameter of a proton! In the past decade – striving for even lower instabilities – research has focused on making reference cavities insensitive to environmental perturbations by design. This led to more robust, compact, and even transportable systems [13, 14]. However, these improvements were not accompanied by a reduction of laser instability, which still remains on a level of $2 \ldots 3 \times 10^{-16}$ [15]. It has been shown by Numata et al. that length-fluctuations resulting from intrinsic Brownian motion fundamentally limit the stability of state-of-the-art ultra-stable lasers, with the largest contribution from the high-reflection coating.

Coating thermal noise arising from Brownian motion has been investigated in great detail in context with gravitational wave antennas [16, 17], and its reduction has become subject of intense research. Possible ways to reduce coating thermal noise include modifications of standard coating technology [18,19], alternative coating materials [20, 21], or even coatingless, diffractive mirror structures [22]. So far,

the improvements have been either moderate or low-noise coatings do not yet satisfy the demands for the construction of high-finesse optical cavities.

Hence, alternative strategies are pursued to lower the thermal noise floor of optical reference cavities. First of all, as the coating thermal noise does not rely on the length of a resonator, its impact on the fractional frequency noise of a reference cavity can be reduced increasing the resonator length. A larger spot size of the laser field that probes the mirror surface leads to a better averaging of the thermal noise, reducing its influence. It has also been shown in [23], that a larger Young's modulus of the mirror substrates reduces the coating thermal noise.

The most promising approaches that potentially lower thermal noise below fractional frequency instabilities of 1×10^{-16} employ ultra-long ULE-glass resonators with spacer lengths approaching half a meter and mirror configurations with large mode sizes. However, an even further reduction of thermal noise in conventional room-temperature resonators does not seem promising.

Thus, to open up an avenue for large improvements, a reduction of the operating temperature seems inevitable. This implicates a rejection of the well established resonator technology based on amorphous glass materials, as these are not suitable for cryogenic operation. Even though stimulated by another motivation – in order to perform a modern Michelson-Morley experiment [24] – a cryogenic sapphire cavity with for that time unreached laser stabilities was demonstrated as early as 1997 [25]. The crystalline cavity was operated at a temperature of 4.2 K, where the coefficient of thermal expansion of sapphire is sufficiently low to enable extraordinary low frequency drifts of the resonance of 2.7 kHz over six months [26] – a benchmark which is still not beaten by any conventional glass resonator which encounter aging-related frequency drifts. Even earlier, Richard and Hamilton investigated the suitability of silicon for constructing a cryogenic cavity [27]. Their conclusion was that "...this technique appears to have true potential for producing a highly stable relative frequency standard". However, they recognized that "There was some increased noise..., and this could be due to the presence of a cryogenic bath.". Indeed, cooling-related vibrations deteriorate the resonator stability, and consequently cryogenic cavities have not been competitive with conventional resonators for more than one decade.

As already included in the work of Richard and Hamilton, silicon is one of the rare natural materials that provides zero-crossings in its coefficient of thermal expansion, which are at 18 K and 123 K [28]. Thus, a large insensitivity of the length to temperature fluctuations can be achieved operating a resonator made from silicon at one of these temperatures. As vibrations are expected to be less severe if cooling all the way down to 4 K can be avoided, operating a cavity machined from silicon at the higher zero-crossing temperature seems to be an attractive option to realize an ultra-low noise reference cavity.

This work describes the development and utilization of such a cryogenic reference resonator machined from a silicon single-crystal, which has enabled laser instabilities below the thermal noise limit of an equivalent glass resonator based laser

system. Operated at the higher zero-crossing of its coefficient of thermal expansion, the low temperature and the superior mechanical properties of silicon reduce the thermal noise floor to an estimated value of $\sigma_y \approx 4 \times 10^{-17}$.

Geometry and support of the resonator were optimized by means of finite element analysis which reduced the measured vibration-induced fractional length changes to less than $10^{-11}/(\mathrm{m\,s^{-2}})$ in each direction. An actively controlled vibration isolation platform suppresses seismic and acoustic accelerations on the table to a level of $10^{-6}\ \mathrm{m\,s^{-2}\,Hz^{-1/2}}$. A low-vibrational gas-based cryostat has been implemented that provides a cryogenic environment for the silicon cavity without significant contributions to the seismic noise floor.

An erbium-doped fiber laser emitting laser radiation of wavelength 1.5 µm was stabilized to an eigenfrequency of the resonator via the Pound-Drever-Hall technique. Residual amplitude modulation from the phase modulator is actively suppressed.

In a frequency comparison with two conventional laser systems the silicon cavity stabilized laser showed short-term instabilities of $mod\,\sigma_y = 1 \times 10^{-16}$ for averaging times from 0.1 s – 1 s. Moreover, the beat frequency with the most stable reference lasers showed a linewidth of 49(4) mHz. The long-term performance of the laser system has been evaluated from frequency comparisons with primary and secondary frequency standards available at PTB, utilizing an optical frequency comb. In the comparison with the ytterbium ion clock at PTB, a frequency instability of $\sigma_y(512\ s) \approx 2 \times 10^{-16}$ has been observed. Long-term measurements against a cesium fountain clock at PTB have revealed a linear drift of about 40 µHz/s in a time interval of three days. The absolute value of the silicon cavity's resonance frequency at the temperature of zero expansion showed a linear drift below $10^{-20}/s$, which was a factor of 2 below the drift of the active hydrogen maser.

Utilizing an optical frequency comb as transfer oscillator, the glass resonator based clock laser (laser wavelength: 698 nm) of PTB's strontium lattice clock was stabilized to the highly stable infrared laser. The $^1\mathrm{S}_0 - {}^3\mathrm{P}_0$ clock transition of ^{87}Sr was resolved to a Fourier-limited linewidth of 1.5 Hz. Alternating two independent stabilizations of the clock laser frequency to the clock transition, clock instabilities of a single-clock are estimated to average down with $4.5 \times 10^{-16}/\sqrt{\tau/\mathrm{s}}$.

This thesis is organized as follows:

- Chapter 2 will provide the basics of laser stabilization to optical resonators. The reader will be introduced to the required equations and measures employed for the characterization of an oscillator's stability. After that, a short introduction to optical resonators is given followed by a brief presentation of the concept behind the Pound-Drever-Hall technique which is utilized for laser stabilization in this work.

- Chapter 3 will describe the development of the ultra-low noise optical resonator machined from single-crystal silicon. As the focus of this work was to demonstrate the usefulness of a cryogenic optical cavity to reduce thermal

noise this topic will be discussed intensively. It will be shown that crystalline silicon provides further unique properties that make it a suitable material to construct an ultra-stable reference cavity. Typical considerations with respect to cavity design that had to be done for the realization of the silicon cavity are presented, closing with a description of the manufacturing process. Finally, the results of initial measurements on the cavity linewidth will be presented.

- Chapter 4 describes setup of the laser system and gives an evaluation of crucial noise sources that affect the frequency stability of a silicon cavity locked laser. First, a detailed description of the low-vibrational cryostat which has been set up to operate the silicon cavity at its temperature of minimal thermal expansion is given. Second, the optical and electronic setup employed for laser stabilization is described. Both sections will also discuss the technical challenges that have been mastered to achieve the obtained laser performance, as well as point out the remaining effects that might still compromise the laser stability.

- Chapter 5 presents the obtained results for the laser stabilized to the silicon cavity. First, the results of a measurement campaign to evaluate the short-term stability of the silicon cavity stabilized laser system in a three-cornered hat comparison with two conventional room-temperature cavity stabilized laser systems are presented. The second part deals with the evaluation of the long-term instability of the silicon oscillator.

- Chapter 6 describes how optical frequency standards can benefit from the performance of the silicon cavity stabilized laser. After a short introduction to optical clocks it is described how a femtosecond frequency comb was utilized to transfer the stability of the silicon system to improve the stability of a spectrally distant optical clock. The results of such a stability transfer are presented in the end of this chapter.

- A conclusion and outlook will complete this work, giving an overview on the remaining challenges required to achieve thermal noise limited operation of the silicon cavity stabilized laser system. Furthermore, the potential of the silicon technology for further improvements is discussed.

Chapter 2

Laser stabilization to optical resonators

State-of-the-art ultra-stable lasers are stabilized to resonances of high-finesse optical cavities and the ultimate limit of achievable laser stability is determined by the fractional length instability of the reference resonator

$$\frac{\Delta\nu}{\nu} = -\frac{\Delta L}{L} \,. \tag{2.1}$$

This chapter will provide the basics of laser stabilization to optical reference resonators, giving a brief introduction to optical resonators, the commonly employed Pound-Drever-Hall stabilization technique, and characterization and evaluation of the frequency stability of a highly-stable oscillator. For more information on optical resonators the reader is referred to [29, 30]. A detailed introduction to the Pound-Drever-Hall technique is given in [31].

2.1 Optical reference resonators

High-precision laser stabilization commonly employs optical reference resonators in a Fabry-Pérot interferometer geometry, consisting of a pair of highly reflective mirrors facing each other and separated by distance L. Consider monochromatic light of wavelength λ that enters the resonator through one of the mirrors. The electro-magnetic wave will exhibit a phase shift

$$\Delta\phi = 2\pi\frac{2L}{\lambda} = 2\pi\frac{2L\nu}{c} \tag{2.2}$$

after each round-trip of length $2L$, where c denotes the speed of light and $\nu = c/\lambda$ is the frequency of the coupled-in light. The cavity is said to be on resonance for input frequencies

$$\nu_q = q\frac{c}{2L}, \quad q = 1, 2, 3, \ldots \tag{2.3}$$

where the cavity phase shift $\Delta\phi$ corresponds to a multiple of 2π and all partial waves with different number of round-trips interfere constructively at the output

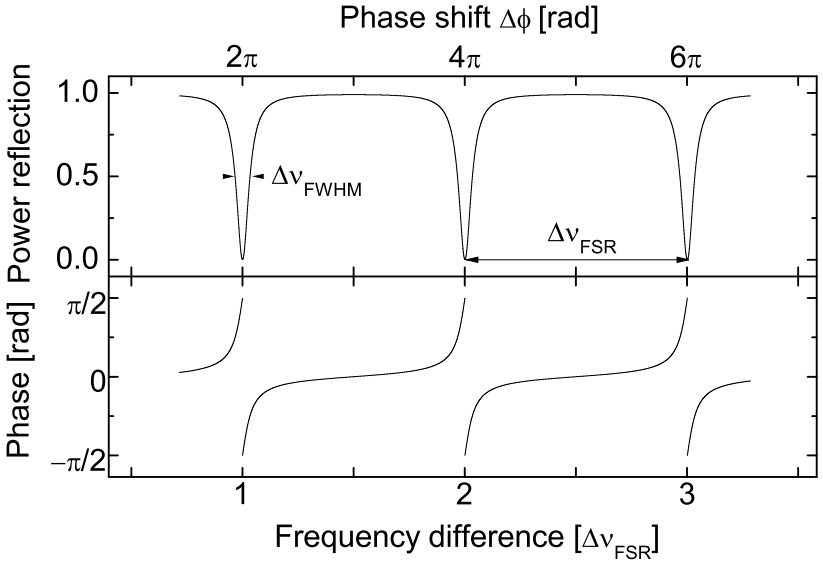

Figure 2.1: Power reflection coefficient $|\mathfrak{r}_{\text{FP}}|^2$ and phase of the reflected light from an loss-less optical resonator as function of the round-trip phase-shift $\Delta\phi$ and frequency difference $\Delta\nu_{\text{FSR}}(\Delta\phi)$. If the incident light is resonant, the phase of $\mathfrak{r}_{\text{FP}}$ shows a discontinuity as the reflected light becomes zero. For a detuning from resonance, the reflected light exhibits a phase shift with opposite sign which is dependent of the direction of the detuning.

mirror. The following formulas provide a description of the transmitted and reflected field,E_t,E_r, as function of the cavity phase shift [32]

$$E_t(\Delta\phi) = \frac{t_1 t_2 e^{i\Delta\phi/2}}{1 - r_1 r_2 e^{i\Delta\phi}} E_i \tag{2.4}$$

$$E_r(\Delta\phi) = \frac{r_1 - r_2(r_1^2 + t_1^2)e^{i\Delta\phi}}{1 - r_1 r_2 e^{i\Delta\phi}} E_i \ , \tag{2.5}$$

where t_1, r_1 (t_2, r_2) denote the amplitude transmission and reflection coefficient of the input (output) mirror. $\mathfrak{r}_{\text{FP}} := E_r(\Delta\phi)/E_i(\Delta\phi)$ defines the amplitude reflection coefficient of the Fabry-Pérot interferometer. Fig. 2.1 shows the dependency of the reflected power $|\mathfrak{r}_{\text{FP}}|^2$ and phase of the reflected light wave as function of the round-trip phase shift $\Delta\phi$. For a symmetrical loss-less cavity ($t_1 = t_2 = t$, $r_1 = r_2 = r$, $t^2 + r^2 = 1$) the power reflected from the resonator drops to zero, while the transmitted power $1 - |\mathfrak{r}_{\text{FP}}|^2$ is maximized and equals the intensity of the incident beam.

The frequency difference between two adjacent resonances corresponding to $\Delta\phi = 2\pi$ is the so-called free spectral range (FSR)

$$\Delta\nu_{\text{FSR}} = \frac{c}{2L} \ . \tag{2.6}$$

The full width at half-maximum $\Delta\nu_{\text{FWHM}}$ is defined as the linewidth where the intensity is reduced by 50%. The line profile is a Lorentzian for high reflectivities $r_1^2, r_2^2 \to 1$. The linewidth depends on the photon lifetime τ_c inside the resonator, thus narrows with increasing resonator length. The ratio of the FSR and the

linewidth, denoted as finesse $\mathcal{F}$, represents a length-independent quantity which relies exclusively on the mirror reflectivities according to [33]

$$\mathcal{F} := \frac{\Delta\nu_{\text{FSR}}}{\Delta\nu_{\text{FWHM}}} = \frac{\pi\sqrt{r_1 r_2}}{1 - r_1 r_2} \,. \tag{2.7}$$

The previous considerations assumed hypothetic plane waves propagating along the optical axis of an idealized resonator that provides two parallel and plane finite sized mirrors. However, plane waves can not describe any wave occurring in reality, since they have an infinite transverse extent. Furthermore, a light beam would exit the resonator after a finite number of round-trips leading to unwanted losses.

A realistic resonator employs spherical mirrors (with radii R_1, R_2) and is stable if the condition [29]

$$0 < g_1 g_2 < 1 \,, \tag{2.8}$$

is satisfied, where $g_i := 1 - \frac{L}{R_i}$ $(i = 1, 2)$. Consequently, at least one concave mirror is employed in practical resonators. Length and radii of curvature R_1, R_2 determine the possible spatial field distributions of the intra-cavity field, of which the fundamental mode is a Gaussian with intra-cavity focal beam waist w_0[1] and Rayleigh length z_0 [29]

$$w_0^2 = \frac{\lambda z_0}{\pi}, \quad z_0^2 = \frac{L(R_1 - L)(R_2 - L)(R_1 + R_2 - L)}{(R_1 + R_2 - 2L)^2} \,. \tag{2.9}$$

Besides the fundamental mode there exists a whole family of higher-order transverse electromagnetic modes (TEM$_{mn}$, $m, n = 0, 1, 2, \ldots$). The spatial field distribution of these theses modes can be described with Hermite-Gaussian functions $H_{m,n}$ and is given for a wave propagation along the z-axis and transverse coordinates x, y by [29]

$$\begin{aligned} E_{mn}(x, y, z) &= E_0 \frac{w_0}{w(z)} H_m\left(\frac{\sqrt{2}x}{w(z)}\right) H_n\left(\frac{\sqrt{2}y}{w(z)}\right) e^{-\frac{x^2+y^2}{w(z)^2}} e^{-i\left[kz - (1+n+m)\arctan\left(\frac{z}{z_0}\right) + \frac{k(x^2+y^2)}{2R(z)}\right]}, \\ w(z) &= w_0\sqrt{1 + \left(\frac{z}{z_0}\right)^2}, \quad R(z) = z\left(1 + \left(\frac{z_0}{z}\right)^2\right) \,. \end{aligned} \tag{2.10}$$

Here, E_0 is the electric field amplitude, $k = 2\pi/\lambda$ is the wave propagation constant, and $w(z)$ and $R(z)$ denote beam size (radius) and radius of curvature of the wavefront at position z, with the beam waist w_0 chosen to be at $z = 0$. With respect to a plane-parallel Fabry-Pérot with multiple eigenfrequencies of $\nu_{\text{FSR}} = c/2L$, the eigenfrequencies are upshifted in addition according to [29]

$$\nu_{mnq} = \Delta\nu_{\text{FSR}}\left(q + \frac{(m + n + 1)}{\pi}\arccos\sqrt{g_1 g_2}\right) \,. \tag{2.11}$$

[1]The beam waist w gives the distance from the beam center where the electric field amplitude has fallen to 1/e of its maximum value.

For an efficient coupling of laser light into the resonator, the beam parameters of the incident beam need to match the field distribution of the resonator mode. The coupling efficiency can be calculated from

$$\eta = \frac{\left| \int_{-\infty}^{\infty} \int_{-\infty}^{\infty} E_i E_{mn}^{*} \, \mathrm{d}x \, \mathrm{d}y \right|^2}{\int_{-\infty}^{\infty} \int_{-\infty}^{\infty} |E_i|^2 \, \mathrm{d}x \, \mathrm{d}y \int_{-\infty}^{\infty} \int_{-\infty}^{\infty} |E_{mn}|^2 \, \mathrm{d}x \, \mathrm{d}y} \, . \tag{2.12}$$

Employing single-mode laser sources with Gaussian beam profile, $\eta \approx 1$ can be achieved locking to the fundamental TEM_{00}-mode of the optical cavity. In this work, however, the linewidth of fundamental resonator mode was significantly smaller than that of higher-order modes, and the same incident field has been used to couple to the TEM_{01}-mode (see Sec. 3.3.4). From Eq. 2.12 one finds that the maximum coupling efficiency is 37% for an incident field that is transversely offset by $w(z)$ at the input mirror position.

2.2 Laser stabilization to optical resonators

There exist various methods to stabilize a laser to an optical cavity, most simply locking the laser frequency to the side of a transmission fringe. The Hänsch-Couillaud-technique [34] uses a polarization spectroscopic method in combination with a polarization dependent resonance of the cavity. However, these techniques suffer from low-frequency noise in the DC detection, i.e. residual intensity noise from the laser and technical noise in the photo detector, which compromises the locking performance. A method that has prevailed against this shortcoming is the Pound-Drever-Hall technique [35], as it circumvents DC noise by a detection in the radio-frequency band.

As depicted in Fig. 2.1, the phase shift of a field reflected from a resonator shows an approximately linear dependency within the cavity linewidth. Measuring this phase shift in the appropriate quadrature, one would obtain a linear frequency discriminant that can be used to steer the optical frequency of the laser to the center of a resonator eigenmode. As there are no detectors that have the ability to directly measure the phase of light, an indirect determination of the phase shift has to be realized. The phase of the incident light field is modulated with a radio frequency (RF) Ω_m and modulation depth β

$$E_i(t) = E_0 e^{i(\omega t + \beta \sin(\Omega_m t))} \, , \tag{2.13}$$

e.g. by employing an electro-optic modulator to generate sidebands with frequencies $\omega \pm n\Omega_m$, where $\omega = 2\pi\nu$. For modulation depth $\beta < 1$ most of the power is concentrated in the carrier and first-order sidebands and Eq. 2.13 can be written as

$$E_i(t) \approx E_0[J_0(\beta)e^{i(\omega t)} + J_1(\beta)e^{i(\omega+\Omega_m)t} - J_1(\beta)e^{i(\omega-\Omega_m)t}] \, , \tag{2.14}$$

where $J_n(\beta)$ is the Bessel function of n-th order. If the carrier frequency is within the resonator linewidth and Ω_m is chosen such that the sidebands are not, carrier light

is coupled into the resonator while the sidebands are directly reflected at the incident mirror. The sidebands provide a phase reference for carrier light that leaks out of the cavity if there is a detuning Δf from the center frequency of the resonance. The carrier phase shift induces an imbalance in the interference with the sidebands[2], leading to a beat component in the reflected light intensity that oscillates at the modulation frequency Ω_m [31]

$$P_r \approx 4P_c \left(\frac{\Delta f}{\Delta\nu_{\text{FWHM}}}\right)^2 + 2P_s - 8\sqrt{P_c P_s}\frac{\Delta f}{\Delta\nu_{\text{FWHM}}}\sin\Omega_m t - 2P_s\cos 2\Omega_m t\ , \tag{2.15}$$

where $P_c = J_0(\beta)^2 P_0$ and $P_s = J_1(\beta)^2 P_0$ denote the power in the carrier and each sideband. The amplitude and sign of this frequency is a function of the detuning Δf. If this signal is fed to a mixer and demodulated with a phase-matched signal of the same frequency Ω_m, one will obtain a frequency discriminant signal with approximately linear slope $\mathcal{D}$ within $-\Delta\nu_{\text{FWHM}}/2 < \Delta f < \Delta\nu_{\text{FWHM}}/2$

$$\epsilon(\Delta f) \approx \mathcal{D}\Delta f = \frac{-8P_0 J_0(\beta)J_1(\beta)}{\Delta\nu_{\text{FWHM}}}\Delta f\ , \tag{2.16}$$

that can be utilized for frequency control. It is important to note that the control bandwidth obtained by the PDH technique is not restricted to the cavity linewidth. While the error signal is proportional to frequency fluctuations of the laser that are smaller than the half-width of the resonance, it is proportional to phase fluctuations of the laser that occur at Fourier frequencies higher than the half-width of the resonance. This effect results from the leakage field interfering with the off-resonant carrier light. Quantitatively, the error signal needs to be multiplied with a single-pole low-pass filter with corner frequency at the cavity half-width.

In principle, the PDH technique enables a shot-noise limited stabilization of the laser to the resonator. The optical shot noise on the detector from the reflected signal has a flat spectrum with density

$$S_P = 2h\nu P_r \tag{2.17}$$

and can be converted to a white frequency noise density by

$$S_\nu^{(\text{shot})} = \frac{S_P}{\mathcal{D}^2} = \frac{h\nu\Delta\nu_{\text{FWHM}}^2 P_r}{32(P_0 J_0(\beta)J_1(\beta))^2}\,. \tag{2.18}$$

$S_\nu^{(\text{shot})}$ is minimized for the ideal case when $P_r = 2J_1(\beta)^2 P_0$ (only the sidebands are reflected and S_P is minimum) and an optimal modulation depth of $\beta = 1.08$ where $\mathcal{D}$ is maximum. With typical parameters of this work ($\nu = 194\times10^{12}\,\text{Hz}$, $\Delta\nu_{\text{FWHM}} = 3.1\,\text{kHz}$, $\beta = 1.08$, $P_0 = 130\,\mu\text{W}$, $P_r/P_0 = 0.8$) a shot-noise floor of $S_\nu^{(\text{shot})} = 2\times10^{-9}\,\text{Hz}^2/\text{Hz}$ is expected. With the relation $\delta\nu = S_\nu\pi$ (see Sec. 2.3), one finds that the cavity lock is limited by the white shotnoise floor below linewidth of 1 μHz. In practice, technical noise that arise from the electronics (e.g. RF pickup in the cables, DC noise subsequent to the demodulation) or the optics (e.g. residual amplitude modulation) limit the locking performance (see Sec. 4.3).

[2]Note that even if the the carrier light is perfectly resonant, there will be carrier light in the reflection due to intra-cavity losses or imperfect mode-matching in practice. However, this is no substantial limitation, as the phase-shift is zero.

2.3 Characterization of frequency instability

Consider an ideal oscillator $E(t) = E_0 \sin(2\pi\nu_0 t)$ with maximum amplitude E_0 and frequency ν_0. If amplitude $E(t)$ and phase $\phi(t) = 2\pi\nu_0 t$ are known for a specific time t both can be predicted for any moment in the future. However, in real oscillators physical or technical noise processes are present which cause fluctuations $\Delta E(t)$ and $\Delta\phi(t)$ of amplitude and phase, respectively. Consequently, both the amplitude and the phase of the oscillator can only be predicted within some uncertainty.

The frequency of an oscillator is basically the time-derivative of the phase and the instantaneous frequency of an oscillator is given by

$$\nu(t) = \nu_0 + \frac{1}{2\pi}\frac{d\phi(t)}{dt} \ . \tag{2.19}$$

It differs from the nominal frequency ν_0 of an ideal oscillator by

$$\Delta\nu(t) = \nu(t) - \nu_0 = \frac{1}{2\pi}\frac{d\phi(t)}{dt} \ . \tag{2.20}$$

In frequency metrology a variety of local oscillators is available, with driving frequencies ranging from the microwave to the visible regime. To compare the performance of theses oscillators one normalizes the frequency deviations to the nominal operation frequency ν_0

$$y(t) = \frac{\Delta\nu(t)}{\nu_0}. \tag{2.21}$$

The fractional frequency deviations can be evaluated both in the frequency and in the time domain. Fast frequency fluctuations are usually described in the frequency domain, typically by determination of the power spectral density (PSD) of phase fluctuations $S_\phi(f)$, from which the PSD of (fractional) frequency fluctuations $S_\nu(f)$[3] ($S_y(f)$) can be derived from the relations

$$S_y(f) = \frac{1}{\nu_0^2} S_\nu(f) = \left(\frac{f}{\nu_0}\right)^2 S_\phi(f) \ . \tag{2.22}$$

For white frequency noise $S_\nu(f)$ =const., the linewidth of the oscillator is a Lorentzian with FWHM of [33]

$$\Delta\nu = \pi S_\nu \ . \tag{2.23}$$

In general, the frequency noise spectrum can be approximated by a superposition

$$S_y(f) = \sum_{\alpha=-2}^{2} h_\alpha f^\alpha \ . \tag{2.24}$$

The integral exponent α is characteristic for well-known types of noise classified in Tab. 2.1. Observing a distinct f^α-dependency in a certain frequency interval, this

[3] $S_\nu(f)$ is the commonly shortened notation of $S_{\Delta\nu}(f)$.

may allow the identification of the origin of the noise and thus its reduction or elimination.

In the time domain the fractional frequency instability is usually characterized by the (relative) Allan variance (AVAR) (or its square root, the Allan deviation (ADEV)) defined as

$$\sigma_y^2(\tau) = \frac{1}{2}\left\langle (\overline{y}_{i+1} - \overline{y}_i)^2 \right\rangle \ . \tag{2.25}$$

The AVAR gives the average squared difference between successive readings of the average frequency deviation, $\overline{y}_{i+1}, \overline{y}_i$, with sample interval τ. The advantage of this two-sample variance is that it converges on all types of noise listed in Tab. 2.1 in contrast to the standard variance which would diverge for random walk frequency-noise or a linear frequency drift. In practice, the AVAR is often derived from a frequency measurement employing frequency counters. The most simple formula to estimate the AVAR from N frequency readings is

$$\sigma_y^2(\tau) = \frac{1}{2(N-1)} \sum_{i=1}^{N-1} (\overline{y}_{i+1} - \overline{y}_i)^2 \ . \tag{2.26}$$

For longer averaging times $\tau = n\tau_0$, the classic AVAR estimator just sums up the frequency data with single use of each integral. To provide a higher confidence of the stability estimate, especially for long averaging times, the overlapping Allan variance (OAVAR) is often used, which makes maximum use of a data set by forming all possible overlapping samples for each averaging time τ [36]

$$\sigma_y(\tau)^2 = \frac{1}{2n^2(N-2n+1)} \sum_{j=1}^{N-2n+1} \left\{ \sum_{i=j}^{j+n-1} (\overline{y}_{i+n} - \overline{y}_i) \right\}^2 \ . \tag{2.27}$$

Similarly as observed in the frequency-domain, the particular noise contributions show a characteristic dependency on the averaging time τ (see Tab. 2.1). However, the AVAR fails to distinguish between flicker phase noise and white phase noise ($\propto \tau^{-2}$). The so-called modified Allan variance (MAVAR), $mod\ \sigma_y^2(\tau)$, introduced by Allan and Barnes [37] provides a different characterization of frequency stability suitable to distinguish between high-frequency noise. In the definition of [36] it reads

$$mod\ \sigma_y^2(\tau) = \frac{1}{2n^4(N-3n+2)} \sum_{j=1}^{N-3n+2} \left\{ \sum_{i=j}^{j+n-1} \left(\sum_{k=i}^{i+n-1} (\overline{y}_{k+n} - \overline{y}_k) \right) \right\}^2 \ . \tag{2.28}$$

An additional phase averaging operation leads to a lower dependency to white phase noise ($\propto \tau^{-3}$) while the slope for flicker phase noise is unaffected (see Tab. 2.1). For example, this can be useful to determine the noise floor of an oscillator if it is covered by white phase noise. Although the dependency on τ is not changed for all other noise types, the additional averaging process has some impact on the prefactor values as shown in Tab. 2.1 [38]. Thus, care has to be taken when comparing the

Table 2.1: Relationship between PSD, AVAR, and MAVAR for characteristic noise types (taken from [38]). f_H denotes the high frequency cutoff of the measurement bandwidth.

Type of noise	$S_y(f)$	$\sigma_y^2(\tau)$	$mod\,\sigma_y^2(\tau)$
white PN	$h_2 f^2$	$\frac{3f_H}{4\pi^2}h_2\tau^{-2}$	$\frac{1}{2f_H}\sigma_y^2(\tau)\tau^{-1}$
flicker PN	$h_1 f^1$	$\frac{1.038+3ln(2\pi f_H\tau)}{4\pi^2}h_1\tau^{-2}$	$\frac{3.37}{3.12+3ln(\pi f_H\tau)}\sigma_y^2(\tau)$
white FN	h_0	$\frac{1}{2}h_0\tau^{-1}$	$0.5\sigma_y^2(\tau)$
flicker FN	$h_{-1}f^{-1}$	$2ln(2)h_{-1}$	$0.67\sigma_y^2(\tau)$
random walk FN	$h_{-2}f^{-2}$	$\frac{2}{3}\pi^2 h_{-2}\tau$	$0.82\sigma_y^2(\tau)$
linear drift	-	$\frac{1}{2}D_y^2\tau^2$	$\sigma_y^2(\tau)$

performance of two oscillators which instabilities are given in different characterizations. Furthermore the frequency data must be acquired in an appropriate mode of counter operation [38].

Both the AVAR and the MAVAR can also be calculated from a measured PSD as [39,40]

$$\sigma_y^2(\tau) = 2\int_0^\infty S_y(f)\frac{\sin^4(\pi f\tau)}{(\pi f\tau)^2}\,\mathrm{d}f \tag{2.29}$$

$$mod\,\sigma_y^2(\tau) = 2\int_0^\infty S_y(f)\frac{\sin^6(\pi f\tau)}{(\pi fn\tau)^2\sin^2(\pi f\tau_0)}\,\mathrm{d}f\ , \tag{2.30}$$

where $\tau = n\tau_0$. Note that the conversion from the frequency-domain to the time-domain gives a unique result, while there is an arbitrary number of PSD of frequency fluctuations which give exactly the same Allan deviation.

2.4 Determination of frequency instability

Generally, a stable reference is indispensable to determine the frequency instability of an oscillator. In principle, this can be a dispersive or absorptive system, but this necessitates that both the oscillator and the reference have the same operation frequency. Therefore, it is more convenient to employ a second oscillator and measure the beat signal frequency employing frequency counters to determine the relative instability σ_{AB} between these oscillators [41]

$$\sigma_{AB}^2 = \sigma_A^2 + \sigma_B^2 - \frac{1}{(N-1)}\sum_{k=1}^{N-1}(\overline{y}_{A_{k+1}} - \overline{y}_{A_k})(\overline{y}_{B_{k+1}} - \overline{y}_{B_k})\ . \tag{2.31}$$

The first two terms denote the variance of each single oscillator and the latter represent correlations between the two oscillators. Two qualitative remarks can be made

at this point: First, if both oscillators are truly independent, the correlation term in Eq. 2.31 averages to zero with increasing quantity of frequency data. Second, the reference oscillator B must provide a superior stability $\sigma_B \ll \sigma_A$ to determine the absolute performance of oscillator A.

Hence, the development of an oscillator that is anticipated to surpass the stability of previous oscillators often comprises the setup of a second identical system. Each oscillator is assumed to contribute half to the measured variance σ^2_{AB}, inferring an upper-limit frequency deviation dividing the measured deviation by $\sqrt{2}$.

If there is no identical system available, one can perform a so-called "three-cornered hat" (TCH) comparison [41] to estimate the frequency stability of a superior oscillator, utilizing at least two reference oscillators B and C. If the oscillators are truly independent, the correlation terms in $\sigma^2_{AB}, \sigma^2_{AC}, \sigma^2_{BC}$ average out and one will obtain three sets of measured variances

$$\begin{aligned} \sigma^2_{AB} &= \sigma^2_A + \sigma^2_B \\ \sigma^2_{AC} &= \sigma^2_A + \sigma^2_C \\ \sigma^2_{BC} &= \sigma^2_B + \sigma^2_C \ . \end{aligned} \tag{2.32}$$

From this system of equations, one can easily derive the variance of each single oscillator, for instance of oscillator A, from

$$\sigma^2_A = \frac{1}{2}(\sigma^2_{AB} + \sigma^2_{AC} - \sigma^2_{BC}) \ . \tag{2.33}$$

If there are correlations the three-cornered hat formalism can produce misleading or even negative variance estimates. For example, correlated frequency fluctuations of two systems, e.g. caused by seismic noise on the shared table, would incorrectly be interpreted as frequency deviations of a third system that exhibits different perturbations. There are approaches to estimate cross-correlations between the oscillators [42–44]. However, the system is underdetermined and therefore the mathematic treatment of correlations is rather tedious. In consequence, if correlations are present, the best way to improve the confidence into the data is to increase the number of oscillators.

Chapter 3

Ultra-low noise single-crystal reference resonator

As described in chapter 2, the achievable frequency stability $\Delta\nu/\nu$ of a cavity-stabilized laser is determined by the length instability $\Delta L/L$ of the reference resonator. While the impact of external noise sources such as temperature fluctuations or vibrations on the resonator length has been technically challenged in the past, fluctuations of the resonator length resulting from Brownian motion set a fundamental limit to the stability of the most advanced laser systems which employ resonators constructed from amorphous glass materials [12, 15, 45]. The fact that the stability of lasers has barely improved over more than one decade clearly illustrates that thermal noise hampers the development of more stable lasers massively.

This chapter describes the development of an ultra-stable reference resonator constructed from single-crystal silicon to significantly reduce the thermal noise by an order of magnitude. Sec. 3.1 discusses the topic of thermal noise in optical cavities and concepts for its reduction, motivating the development of a silicon cavity. Sec. 3.2 explains why silicon is an excellent choice for constructing an ultra-low noise reference cavity. The required steps for its realization such as simulation work for a vibration insensitive cavity support are described in Sec 3.3.

3.1 Thermal noise in optical cavities

3.1.1 Introduction of thermal noise in optical cavities

Thermal noise in optical mirrors has been subject of intense research in the field of gravitational wave detection [16, 17, 23, 46–52]. Various kinds of thermally driven noise processes such as thermo-elastic noise or thermo-refractive noise are discussed in [53]. Amongst all, Brownian noise resulting from internal friction is the most dominant thermal noise source in macroscopic mirrors employed in high-finesse optical cavities.

Using the fluctuation-dissipation theorem (FDT) [54] dissipative losses in the mirrors can be related to position fluctuations on the mirror surface, which lead

to a phase distortion of the reflected wave. Yuri Levin provided a powerful method to estimate thermal noise of a mirror with temperature T in the so-called "direct-approach" [16], where the power spectral density of displacement noise $S_x(f)$ is calculated from

$$S_x(f) = \frac{2k_BT}{\pi^2 f^2}\frac{W_{\text{diss}}}{F_0^2} \ . \tag{3.1}$$

Here, k_B is the Boltzmann constant and W_{diss} is the time-averaged dissipated power in the system when an oscillatory force with amplitude F_0 and frequency f is applied. Assuming a homogenous distribution of the internal losses W_{diss} is expressed by

$$W_{\text{diss}} = 2\pi f U_{\text{max}}\phi(f) \ , \tag{3.2}$$

where U_{max} is the energy of elastic deformation at a moment when the object is maximally contracted or extended under the action of the oscillatory force and $\phi(f) = 1/Q(f)$ denotes the mechanical loss angle, which is the inverse of the mechanical quality factor Q of the material. In a typical experiment, the differential mirror displacement is sensed by a laser beam with Gaussian intensity profile with beam radius w. For a mirror described as an infinite half-space, which is a good approximation when the laser spot size is much smaller than the mirror diameter and thickness, the thermal noise of the mirror substrate calculates to [16,17]

$$U_{\text{max}}^{(\text{sb})} = \frac{1-\sigma^2}{2\sqrt{\pi}Ew}F_0^2 \ , \tag{3.3}$$

$$S_x^{(\text{sb})}(f) = \frac{4k_BT}{\pi f}\frac{1-\sigma^2}{2\sqrt{\pi}Ew}\phi \ , \tag{3.4}$$

where E denotes Young's modulus and σ is the Poisson ratio of the mirror. An important result of Levin's work was that the location of mechanical losses within the mirror is highly important for the calculation of thermal noise. Dissipative losses close to the probe beam will contribute significantly more to the thermal noise of a mirror than losses at a distant location. Hence, a multi-layer high-reflection coating typically evaporated to the mirror substrate can be a significant source of thermal noise. Treating the mirror coating as a thin layer on the substrate surface with same elastic properties but higher losses, the main conclusion found in [48] was that the coating thermal noise "[...] scales as the ratio of the coating loss to the substrate loss and as the ratio of the coating thickness to the laser beam spot size". A calculation of the coating thermal noise that considers different elastic properties is given in [23,55]

$$\begin{aligned} S_x^{(\text{ct})}(f) = {} & \frac{2k_BT}{\pi^2 f}\frac{1-\sigma^2}{EE_\perp}\frac{d}{w^2} \\ & \times \Bigg[\left(\frac{E}{1-\sigma^2} - \frac{2\sigma_\perp^2 EE_\parallel}{E_\perp(1-\sigma^2)(1-\sigma_\parallel)}\right)\phi_\perp \\ & + \frac{E_\parallel\sigma_\perp(1-2\sigma)}{(1-\sigma_\parallel)(1-\sigma)}(\phi_\parallel - \phi_\perp) \\ & + \frac{E_\parallel E_\perp(1+\sigma)(1-2\sigma)^2}{E(1-\sigma_\parallel^2)(1-\sigma)}\phi_\parallel\Bigg] \ , \end{aligned} \tag{3.5}$$

where unsubscripted E, σ, ϕ refer to the substrate material properties and subscripted to those of the coating with a distinction between parallel ($\parallel$) and perpendicular ($\perp$) directions with respect to the mirror surface. Note that Eq. 3.5 collapses to the simplified form given in [48] for the assumption of anisotropic and equal elastic properties of coating and substrate.

The topic of thermal noise drawed attention to the laser stabilization community, when Numata et al. showed that the most-stable laser systems available at that time were actually limited by Brownian thermal noise [45]. Following Levin's direct application of the FDT, they derived a formula to calculate the thermal noise of a cylindrical spacer with length L, radius R_{sp} and central bore-radius r_{sp} (given here in a slightly corrected form [56]),

$$S_x^{(\text{sp})}(f) = \frac{4k_B T}{\pi f} \frac{L}{2\pi E (R_{\text{sp}}^2 - r_{\text{sp}}^2)} \phi \, , \tag{3.6}$$

to estimate the total thermal noise of an optical reference resonator with

$$S_x^{(\text{cav})}(f) = S_x^{(\text{sp})}(f) + 2S_x^{(\text{sb})}(f) + 2S_x^{(\text{ct})}(f) \, . \tag{3.7}$$

Using Eq. 2.1 the PSD of length fluctuations $S_x(f)$ can be converted to the PSD of fractional frequency fluctuations according to

$$S_y(f) = S_x(f)/L^2 \, . \tag{3.8}$$

In the time-domain, the 1/f-dependency of $S_y(f)$ (flicker frequency noise) leads to a constant Allan deviation which is calculated according to Tab. 2.1 from

$$\sigma_y = \sqrt{2\ln(2) S_y(f) f} = \sqrt{2\ln(2) h_{-1}} = const. \, . \tag{3.9}$$

For the reference resonator employed in [12] a thermal noise floor of $\sigma_y = 3 \times 10^{-16}$ was calculated which is in good agreement with the observed flicker floor of the stabilized laser. Furthermore, it was shown that the main contributions to the thermal noise arise from the mirror substrates of the cavity ($2S_x^{(\text{sb})}(f)/S_x^{(\text{cav})}(f) \approx 84\%$), which are made from ULE glass. Note that – although machined from the same material – the contribution of the spacer is negligible ($\approx 3\%$) due to the relatively distant location from the laser beam sensing the mirror surface.

3.1.2 Concepts for the reduction of thermal noise in optical cavities

From the equations 3.6, 3.4, 3.5, 3.8 one can infer various approaches to reduce the total thermal noise of an optical reference cavity. General parameters that have impact on the thermal noise floor σ_y are temperature T, loss angle ϕ, beam radius w, coating thickness d, elastic properties E, σ, and length L of the spacer.

However, the margins in exploiting these parameters are heavily confined for practical use in optical reference resonators. For instance, lowering the temperature

of a conventional cavity made from ultra-low expansion (ULE) glass is not an option, as the mandatory insensitivity of the cavity length to temperature variations restricts these resonators to operation at room-temperature.

Coming back to the reference cavity employed in [12], Numata et al. [45] proposed an efficient way to reduce the dominant noise contribution of the mirror substrates, replacing the lossy ULE ($\phi^{\mathrm{ULE}} = 1.7 \times 10^{-5}$ [45]) by fused silica [57, 58] ($\phi^{\mathrm{FS}} \leq 5 \times 10^{-8}$) [59,60]). The lower mechanical loss reduces the substrate's contribution to S_y to a negligible level and state-of-the-art resonators following this approach are now limited by the high-reflection coatings of the mirrors, which typically consist of alternating $\lambda/4$-layers of tantalum pentoxide (Ta_2O_5) and fused silica (SiO_2).

Consequently, reducing the coating thermal noise is a subject of intense research. It includes modifying standard Ta_2O_5/SiO_2-coatings, e.g. reduce the relative amount of the lossy Ta_2O_5 [19] in the coating or increase the Q-factor of Ta_2O_5 by co-doping with TiO_2 [18], the search for alternative high-Q coating materials (e.g. $Al_xGa_{1-x}As$ hetero structures [21], Si/SiO_2 multilayers [20]) and even coatingless, diffractive reflectors [61]. However, the improvements are either moderate or not (yet) suitable for optical cavities. Typical problems arise from degeneration of the layer structures, absorption, insufficient reflectivity and the incapability to realize curved mirrors.

As a consequence, alternative strategies must be pursued to further lower the thermal noise floor of optical reference cavities. As $S_y(f)$ scales with $1/L^2$ and $S_x^{(\mathrm{sp})}(f)$ scales with L only ($S_x^{(\mathrm{ct})}$ and $S_x^{(\mathrm{sb})}$ do not rely on the length), one obvious possibility is to simply increase the resonator length. In extension, one suggestion is to increase the effective resonator length employing multi-mirror resonators. However, the gain of an effectively longer resonator length is moderate due to the additional uncorrelated noise from the mirrors [15].

From Eq. 3.5 one finds that a larger beam radius w of the probing laser field lowers the coating thermal noise originating from the fact that the uncorrelated position fluctuations on the mirror surfaces are averaged over a larger area[1]. Thus, resonators in near-planar ($R_i \gg L$, $g_i \to 1$) or near-concentric ($R_i \to L/2$, $g_i \to -1$) mirror configurations close to the stability limit are considered as a powerful possibility to reduce the cavity noise floor. Going one step further, one can also think of exciting higher-order modes of the resonator or even employ specially shaped mirrors that allow non-Gaussian eigenmodes with flattened intensity profile, leading to a better averaging of the surface fluctuations.

However, not all approaches seem practical for high-finesse cavities or do not represent a significant improvement being worth the effort. Currently favored designs propose to combine ultra-long ULE spacers with fused silica mirrors and resonator configurations close to the stability edge. These measures could provide instability floors in the mid-10^{-17} regime. However, the increased engineering effort, e.g. for a vibration insensitive support that also has to provide a sufficient mechanical integrity for a stable coupling to the resonator mode, is quite challenging. Even further reduction of thermal noise in conventional room-temperature cavities there-

[1]Note that a larger beam radius when going to a larger laser wavelength reduces $S_x^{(\mathrm{sb})}$ only. In the coating thermal noise $S_x^{(\mathrm{ct})}$ the gain is exactly compensated due to the fact that the coating thickness increases to achieve the same reflectivity.

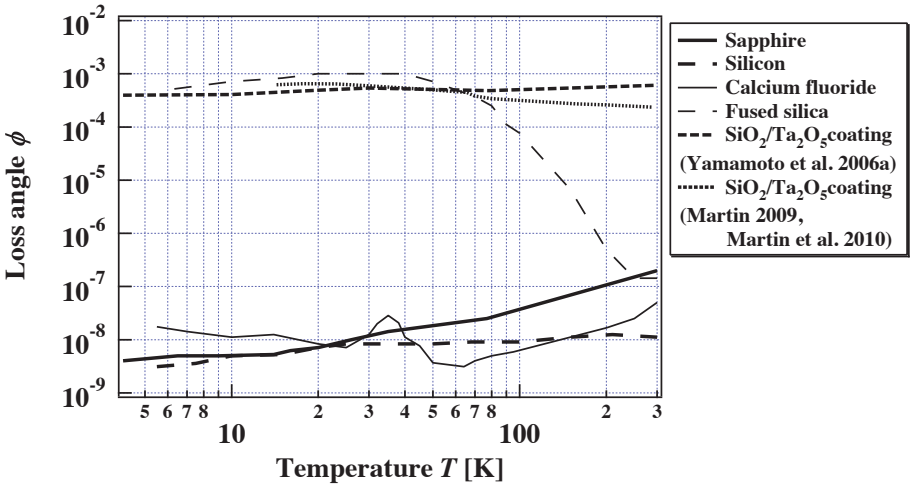

Figure 3.1: Temperature dependence of mechanical loss angle ϕ of various materials (figure taken from [62]). At cryogenic temperatures the mechanical losses of crystalline materials such as silicon [63], sapphire [64] and calcium fluoride [65] are orders of magnitude lower than that fused silica [60]. SiO_2/Ta_2O_5 coatings show an almost temperature independent loss angle [66–68].

fore seems very challenging. As $S_x(f)$ scales with T (hence, $\sigma_y \propto \sqrt{T}$), an apparent approach to reduce the coating thermal noise is to operate an optical resonator at cryogenic temperatures. Beyond the topic of thermal-expansion, resonators machined from non-crystalline glass materials are not suitable as the mechanical losses increase massively at low temperatures [60] (see Fig. 3.1). In contrast, crystalline materials such as sapphire [64], calcium fluoride [65] or silicon [63] provide almost temperature independent loss angles on the order of 10^{-8} .

In general, resonators made of crystalline materials must be cooled down to temperatures of a few Kelvin [25], where the thermal expansivity is small enough to reduce cavity length fluctuations from temperature instabilities to an acceptable level. The low temperature reduces the thermal noise floor by roughly one order of magnitude compared to conventional room-temperature resonator. However, the required cooling generates additional vibrations which have thus far prevented cryogenic cavities to exploit their full potential [25]. In this work, this limitation has been tackled, employing a reference cavity machined from single-crystal silicon. As a special property, crystalline silicon provides a vanishing thermal expansion coefficient at temperatures of 18 K and 123 K [28] (see Fig. 3.2). Operating a cavity machined from silicon at the higher zero-crossing reduces the requirements on the cryostat drastically. At a first glance, one could think that the tradeoff is not worthwhile, as the reduction of the coating thermal noise is moderate ($\sigma_y \propto \sqrt{123\,\mathrm{K}/293\,\mathrm{K}} \approx 1/\sqrt{2}$). However, as will be shown in Sec. 3.2, the superior elastic properties of silicon further reduce the coating thermal noise by a significant amount.

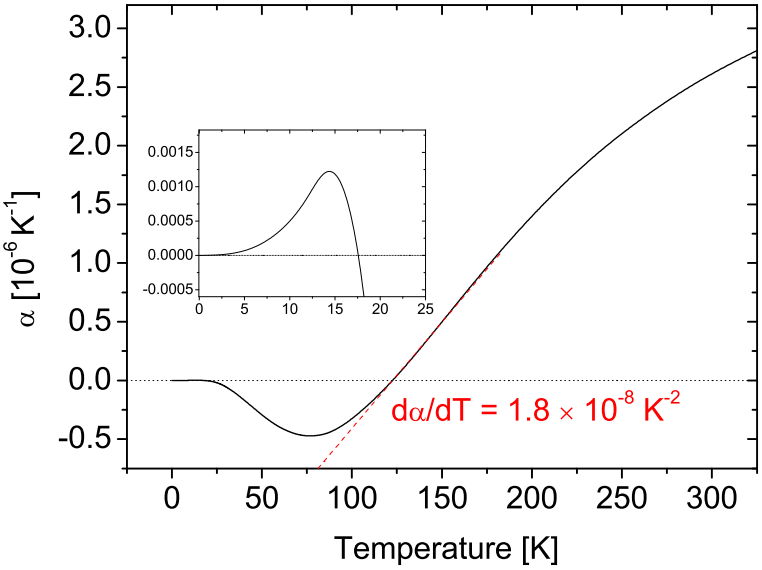

Figure 3.2: Temperature dependence of coefficient of thermal expansion of silicon (data taken from [28]). At a temperature of 18 K and 123 K the coefficient of thermal expansion approaches zero. The slopes $\alpha' = \mathrm{d}\alpha/\mathrm{d}T$ are $\alpha'(18\,\mathrm{K}) = -1 \times 10^{-8}\,\mathrm{K}^{-2}$ and $\alpha'(123\,\mathrm{K}) = 1.8 \times 10^{-8}\,\mathrm{K}^{-2}$.

3.2 Silicon as cavity material

This section will explain why silicon is a good choice for constructing an ultra-low noise reference cavity. Beyond enabling an efficient reduction of thermal noise, silicon provides various unique properties that make it a suitable material to minimize "classical sources" of cavity length fluctuations such as thermal-expansion or seismic noise.

3.2.1 Thermal noise estimates

To begin with the main motivation, the reduction of thermal noise, Fig. 3.3 shows the results of a thermal noise calculations based on the analytical expressions given in section 3.1. It compares three cavity designs with the same dimensions but different constituents: An all-ULE cavity (ULE/ULE), a state-of-the-art conventional ULE cavity with fused silica mirror substrates (ULE/FS) and a cavity machined from silicon. The parameters used are given in Tab. 3.1. For an ULE/ULE-resonator the substrates contribute dominantly to the estimated thermal noise floor of $\sigma_y = 2.5\times10^{-16}$, as mentioned before in Sec 3.1. Replacing the mirror substrates with fused silica the substrate contribution to the thermal noise becomes negligible. However, the comparably large coating contribution remains unaffected and one finds a typically observed reduction of σ_y by a factor of two. As low-noise coatings are not yet available, a further reduction can only be achieved with the quite challenging approaches described in Sec. 3.1.2. A cavity machined from silicon and operated at a temperature of 123 K, however, can lower the coating noise significantly. The estimated thermal

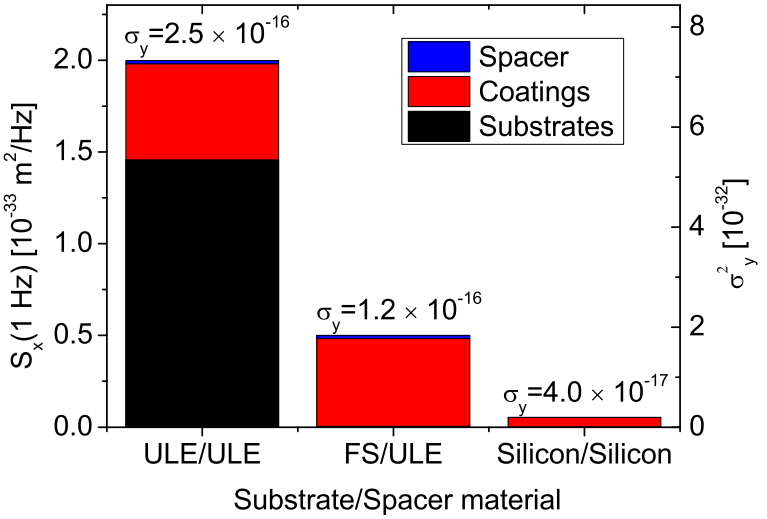

Figure 3.3: Thermal noise estimates for various material combinations of mirror substrates and spacer. Operating temperature depends on the employed spacer material (ULE: 293 K, Silicon: 123 K) and spacer length is 21 cm (see Tab. 3.1 for all parameters). The left axis shows the displacement noise power spectral density S_x, the right axis the corresponding instability expressed in the Allan variance σ_y^2. The resonator geometry is similar to that of the resonator employed in this work.

noise floor of only $\sigma_y = 4 \times 10^{-17}$, three times lower than that of a state-of-the-art room-temperature resonators with fused silica mirror substrates.

The large gain originates from the fact that, beyond the lower temperature, the coating thermal noise furthermore decreases with a larger Young's modulus of the substrate material. For silicon this value can be a factor of three higher [69]. Actually, both the lower operation temperature and the superior Young's modulus of silicon lead to the reduction of thermal noise by the same amount.

Finally – due to the low mechanical loss of silicon – the contributions of the silicon spacer and substrates can be completely neglected down to instabilities of $\sigma_y = 10^{-19}$ and $\sigma_y = 10^{-18}$, respectively. Notice from Fig. 3.3, that in case of a conventional resonator, the thermal noise contribution of an ULE spacer is on a comparable level of the coating contribution. Hence, even if new coatings with extraordinary low losses would become available, a state-of-the art room-temperature cavity would be limited to a thermal noise floor of low 10^{-17}, which is already achievable with a silicon cavity employing standard Ta_2O_5/SiO_2-coatings. To reduce the thermal noise of the ULE spacer ($S_y^{(\mathrm{sp})} \propto 1/L$, see Eqs. 3.6, 3.8), one would need to tremendously increase its length to the meter scale.

3.2.2 Thermal expansion

A change of resonator temperature around a temperature T_0 causes a change of its length due to thermal expansion that can be approximated by

Table 3.1: Parameters used for thermal noise calculations.

Property	Value			
spacer length L [mm]	212			
spacer radius R_{sp} [mm]	40			
central bore radius r_{sp} [mm]	5			
laser wavelength λ [nm]	1542			
beam radius w [μm]	448 (plane), 505 (concave, R=1 m)			
temperature T [K]	293 (ULE/FS), 123 (Silicon)			
coating thickness d [μm]	9			
	ULE	FS	Silicon	Coating
Poisson's ratio σ	0.17	0.17	0.26 [69]	0.2$\parallel$/0.2$\perp$ [50,55]
Young's modulus E [GPa]	68	72	188 [69]	90$\parallel$/100$\perp$ [50,55]
mechanical loss ϕ [10^{-8}]	1 700	5	1 [63]	42 000$\parallel$/12 000$\perp$ [55]

$$\frac{\Delta L}{L} \approx \alpha(T_0)\Delta T + \frac{1}{2}\alpha'(T_0)\Delta T^2 + \mathcal{O}(\Delta T^3) \,, \tag{3.10}$$

where ΔT is the temperature difference to the initial temperature T_0, and $\alpha(T_0)$ and $\alpha'(T_0)$ denote the coefficient of thermal expansion and its temperature derivative at T_0.

Similar to ultra-low expansion (ULE) glass at room-temperature, silicon provides a vanishing CTE $\alpha(T_0) = 0$ at a temperature $T_0 \approx 123$ K, with a linear slope of $\alpha'(123\ K) = 1.8 \times 10^{-8}$ K^{-2} [28] (see Fig. 3.2). Hence, a silicon cavity can be made insensitive to temperature fluctuations operating it close to this temperature. Consider a silicon cavity operated with some constant temperature offset ΔT from T_0, with small temperature fluctuations $\delta T \ll \Delta T$ occurring on the silicon cavity. The fractional length stability can be approximated by

$$\frac{\delta L}{L} = \alpha'(T_0)\Delta T \delta T \,. \tag{3.11}$$

Thus, for an instability at the expected thermal noise floor of $\sigma_y = 4 \times 10^{-17}$, a deviation of the mean temperature of only $\Delta T = 1$ mK would require a temperature stability of a silicon cavity at the μK-scale. However, the large thermal mass of silicon ($C_m \approx 300$ J/(kg K)) reduces the impact of environmental temperature fluctuations at short-time scales.

The sensitivity $\alpha'(123\ K)$ is about a factor of ten higher for silicon compared to ULE glass, increasing the demands on the temperature stability for a silicon cavity. In contrast to ULE resonators – which often do not stabilize the temperature exactly

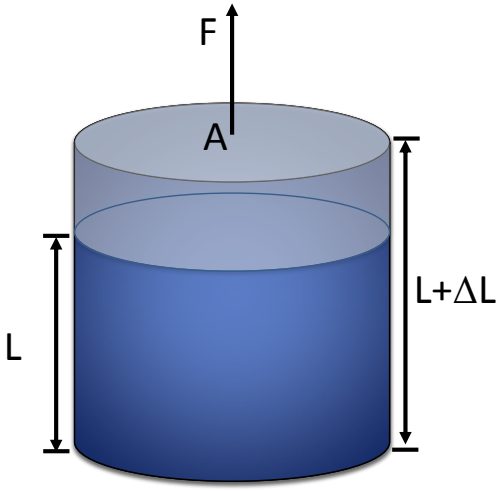

Figure 3.4: Longitudinal deformation of an elastic body when a tensile force is applied.

to the zero-crossing temperature for convenience – a cryostat is required to operate a silicon cavity close to 123 K. Thus, this disadvantage can be compensated by appropriate cryostat design.

3.2.3 Vibration sensitivity

Tensile or compressive loads that exert on an elastic body change its length according to

$$\frac{\Delta L}{L} = \frac{F}{EA} \,, \tag{3.12}$$

where F is the force applied to the cross-sectional area A and E denote the Young modulus of the material. Hence, acoustic and seismic vibrations that couple via the mount to the resonator can represent a significant source for cavity length fluctuations.

For example, in [12] an acceleration of 1 m/s^2 led to a fractional length change of $\Delta L/L \approx 2 \times 10^{-10}$ of a cylinder-shaped resonator supported from below by a v-shaped block. A very sophisticated vibration isolation was necessary to reach thermal-noise limited fractional frequency stabilities of $\sigma_y(1\,\mathrm{s}) = 3 \times 10^{-16}$ with a laser locked to this cavity.

Without going to much into detail – Sec. 3.3.1 will provide a discussion how to lower the length sensitivity to vibrations – a cavity will in general benefit from a higher Young's modulus (see Eq. 3.12). Silicon has a diamond cubic crystal structure with anisotropic elastic properties. Its Young's modulus varies between 130 GPa in the <001> direction and 188 GPa in the <111> direction [69], two to three times larger than that of amorphous glass (see Tab. 3.1). Choosing the optical axis of a silicon cavity along the <111> direction, where the stiffness is maximized, reduces the fractional length change from vibrations in the same direction by a factor of three in comparison with a cavity machined from glass.

3.2.4 Additional aspects

Among the discussed noise sources, there are further effects that can cause a variation of the cavity length. ULE spacers suffer from aging-related length drifts on the order of 10^{-16}/s [15] induced by restructuring processes in the amorphous glass material. This is not the case in single-crystal materials, allowing linear drift rates below 10^{-18}/s as demonstrated for sapphire cavities [26].

In ULE based cavities, severe sensitivities of the cavity length to the coupled-in laser power have been reported [12, 70]. The effect is explained to stem from local heating in the coatings due to laser light absorption, inducing deformations of the mirrors which effectively shorten the cavity length. In [70], the time constant of this effect was experimentally observed to be a few seconds. A fractional frequency change of $\sigma_y = 6.6 \times 10^{-16}$ for a fractional power change in transmission of 1% was determined. Consequently, the power transmission of this cavity should have been kept below $\Delta P/P = 10^{-3}$ to enable fractional frequency instabilities of $\sigma_y = 4 \times 10^{-17}$. A cavity machined from silicon could benefit from the significantly higher thermal conductivity compared to optical glasses ($\kappa \approx 500\,\mathrm{Wm^{-1}K^{-1}}$ at 123 K [71] compared to $\kappa = 1.31\,\mathrm{Wm^{-1}K^{-1}}$), avoiding large temperature gradients from the mirror substrates to the silicon spacer.

As a closing remark for this section, note that the absorption of silicon restricts laser operation to the infrared between 1 and 6 µm. However, also other spectral regions are accessible utilizing a femtosecond frequency comb as transfer oscillator [72] (see chapter 6). An operation wavelength of 1.5 µm is a reasonable choice, as the laser technology at this wavelength is rather mature and stable light can be disseminated at low cost using standard telecom fibers [73].

3.3 Realization of single-crystal silicon cavity

For a resonator with ultimate length stability various aspects and dependencies of the noise sources have to be taken into account. As mentioned in Sec. 3.2.3, enormous efforts have been put in the isolation of vibrational noise to reach thermal noise limited fractional frequency stabilities of $\sigma_y(1\,\mathrm{s}) = 3 \times 10^{-16}$ [12]. An efficient reduction of environmental vibration noise is also indispensable for a silicon cavity laser system. However, most of all, opposing cooling related vibrational noise that directly couples to the cavity is a key issue to achieve thermal noise limited length stabilities of a silicon cavity.

At first, keeping cooling related vibrations of some cooling device as low as possible is essential. Moreover, it has been shown in the past years that the impact of vibrational noise on the cavity length can be minimized with an optimized cavity design and support structure. To give an example that is intuitively accessible, one could support a cavity with vertical optical axis from below at its geometric midplane. Compression and expansion of the two halves compensate during acceleration leading to a zero-shifted mirror separation. Utilizing finite element method (FEM) it is possible to take into account the influence of the support structure, vibration sensitivities of down to $k \approx 3.5 \times 10^{-12}/(\mathrm{m\,s^{-2}})$ in the vertical direction and

$k \approx 1.4 \times 10^{-11}/(\mathrm{m\,s^{-2}})$ in the horizontal directions [57, 74, 75] have been demonstrated. This concept of symmetric mounting is not restricted to vertical cavities – comparable and even better vibration insensitivities have been achieved in horizontal mounting configurations [57, 76–78].

For the silicon cavity, intensive simulations for a vibration insensitive design have been performed. A moderate length of 21 cm was designated, which lowers the required cooling power compared to a longer cavity. This reduces cooling related vibrational noise, while still allowing an immense reduction of the thermal noise floor compared to state-of-the-art glass cavities [15] (see Sec. 3.2.1 for thermal noise estimates).

The results of the performed simulations are summarized in Sec. 3.3.1. Sec. 3.3.2 and Sec. 3.3.3 describe the resonator configuration and the manufacturing process. The results of an initial measurements for determination of the cavity linewidth are presented in Sec. 3.3.4.

3.3.1 Vibration insensitive cavity design

For the silicon cavity, simulation work on both horizontal and vertical mounting configurations was performed, taking into account the full elasticity tensor of silicon [69]. A vertical support in the mid-plane similar to the one detailed in [75] was chosen. This design sets the lowest demands on the mounting details such as the contact area. Additionally, the rotation symmetry of the geometry simplifies the machining. The <111> axis of the crystal was selected to be the optical axis of the cavity as the maximized Young modulus ($E = 187.5$ GPa [69]) in this direction minimizes tensile strain.

The support structure is a tripod made from Teflon ($E(150\,\mathrm{K}) = 5.9$ GPa, $\sigma = 0.4$ [79]) to minimize conductive heat load on the cavity (see Sec. 4.1.1). The contact diameter of the cavity ring with each Teflon rod is 5 mm, whereas the rod diameter is 12 mm most of its length and a Teflon annulus is mounted at the upper end of the rods for a higher mechanical stability (see photograph in Fig. 3.6).

To find the optimal position of the support ring, the support area by the three Teflon rods was considered to be fixed from the bottom while the cavity is subject to vertical acceleration. The result is shown in Fig. 3.5, where the fractional change of the mirror separation in dependency of the axial ring position is plotted. For a maximum vibration immunity a ring position downshifted by 2.2 mm from the symmetry plane was found. The reduced sensitivity to the axial ring position ($5.7 \times 10^{-12}/(\mathrm{mm\,m\,s^{-2}})$ compared to an ULE cavity ($1.7 \times 10^{-11}/(\mathrm{mm\,m\,s^{-2}})$ reflects the superior stiffness of the silicon crystal. This leads to less stringent demands to the machining precision, as even with a machining tolerance of 1 mm in the axial ring position the sensitivity to accelerations would be below $k_z = 10^{-11}/(\mathrm{mm\,m\,s^{-2}})$. To estimate the impact of horizontal accelerations, three cases have been studied, varying the number of inelastic elements.

Case A in Fig. 3.6a shows the deformation of the cavity when a horizontal force is applied to the inelastic support ring. Both cavity ends bend by a slightly different amount (within 10 %), due to unequal lengths of both ends to the bottom or top of

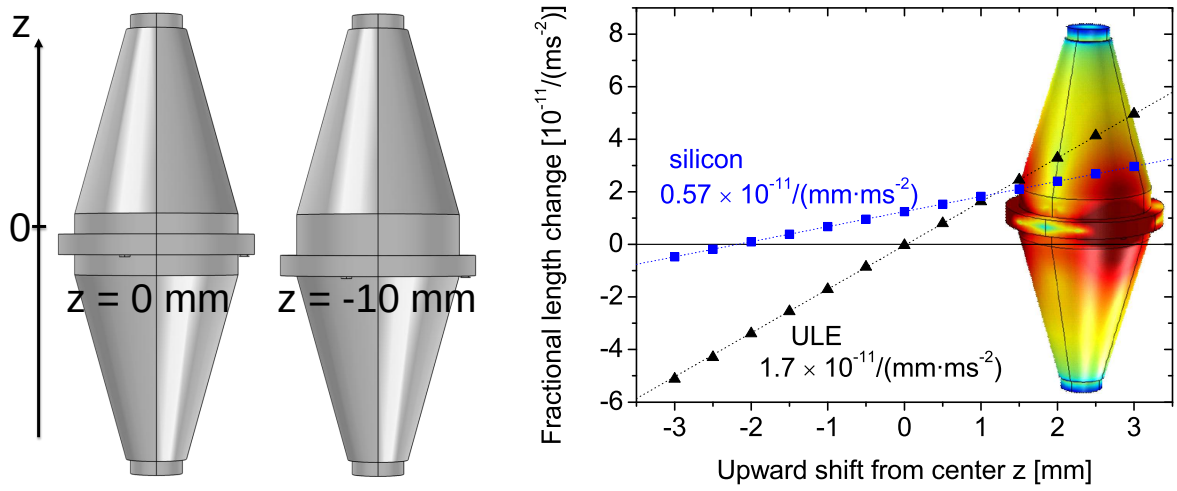

Figure 3.5: FEM calculation on the vertical cavity design, showing the fractional length change from vertical accelerations as a function of the position of the central support ring from the geometrical symmetry plane. ULE glass and single-crystal silicon as cavity materials are compared. The inset in the plot shows the strain energy distribution for the silicon cavity with $z = -2.2$ mm.

the support ring with $z = -2.2$ mm, respectively. Note that the bending does not rely on the orientation of the applied acceleration, as Young's modulus is invariant for directions in the {111} plane ($E = 169$ GPa, [69]). If the optical axis of the resonator does not perfectly match the symmetry axis of the spacer geometry, the bending will cause a length change. However, even with a transverse shift of 1 mm, this effect causes a fractional length change of only $3 \times 10^{-11}/(\mathrm{m\,s^{-2}})$. A silicon cavity again benefits from the larger Young modulus compared to ULE, reducing this value by a factor of ≈ 3. Secondly, the double-cone shape lowers inertia at the cavity ends compared to a cylindrical shape, reducing the tilt of the mirrors by a factor of two.

In case B, the cavity support ring is not fixed to the still inelastic support structure. The cavity can wobble which leads to mirror tilts with same orientations. Going one step further in case C, where the support structure is elastic and fixed at the footprints, the cavity tilt and a parallel translation of the silicon cavity of 0.2 mm/(m s^{-2}) was found. The motional effects found in case B and case C will cause a variation of the coupling efficiency, which may cause frequency fluctuations from various spurious effects. However, the impact seems to be low, as with typical horizontal accelerations provided by a vibration isolation platform of μm s^{-2} the transverse shift is six orders of magnitude below typical beam radii w on the mirrors.

Fig. 3.6b shows the lowest calculated eigenmodes of the support structure. Two modes with frequency of ≈ 40 Hz cause a translation of the cavity perpendicular to the z-axis. These modes are the most crucial for the laser performance as the coinciding tilt of cavity together with the offset from the optical axis can cause a large decrease of mode-coupling efficiency and thus induce frequency noise at this

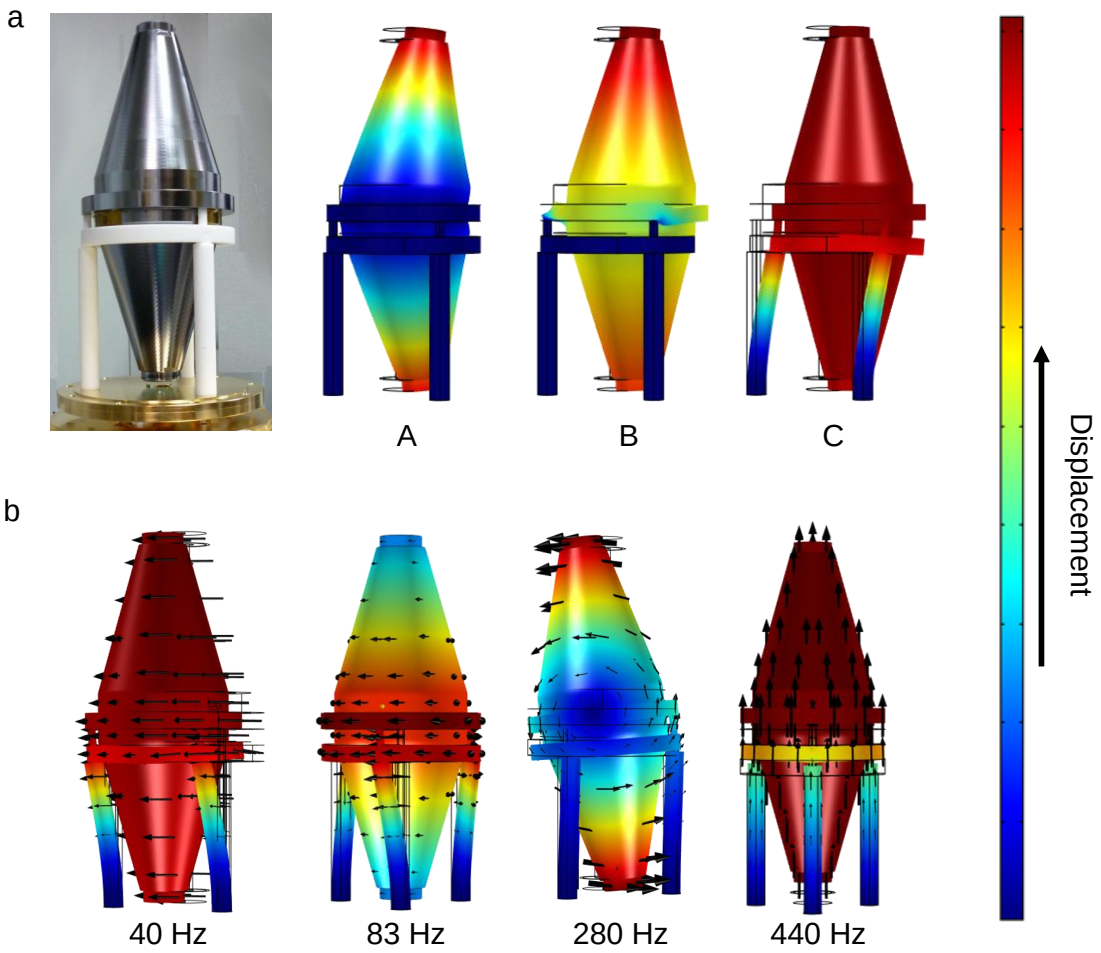

Figure 3.6: Total displacement of the silicon cavity for various considerations. **a,** Impact of horizontal accelerations on the cavity displacement with increasing number of elastic support elements. **b,** Eigenmodes of support structure and silicon cavity. An eigenmode at 40 Hz might induce severe frequency noise to a silicon cavity stabilized laser.

relatively low Fourier frequency. These modes are followed by a rotational mode at $\approx$ 80 Hz, where the support rods are twisted and the cavity rotates around the z-axis, which ideally has no impact on the mirror position. Two modes at $\approx$ 280 Hz represent a wobbling of the cavity. At $\approx$ 440 Hz the cavity translates in the z-axis compressing its support, which could induce Doppler shifts. For the mechanical properties of Teflon, available data at a temperature of 150 K was used [79], which are within 5 % of the slightly higher values of the eigenfrequencies obtained for 77 K. Further investigations have revealed that the anisotropy of the silicon crystal structure [80, 81] causes a dependency of the vibration sensitivity on rotation of the cavity along the symmetry axis. Starting with the initial parameters, where the support points intersect with the three <$2\overline{1}1$> directions at an angle of 0°, a rotation around the vertical axis leads to an increased vertical vibration sensitivity with a maximum of up to $k_z \approx 3 \times 10^{-11}/(\mathrm{m\,s^{-2}})$ at an angle of 60° (see Fig. 3.7). Between

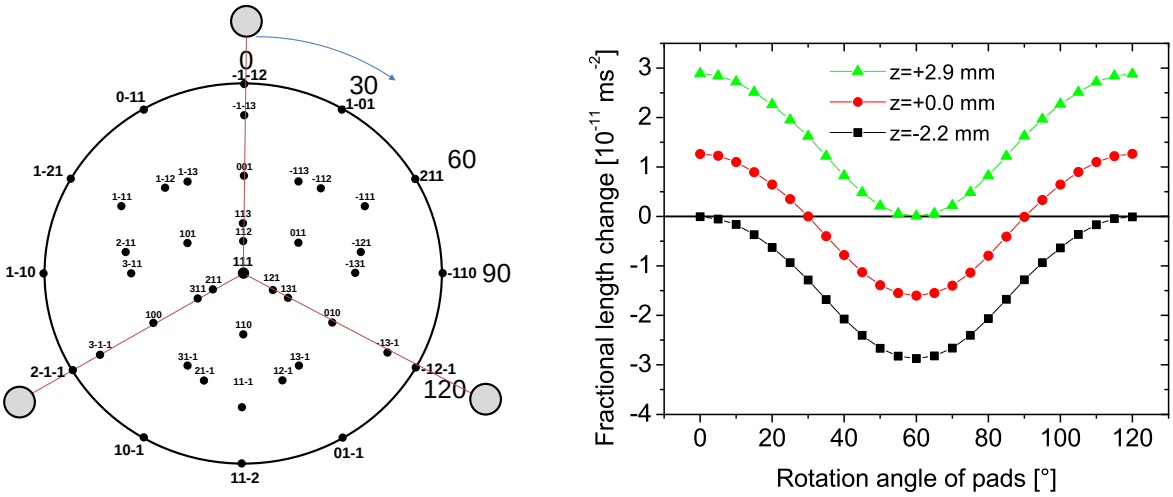

Figure 3.7: Dependency of vibration sensitivity on the position of the support points. **Left:** Crystallographic projection of (111)-oriented silicon. The outer circles represent the three support points. **Right:** FEM simulation of the vibration sensitivity to vertical accelerations of the silicon cavity design as a function of the rotation angle of the support points.

the two extreme situations the vibration sensitivity varies nearly sinusoidally. In consequence, a vanishing length change can also be achieved for other axial shifts of the ring position. For instance, an angle of 60° would require an axial shift of the ring position of $z = 2.9$ mm. In the interval $-2.2\,\text{mm} < z < 2.9\,\text{mm}$ there exist six rotational positions of the cavity where the vibration sensitivity is zero. This additional degree of freedom provides a practicable opportunity to compensate for an axial displacement of the support ring in an interval that comprises more than 5 mm and optimize the insensitivity to vertical vibrations.

3.3.2 Resonator length and mode configuration

The silicon spacer length is $L = 212\,\text{mm}$ and the detailed drawing can be found in appendix B. A plano-concave mirror configuration was chosen with highest available radius of curvature (R=1 m) to maximize the spot size on the mirror surfaces, and thus, lower the thermal noise. The beam radii w on the mirrors are 450 µm and 500 µm (see Tab. 3.1). From Eq. 2.11 one finds a longitudinal mode spacing of 708 MHz and transverse mode spacing of 108 MHz. With these parameters, the higher-order transverse modes are unlikely exited as the first higher-order mode to be within 10 MHz is found for $\Delta(m+n) = 46$, and within 1 MHz for $\Delta(m+n) = 204$.

3.3.3 Machining of the silicon cavity

The silicon spacer was machined from a low-impurity silicon rod pulled along the <111> direction with a diameter of 100 mm and with a resistivity of about 30 kΩ cm. The crystal was oriented by x-ray diffraction and precisely cut along a {111} plane to

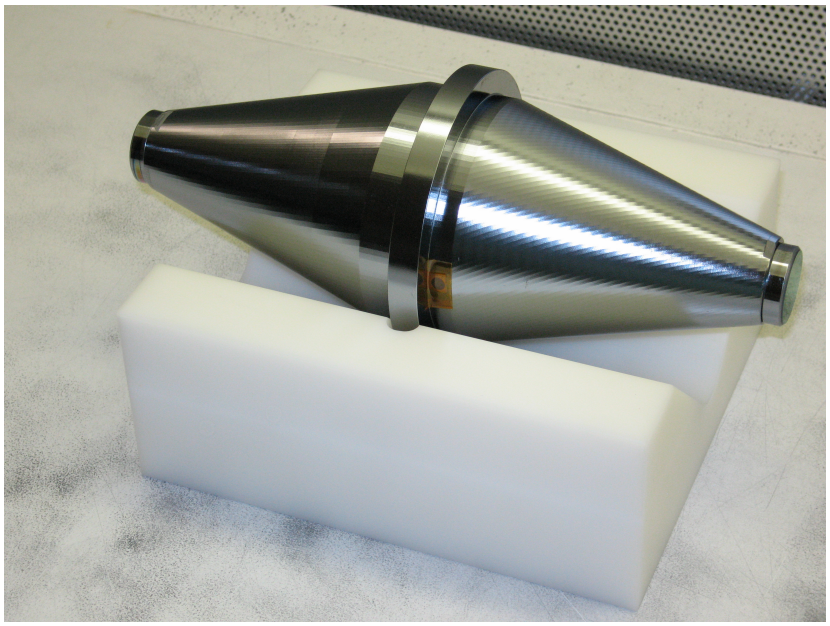

Figure 3.8: Photograph of the silicon cavity after optical contact of the mirrors.

provide a reference for the optical axis within 1 mrad[2]. After machining the crystal to the desired double-tapered cylinder shape the surface was etched to reduce stress induced by the machining[3].

Mirror substrates of 1″ diameter were machined from a similar crystal. Both the substrates and the end-faces of the spacer have been "superpolished"[4] to enable optical contacting [5]. Before optical contacting to the spacer, each substrate was coated with Ta_2O_5/SiO_2 dielectric thin films aiming an outer surface mirror reflectivity of $r^2 = 130$ parts per million (ppm) and an inner surface mirror reflectivity of $r^2 = 1 - 8$ ppm[6]. The transmission of a mirror has been specified to be 1.6 ppm which would correspond to a finesse of $\mathcal{F} \approx 2\ 000\ 000$ if no losses occur. To best maintain the single-crystal property of the entire cavity, the mirrors were contacted in the same crystallographic orientation as that of the spacer. For this purpose a $\{1\bar{1}0\}$ plane of substrates and spacer was marked by milled-in flats. The accuracy of the alignment of the optical contact is within a few degrees.

3.3.4 Cavity linewidth

After the high-reflection mirrors have been optically contacted to the silicon spacer, two approaches have been pursued to determine the linewidth $\Delta\nu_{\mathrm{FWHM}}$ of the silicon cavity. In the cavity-ring down method (see [26] for more information), one

[2]Work carried out at working group "Röntgenoptik" of the "Optics" division at PTB, Braunschweig, Germany.
[3]Work carried out at Holm Siliciumbearbeitung, Tann, Germany.
[4]1/10 wave peak-to-valley at 633 nm, 20-10 scratch dig
[5]Work carried out at Coastline Optics, Camarillo, CA, USA.
[6]All work carried out at ATFilms, Boulder, CO, USA.

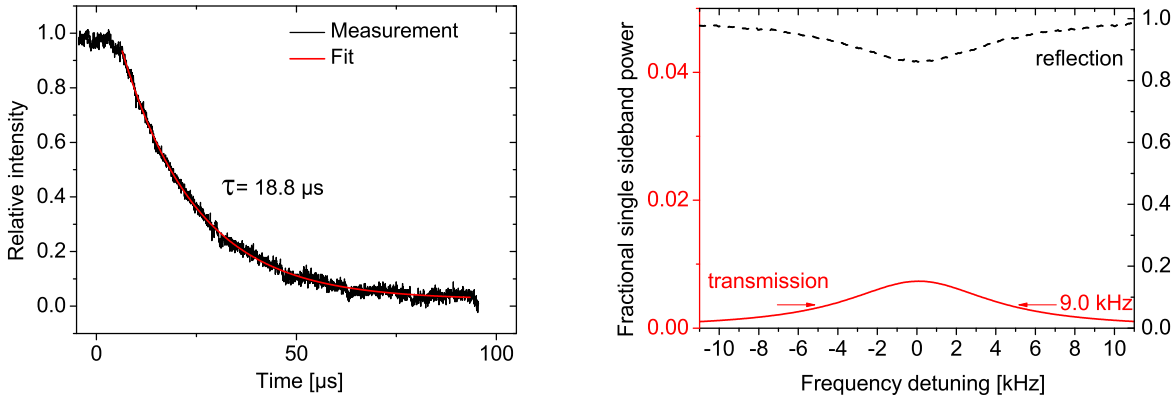

Figure 3.9: Measurements of cavity linewidth on TEM_{00}-mode. **Left:** Exponential decay of the intra-cavity power measured with a fast photo diode in transmission. **Right:** Fractional power with respect to single sideband power with respect to the detuning from the resonance frequency, measured in transmission and reflection.

measures the exponential decay of intra-cavity power after abruptly switching of the incident light. The detected decay time gives the intra-cavity photon lifetime τ_c, which is related to the cavity linewidth by the relation $\Delta\nu_{\mathrm{FWHM}} = (2\pi\tau_c)^{-1}$. The advantage of this technique is that it does not require stabilizing a laser to the cavity. A laser source with linewidth similar to the one of the cavity is sufficient to occasionally couple light into the resonator. In our experiment, source of laser light was an erbium doped fiber laser[7] emitting radiation of 194 THz ($\lambda = 1.5$ µm) with fast linewidth of $\Delta\nu \approx 3$ kHz. The silicon cavity was kept under vacuum to avoid absorption of infrared radiation from air. A fast photo diode monitored the transmitted power and, when a certain threshold was exceeded, an electronic circuit interrupted the radio frequency (RF) power driving a fiber acousto-optical modulator[8] (AOM) to switch off the incident light within 300 ns with a delay of 2 µs.

In a more advanced state of the experiment a direct measurement of the linewidth has been performed when the cavity was operational at cryogenic temperatures (see Sec. 4.1.1 for cryostat setup), utilizing a reference laser with frequency fluctuations being small compared to the cavity linewidth (reference system 1, see Sec. 5.1.1). To bridge the spectral gap between the laser frequency ν_0 and the eigenfrequency ν_{mnq} of the cavity mode a fiber-coupled phase modulator has been employed to generate first-order sidebands with optical frequencies $\nu_0 \pm \Omega_m$. Modulation depth β was chosen such that the intensity in the first-order sidebands was maximum (33.8 % of total power at $\beta = 1.84$) and the optical frequency of the sidebands was controlled with a radio frequency synthesizer[9]. The transmitted and reflected power was recorded while scanning over a cavity resonance. Fig. 3.9 shows the results of the two techniques on a fundamental TEM_{00}-mode. The decay time observed in five consecutive cavity-ringdown measurements was $\tau_c = 17.9(8)$ µs corresponding to a

[7] RP Photonics, Scorpio
[8] Gooch & Housego, FO AOM / R26040 -2- 1.54-LTD-FO-FC, +40 MHz
[9] Marconi 2024

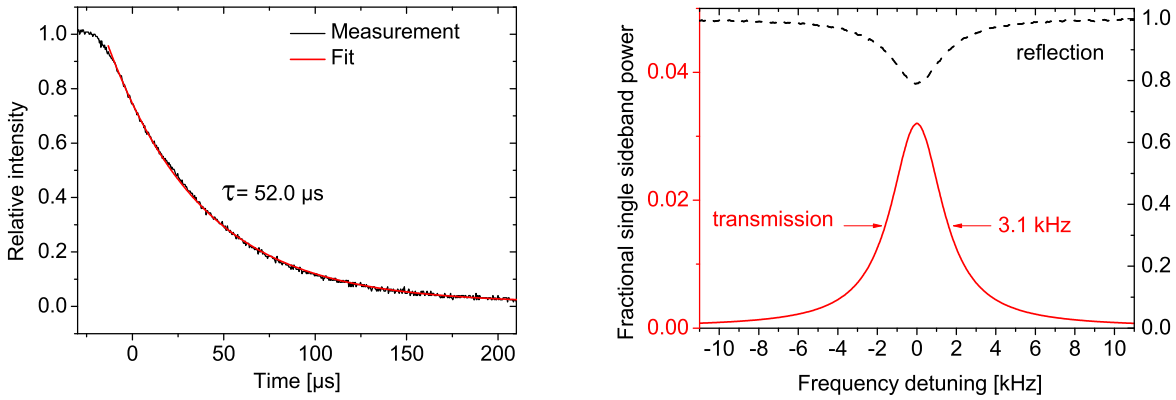

Figure 3.10: Measurements of cavity linewidth on TEM_{01}-mode. **Left:** Exponential decay of the intra-cavity power measured with a fast photo diode in transmission. **Right:** Fractional power with respect to single sideband power with respect to the detuning from the resonance frequency, measured in transmission and reflection.

cavity linewidth of $\Delta\nu_{\mathrm{FWHM}} \approx 8.9$ kHz. This result is in good agreement with the linewidth of the observed transmission peaks in the direct approach, proving that the reflectivities of the silicon cavity mirrors did not degrade when the cavity was operated at cryogenic temperatures. Although mode-matching was optimized with high effort, only about 15% of the sideband power was coupled into the resonator. The fact that only a tiny fraction (1:19) of the coupled-in power is transmitted reveals significant intra-cavity losses due to absorption or scattering.

The cavity linewidth corresponds to a finesse of $\mathcal{F} \approx 80\,000$ which is a factor of five reduced compared to the target finesse. However, a significantly higher finesse of $\mathcal{F} \approx 230\,000$ was obtained for the TEM_{01}-mode, which corresponds to a linewidth of $\Delta\nu_{\mathrm{FWHM}} \approx 3.1$ kHz (see Fig. 3.10). This indicates that the losses occur on at least one of the mirrors in a region where the intensity of the TEM_{01}-mode is minimum. It was impossible to observe the TEM_{10}-mode, which suggests that the source of loss is not located in the cross-sectional area of the nodal lines of both modes. Exciting the TEM_{01}-mode more than 21% of the incident sideband power was coupled to the resonator, which is about half of the maximum possible efficiency of about 37% (see Sec. 2.1).

A high finesse, or small linewidth, respectively, increases the slope of the PDH discriminator signal (see Eq. 2.16) and thus decreases unwanted frequency shifts caused by parasitic amplitude modulation at the PDH detection frequency (see Sec. 4.3). In consequence, in this work laser stabilization to the silicon cavity has been accomplished on the TEM_{01}-mode.

Chapter 4

Silicon cavity stabilized laser system

This chapter describes the setup of the first ultra-stable laser system comprising a cryo-cooled single-crystal silicon cavity as reference resonator.

As described in chapter 3, the silicon cavity can provide an ultra-low thermal noise floor of $\sigma_y \approx 4 \times 10^{-17}$. However, to reach this unprecedented fractional frequency stability, other sources of noise that either affect the length of the silicon cavity or compromise the locking performance of a laser must be reduced to the same level.

As explained in Sec. 3.2.2, length fluctuations originating from temperature variations can be suppressed in first-order by operating the silicon cavity at a temperature close to $T_0 = 123$ K, where the coefficient of thermal expansion of silicon is zero. However, the requirements are still high: If the cavity is operated only 10 mK beside its zero-crossing temperature, residual temperature fluctuations of the silicon cavity must be kept well below 1 µK (see Eq. 3.10).

Simulations on the cavity support (see Sec. 3.3.1) have proven that the fractional sensitivity of the silicon cavity length to seismic noise can be expected to be on a level of $10^{-11}/(\mathrm{m\ s^{-2}})$. With commercial vibration isolation platforms that provide seismic noise levels below $10^{-6}(\mathrm{m\ s^{-2}})/\mathrm{Hz}^{1/2}$, fractional frequency instabilities σ_y on the level of 10^{-17} seem feasible. However, the required cooling in cryogenic cavities leads to additional vibrational noise which has thus far prevented cryogenic cavities to compete with state-of-the-art ultra-stable lasers employing room-temperature reference cavities.

A low-vibrational cryostat is thus indispensable to reach the required stability. Commercial pulse tube coolers or cryostats that employ liquid nitrogen for the cooling have been considered. However, the cooling related vibrations do not yet suit the requirements. Thus, a gas based cryostat was developed, which has mostly overcome the limitation due to vibrations.

Besides environmental noise sources, a second critical component is the optical setup. An instability level of 10^{-17} sets higher demands to the locking performance of a laser to the reference cavity. Locking errors, in particular stemming from parasitic amplitude modulation at the Pound-Drever-Hall detection frequency, can present a serious limitation to the laser performance.

This chapter is organized as follows: The first section describes the setup of the

low-vibrational cryostat and that of the laser system. In Sec. 4.2, the expected impact of environmental noise sources to the performance of a silicon cavity stabilized laser is estimated. This includes the characterization and identification of environmental noise sources as well as measurements of the vibration sensitivity and the coefficient of thermal expansion of the silicon cavity. Sec. 4.3 addresses residual amplitude modulation, explaining the origin of this effect and presenting the results achieved with an active control loop for its suppression.

4.1 Experimental setup

This section first describes the development of a low-vibrational cryostat to operate the silicon cavity at its temperature of zero-expansion around 123 K. In the second section, the implementation of the silicon cavity as reference resonator to stabilize the output frequency of a laser is presented. Fig. 4.1 shows a photograph of the laser system.

4.1.1 Low-vibrational cryostat

A major requirement to the cryostat was that vibrations induced by the cooling mechanism should not exceed a level of 10^{-6} m s^{-2}. In preceding tests, cold nitrogen gas or liquid nitrogen was conducted through a vacuum insulated flexible tube[1] which was softly suspended from above. This tube was connected to a copper pipe which was welded to a copper cylinder placed upon a passive vibration isolation platform[2]. The vibrational noise was measured, with and without cooling, employing high-sensitivity seismometers[3]. It turned out that cooling related vibrations when employing liquid nitrogen were well above a level of 10^{-5} m s^{-2}, which was two orders of magnitude higher in comparison to the seismic noise floor of 10^{-7} m s^{-2} to 10^{-6} m s^{-2} provided by the vibration isolation platform. In contrast, employing gas induced only minor contributions to the seismic noise floor. Thus, a gas based cooling mechanism was chosen.

Fig. 4.2 shows a sketch of the cryostat developed in order to provide a cryogenic and temperature stable environment for operation of the silicon cavity at its zero-crossing of thermal expansion (see Sec. 4.2.1). The silicon cavity is located inside a vacuum chamber which is installed upon an actively controlled vibration isolation table[4] which also carries the optical components for laser stabilization (see Sec. 4.1.2). The cavity is surrounded by two massive, cylindrical, gold-plated copper-shields of which the outer one provides the cryogenic environment. Cooling of this shield is accomplished evaporating liquid nitrogen from a dewar using a resistor for heating. The gas is conducted via vacuum insulated tubes[1] and fed to the feeding lines of a spiral-shaped copper pipe which is electroplated to the bottom of the

[1] Technifab Techflex, length 2 m
[2] MinusK
[3] Geospace GS1
[4] TS-140 by JRS Scientific Instruments, 60 cm $\times$ 50 cm

Figure 4.1: Photograph of the laser system, comprising the vacuum chamber of the cryostat and the free-space optical setup, which are set on an active vibration isolation platform. A photograph of the silicon cavity contained in the vacuum chamber is superimposed for illustration. The hoses on the left are used to feed cold nitrogen gas to and back from the bottom base plate of the silicon cavity. The laser which is intended to be stabilized is located at the right hand side of the isolation platform.

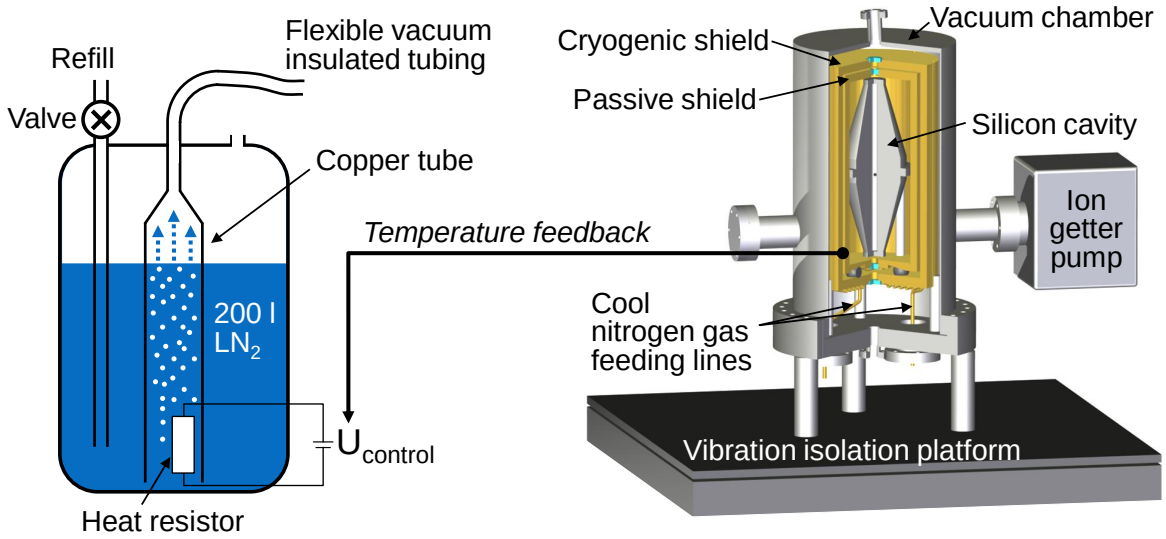

Figure 4.2: Sketch of the low-vibrational nitrogen gas based cryostat.

outer shield. The heating current of the resistor is used in a feedback loop to regulate the gas flow, thus the temperature, of the outer shield, which is monitored by a temperature sensor[5] and a high-precision thermometer[6].

To damp seismic noise from the environment and the boiling of the liquid nitrogen, the flexible gas conduction hoses are suspended from the top with mass-spring systems with eigenfrequencies of ≈ 0.5 Hz. The hoses have been modified to reduce heat load on the cold gas flow. On side of the vacuum chamber, both vacuum hoses have been cut to reduce thermal conduction from the chamber to the nitrogen gas line. On the side of the dewar the vacuum insulated end of the hose is connected to a copper tube which extends to the bottom of the dewar. This keeps the inlet at cryogenic temperatures. Furthermore the cooling gas experiences low heating rates as it is separated by the relatively warm evaporated gas building up in the upper part of the dewar. In summary, these modifications led to a twofold decrease of the required heating power of the resistor to about 40 W. This lowers the required gas flow rate, which is found for a density of 0.808 kg/l and enthalpy of vaporization of 200 kJ/kg of liquid nitrogen, to 0.9 l/h and in consequence reduces flow-related vibrations. With a specific heat capacity of nitrogen $c_p = 1$ kJ/(kg K) and a temperature difference of $\Delta T = (125 - 77)$ K between the evaporated nitrogen and the cryostat exhaust one can estimate a required cooling power of ≈ 10 W.

The heat resistor is placed inside the copper tube and the dewar is not operated in a pressurized mode which enables continuous cooling operation also during refilling of the vessel once per week. This is a mandatory feature for a long-term utilization of a silicon cavity stabilized laser such as in an optical clock setup (see chapter 6). Appropriate measures have been taken for thermal insulation of the cryogenic shield from the ambient temperature and of the silicon cavity from the

[5]Wound-wired PT-100, Class 1/10 (DIN EN 60751)
[6]Anton Paar MKT 50

cryogenic shield. The first ones primarily reduce the cooling power required to operate the cryogenic shield at 124 K. The second ones damp the impact of "fast" temperature fluctuations of the shield to the cavity.

The vacuum is maintained by an ion getter pump[7] to 5×10^{-9} mbar, which minimizes heat transfer through gas. Teflon ($\kappa = 0.26\,\mathrm{Wm^{-1}K^{-1}}$ for both cryogenic and room-temperature [82]) caps with thickness of 15 mm are pulled over the three stainless steel support rods which lower conductive heat transfer from the vacuum chamber to the cryogenic shield ($T_4 - T_3 = 170$ K) to $\dot{q}_{\mathrm{con43}} \approx 1.4$ W. The radiative heat flow from a warmer outer surface with area A_a and temperature T_a to an enclosed inner surface with area A_i and temperature T_i can be calculated according to [82]

$$\dot{q}_{\mathrm{rad}} = \sigma_{\mathrm{SB}}(T_a^4 - T_i^4)\left(\frac{1}{A_a\epsilon_a} + \frac{1}{A_i\epsilon_i} - \frac{1}{A_a}\right)^{-1}, \tag{4.1}$$

where $\sigma_{\mathrm{SB}} = 5.67 \times 10^{-8}$ W/(m^{2}K^4) is the Stefan-Boltzmann constant, and ϵ_a and ϵ_i denote the emissivities of the outer and inner surface, respectively. The cryogenic shield is surrounded by aluminum "super-insulation" foil[8] which provides an emissivity of 3%. Assuming an emissivity of 70% for stainless steel employed for the chamber, one finds a heat load of $\dot{q}_{\mathrm{rad43}} \approx 2.2$ W. In summary, $\dot{q}_{\mathrm{rad43}}$ and $\dot{q}_{\mathrm{con43}}$ contribute about one-third to the required cooling power of 10 W.

The heat transfer through the read-out cables of the temperatures sensors[9] – which have been thermally anchored to the outer shield – can be neglected in this calculation. Instead of copper ($\kappa = 410\,\mathrm{Wm^{-1}K^{-1}}$) wires, extra-thin Kapton insulated Manganin ($\kappa = 16\,\mathrm{Wm^{-1}K^{-1}}$ at 150 K) wires[10] have been employed, which reduces the heat transfer of each meter wire to the order of 10 µW at a temperature difference of 170 K. Each temperature sensor has been read out in a four-wire configuration, which makes the temperature measurements insensitive to the large electrical resistivity of the Manganin wire.

For an efficient suppression of temperature fluctuations on the cryogenic shield the silicon cavity has been thermally isolated from the outer shield by a high degree. The additional, passive copper shield prevents radiative heat transfer between the outer shield and the silicon cavity. Furthermore, its mass of 10 kg provides a large thermal capacity of about $C_2 = 3$ kJ/K at 123 K and heat flow from the outer shield is suppressed by three soda-lime glass ($\kappa \approx 0.7\,\mathrm{Wm^{-1}K^{-1}}$ [83]) support balls with diameter of $d = 20$ mm. Considering the balls as cylinders with same volume in a conservative estimate, a heat flow of $\kappa_{32} \approx 20$ mW/K between cryogenic shield and passive shield can be estimated. Radiative heat transfer between the two shields is two orders of magnitude below, thus can be neglected ($\epsilon_{\mathrm{gold}} < 0.5\%$ at 123 K [84]). The silicon cavity provides a thermal capacity of about $C_1 = 0.5$ kJ/K and is again thermally isolated from the passive shield, being supported on a tripod entirely made from Teflon. Benefiting from the vertical cavity design, the long distance be-

[7] Vacion Plus StarCell, 20 l/s
[8] SCB SCBnrc07-09
[9] Wound-wired PT-100, Class 1/10 (DIN EN 60751)
[10] AWG-36 (diameter 0.127 mm)

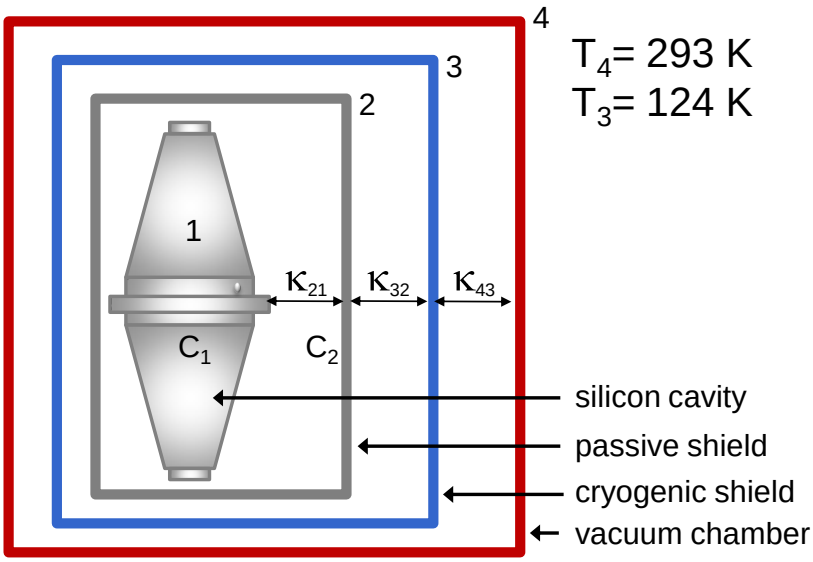

Figure 4.3: Sketch of a model for the thermal management of the cryostat.

tween the passive shield base and the silicon cavity support ring minimizes conductive heat flow to $\dot{q}_{\text{con21}} \approx 0.27$ mW/K. Assuming an emissivity of 10% for silicon, $\dot{q}_{\text{rad21}} \approx 0.2$ mW/K, thus $\kappa_{21} \approx 0.47$ mW/K.

From a model where heat flow only occurs between neighboring thermal capacities (see Fig. 4.3), one expects a suppression of thermal fluctuations from the shield to the cavity following the characteristics of a second-order low-pass filter (LPF), where the individual time constants of the first-order "passive shield LPF" and the "silicon cavity LPF" are $\tau_{23} = C_2/\kappa_{23} \approx 1.7$ days and $\tau_{23} = C_1/\kappa_{12} \approx 12.3$ days. To determine the transfer function between the cryogenic shield temperature T_3 and the silicon cavity temperature T_1 the interaction between the two "low-pass filters" needs to be taken into account.

Assuming that the cryogenic shield temperature T_3 is constant, the thermal system can be described according to

$$C_2\dot{T}_2 = \kappa_{23}(T_3 - T_2) - \kappa_{12}(T_2 - T_1) \ , \tag{4.2}$$

$$C_1\dot{T}_1 = \kappa_{12}(T_2 - T_1) \ . \tag{4.3}$$

A convenient way to solve these differential equations in the time domain is to perform a Laplace transform [85, 86], which allows an elementary algebraic treatment of these differential equations in the frequency domain. In Laplace space, Eq. 4.2 and Eq. 4.3 read

$$sC_2\tilde{T}_2 = \kappa_{23}(\tilde{T}_3 - \tilde{T}_2) - \kappa_{12}(\tilde{T}_2 - \tilde{T}_1) \ , \tag{4.4}$$

$$sC_1\tilde{T}_1 = \kappa_{12}(\tilde{T}_2 - \tilde{T}_1) \ , \tag{4.5}$$

where s is a complex argument and $\tilde{T} = T(s)$. From Eq. 4.4 and Eq. 4.5 one derives

$$\tilde{T}_1 = \tilde{T}_3 \frac{\kappa_{12}\kappa_{23}}{C_1C_2s^2 + (C_1\kappa_{12} + C_2\kappa_{12} + C_1\kappa_{23})s + \kappa_{12}\kappa_{23}} \tag{4.6}$$

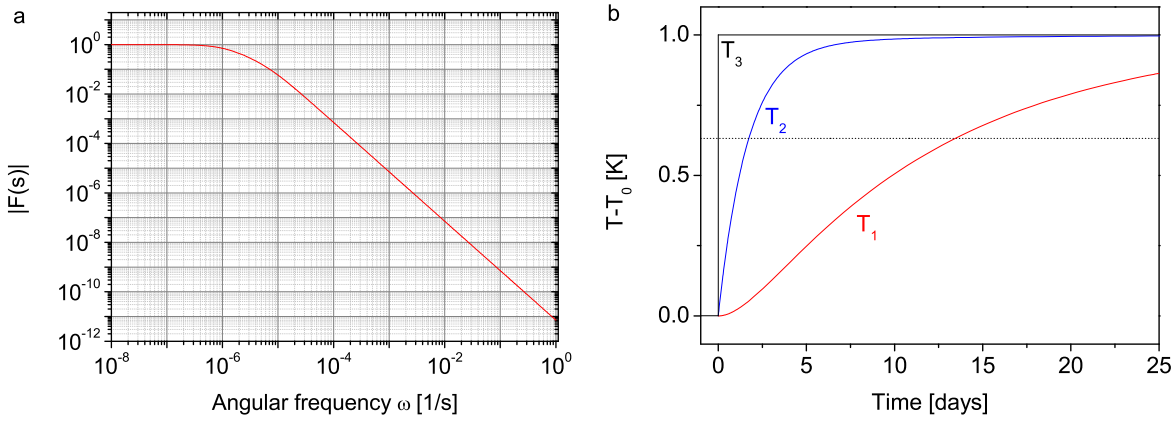

Figure 4.4: Suppression of thermal fluctuations ΔT from the cryogenic shield to the silicon cavity. **a,** Magnitude of the transfer function $F(s) = \tilde{T}_1/\tilde{T}_3$. The system can be described as a low-pass filter of second order with magnitude $|F(s)|$ which rolls of with two decades per decade for $\omega > 10^{-5}$. **b,** Step response of the thermal system. At $t = 0$, the cryogenic shield temperature is abruptly increased by one Kelvin. The response of the silicon cavity temperature T_1 is suppressed by a high degree, reaching a temperature of $1 - 1/e$ in 13.5 days.

as relation between $\tilde{T}_1$ of the silicon cavity and $\tilde{T}_3$ of the cryogenic shield. The magnitude of the transfer function $F(s \to i\omega) = \tilde{T}_1/\tilde{T}_3$ between the cryogenic shield temperature and the silicon cavity temperature is depicted in Fig. 4.4a, showing the roll-off of two decades per decade typical for a second-order low-pass. To derive the response of the system to a temperature step, Eq. 4.6 has to be multiplied with s^{-1} [86] and an inverse Laplace transform needs to be applied. Fig. 4.4b shows the calculated temperature response of the silicon cavity when a temperature step of one Kelvin is applied to the cryogenic shield. Both figures show, that temperature fluctuations on the cryogenic shield are suppressed at the silicon cavity to a high degree. For instance, temperature excursions of 1 K which oscillate with period of 100 s would induce temperature excursions on the silicon cavity of below 10 nK. In contrast, if one would have omitted the passive shield, the temperature excursions on the silicon cavity would be above 10 µK.

Black-body-radiation from the room-temperature environment (emissive power of 42 mW/cm^2 with main-peak at $\lambda \approx 10$ µm) can induce a decent heat load to the cavity, which has not taken into account in the calculations. However, both shields are equipped with windows made from BK-7 glass which reject radiation larger than $\lambda = 2.6$ µm and only 8 ppm of the black-body irradiance is transmitted. All windows have been anti-reflection-coated to avoid parasitic reflections (see Sec. 4.3). Nonetheless, a critical source of heat load can originate from absorption of laser radiation inside the silicon cavity. As it turned out (see Sec. 3.3.4) the finesse of the silicon cavity is likely degraded by intra-cavity losses or absorption. From approximately 20 µW coupled into the resonator at TEM$_{01}$-mode, about 5 µW are transmitted. Thus, neglecting losses from the multiple BK7-windows, about 15 µW of laser light are lost.

In thermal equilibrium, a complete absorption of this power would cause an upshift of the silicon cavity temperature T_1 from that of both shields of about 30 mK. However, this effect would marginally affect the time constant of the system and the absorption can be kept constant stabilizing the laser power to the transmission of the cavity.

4.1.2 Laser stabilization

As mentioned in Sec. 3.2.4, absorption restricts laser transmission through silicon to the infrared between 1 and 6 µm. However, at these wavelengths fiber lasers become available, which provide fast linewidths in the kHz-range – three orders of magnitude lower than that of diode lasers conventionally used for frequency stabilization. This lowers the demands to the servo loop, reducing the bandwidth required to lock a fiber laser to the silicon cavity.

A commercial erbium-doped fiber laser[11] at 1.5 µm was chosen for the locking of a laser's output frequency to the silicon cavity, which provides a fast linewidth of 3 kHz. The output frequency can only be tuned by acting on the length of the fiber resonator, i.e. by changing the fiber temperature or addressing a piezo attached to the fiber. The temperature servo is slow and mechanical resonances limit the servo bandwidth of the piezo to a few kilohertz. Thus, an external frequency servo, i.e. an acousto-optic modulator, has been utilized to compensate fast frequency fluctuations of the fiber laser. A schematic of the optical and electronic setup is depicted in Fig. 4.5. On its path to the output coupler (OC), the light of output power of ≈ 12 mW is sent through polarization maintaining fibers and passes several fiber-based components: An acousto-optic modulator[12] (AOM) is used as fast frequency servo for stabilization of the laser frequency. For phase modulation at $\Omega_m = 8$ MHz, the laser light passes an electro-optic modulator[13] (EOM). The polarizers prior and after the EOM are of importance for the detection and cancellation of residual amplitude modulation (RAM) from the phase modulator (see Sec. 4.3). After the second polarizer the light power has dropped to about 1 mW, of which 80% is directed to a dissemination unit which contains the optical setup to allow a phase-stable delivery of the laser light [87] to remote experiments. The performance of the fiber length stabilization was $\sigma_y(\tau) = 4 \times 10^{-17}/(\tau/s)$ determined from a frequency comparison of light at the remote end (fiber length 10 m) and reference light used for phase-locking.

The remaining light power of 20% from the polarization-maintaining splitter is coupled out to free space (focal length of OC: 8 mm) and passes a half-wave plate ($\lambda/2$) and a polarizing beam splitter (PBS), which in combination can be used to adjust the power. Afterwards, the light beam is divided by a polarization-independent beam splitter (BS) in order to detect RAM on a photo detector (PD-RAM). The other half of the light beam passes an isolator, realized by another PBS and a quarter-wave ($\lambda/4$) plate. The reflected light from the resonator which contains the information for

[11] RP Photonics Scorpio
[12] Gooch & Housego, PM Fibre-Q T-M080-0.4C2J-3-F2P, RF drive frequency 80 MHz
[13] Photline MPX-LN-0.1-P-P-FA-FA

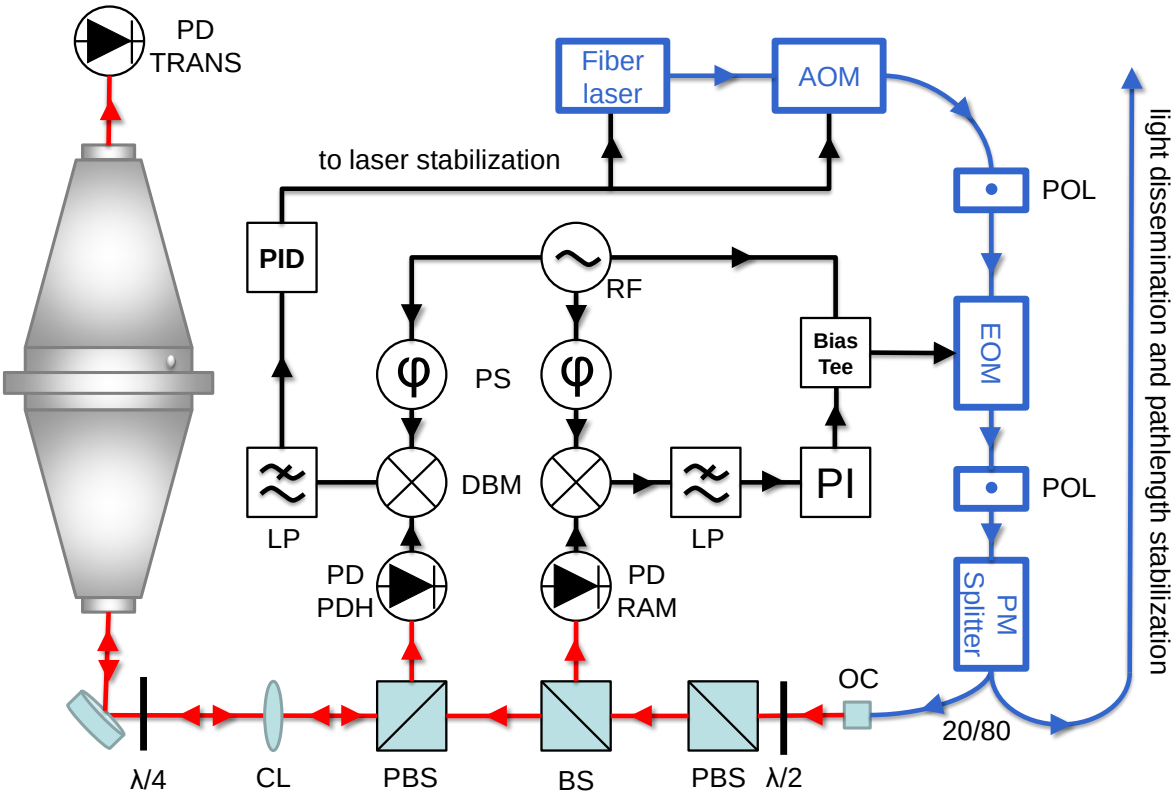

Figure 4.5: Schematic of optical and electronic setup for laser stabilization. AOM: Acousto-optic modulator, POL: Polarizer, EOM: Electro-optic modulator, PM Splitter: Polarization-maintaining splitter, OC: Output coupler, $\lambda/2$: Half-wave plate, $\lambda/4$: Quarter-wave plate, PBS: Polarizing beam splitter cube, BS: Polarization-independent beam splitter cube, CL: Resonator coupling lens, DBM: Double-balanced mixer, PS: Phase-shifter, RF: Radio-frequency source, LP: Low-pass filter, PD: Photo detector, PI/PID: Servo amplifier.

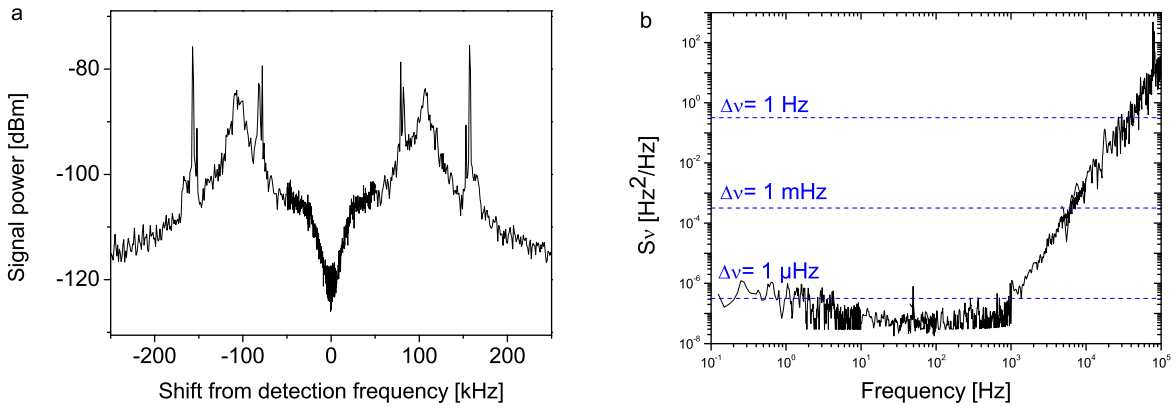

Figure 4.6: Inloop PDH error signal, recorded on a spectral analyzer at 8 MHz (**a**), and demodulated and recorded by a FFT analyzer (**b**). The frequency noise of the locked laser is suppressed to a shot-noise limited level up to a Fourier frequency of about 10 kHz. The horizontal lines in **a** indicate the corresponding linewidth $\Delta\nu = \pi S_\nu$ for different levels of white frequency noise. Large "spikes" at 80 kHz and 160 kHz observed in **a** originate from a switching power supply in the temperature control of the commercial fiber laser.

PDH-locking was detected on the photo diode PD-PDH. The transmitted light was detected on another photo diode (PD-TRANS) and was used for power stabilization controlling the power of the radio drive frequency on the AOM. This reduced fractional power fluctuations in transmission from a constant level of 10^{-3} to 10^{-5} in the investigated time intervals of 10 000 seconds each.

The radio frequency driving the EOM and the phase-shifted references is generated from a highly stable RF reference utilizing a multi-channel direct digital synthesizer (DDS). Modulation depth was chosen such that the error signal was maximized ($\beta = 1.08$). The electronic signal processing in the PDH and RAM detection is similar, demodulating the precedingly amplified RF signals with double-balanced mixers (DBM). The phase of the local frequency inputs from the DDS were maximized by changing the phase by $90°$ when the signal was zero. The mixer outputs were low-pass filtered and fed to the servo electronics.

For PDH locking, feedback was applied using both the piezo of the fiber laser and the AOM. The piezo provides a large locking range of > 100 MHz, which enables the system to stay in lock for a long time even if the free-running laser would undergo a large drift. Mechanical resonances limit the servo bandwidth of the piezo to a few kilohertz. To compensate fast frequency fluctuations of the laser the AOM is used. The design of the homemade servo amplifier can be found in Appendix C. The demodulated error signal is amplified in a proportional-integral (PI) amplifier with additional double integrator and subsequently divided into two branches, with one fast and one slow output. Both branches feature a further PI amplifier which can be switched fully integrating to increase the servo gain at low Fourier frequencies. Fig. 4.6 shows two representations of the PDH inloop error signal, indicating the effectiveness of the servo lock. Fig. 4.6a depicts the RF error signal

recorded on a spectral analyzer at 8 MHz, originating from the beat of the sidebands with the carrier. Fig. 4.6b shows the demodulated error signal recorded with a FFT-analyzer, where the slope $\mathcal{D}$ of the error signal (including a multiplication with a first order low-pass filter function with cut-off frequency at the cavity half-width of $\Delta\nu_{\mathrm{FWHM}}/2 = 1.55$ kHz, see Sec. 2.2) has been used to calculate the corresponding PSD of frequency fluctuations S_ν. Below 10 kHz, the servo gain is sufficient to suppress frequency noise of the free-running laser relative to the cavity to a shot-noise limited detection floor which is on a level of $S_\nu^{(\mathrm{shot})} = 10^{-7}$ Hz^2/Hz, far below the instability regimes that are aimed at.

The discrepancy between the observed and the calculated shot-noise limit ($S_\nu^{(\mathrm{shot})} = 2 \times 10^{-9}$ Hz^2/Hz, see Sec. 2.2) is associated with the observed intra-cavity losses (see Sec. 3.3.4), which are not considered in Eq. 2.18.

4.2 Characterization of environmental noise sources

In this section, the impact from environmental noise sources on the length stability of the silicon cavity is estimated. The measurements include the evaluation of the silicon cavity to external noise sources as well as the determination of the power of noise.

4.2.1 Thermo-expansive perturbations

Thermal expansion of the silicon cavity

As described in Sec. 3.2.2, single-crystal silicon provides zero-crossings in its CTE, which are at temperatures $T_0 \approx 18$ K and $T_0 \approx 123$ K [28]. The reported values based on measurements with capacitive dilatometry contradict with another CTE measurement, which employed a Fabry-Pérot cavity with a silicon spacer [27]. The reported value for the upper zero-crossing temperature was 148 K, distinctly higher than the results obtained with capacitive dilatometers. The authors state that the discrepancies are caused by sample preparation, cementing fused silica mirrors to the silicon spacer with aluminum collars.

As in this work, the silicon cavity employs silicon mirrors and care has been taken to realize the optical contact in such a way that the crystalline properties are maintained for the whole cavity (see Sec. 3.3.3), one would expect the minimum length of the silicon cavity close to the reported zero-crossing temperatures in [28].

To determine the zero-crossing of the silicon cavity, a measurement of its fractional length change has been performed sweeping the operating temperature of the cryostat across the expected temperature of $T_0 = 123$ K. The length change ΔL of the cavity has been probed in a beat measurement between the silicon cavity stabilized laser and a second cavity stabilized laser operated at 1.5 µm (reference system 1 in Sec. 5.1.1). A PT-100 sensor[14] was mounted to the support ring of the silicon cavity to monitor its temperature. To reduce systematic uncertainties in the temperature

[14]Class 1/10 (DIN EN 60751)

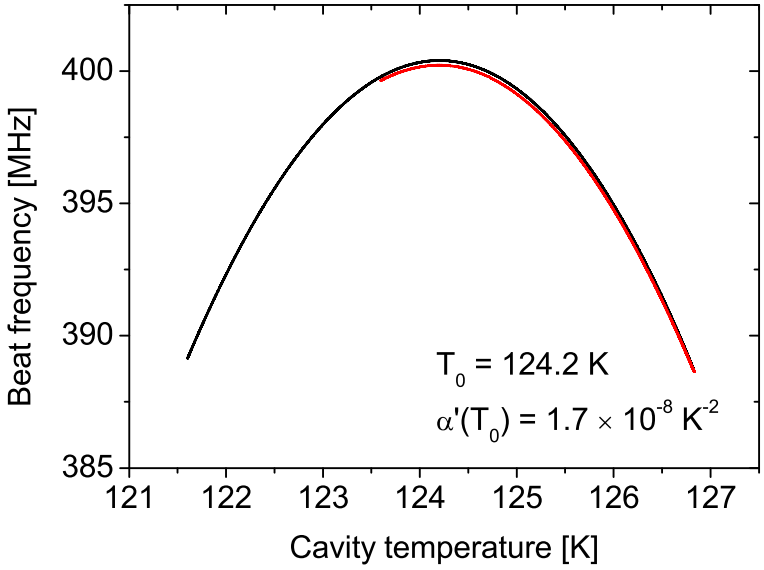

Figure 4.7: Beat note of the silicon cavity stabilized laser with a reference laser as a function of cavity temperature. The minimal length of the silicon cavity is found for a temperature of 124.2(1) K. Measurement time was five days. Chronological order starting with increasing the temperature: black curve, red curve.

reading due to an inhomogeneous temperature distribution in the silicon cavity, the temperature has been swept slowly and in both directions: The duration of the measurement was 5 days, and the silicon cavity temperature exhibited a linear drift of $\approx \pm 30$ µK/s at 124.2 K. The result of the two consecutive temperature sweeps is depicted in Fig. 4.7. The point of minimal expansion was found at 124.2(1) K with uncertainty dominated by the temperature sensor. The slope of the coefficient of thermal expansion is $\alpha'(124.2\,\mathrm{K}) = 1.71(2) \times 10^{-8}\ \mathrm{K}^{-2}$. The obtained results are in a good agreement with the recommended values for the thermal expansion of silicon given in [28] and confirm that the discrepancy found in [27] likely resulted from sample preparation of the Fabry-Pérot cavity.

Temperature stability of the silicon cavity

To estimate the temperature instability σ_{T_1} of the silicon cavity and its impact on the fractional instability $\sigma_y = \alpha(T)\sigma_{T_1}$ of the cavity length, at first the temperature instability σ_{T_3} of the actively cooled shield has been derived. Fig. 4.8a shows the distribution of temperature readings from the inloop sensor of the temperature stabilization, which is attached to the base plate of the shield. The data set contains temperature readings of one refill cycle of the dewar corresponding to a measurement time of 1 week. Around the set point, the temperature deviations follow a normal distribution, with a standard deviation of 0.2 mK. Calculating the Allan deviation σ_{T_3} from this data set reveals that the temperature stability decreases for longer time scales with maximum excursions around 100 s. This behavior originates from delay in the temperature detection (damping from the copper in between the sensor and the ni-

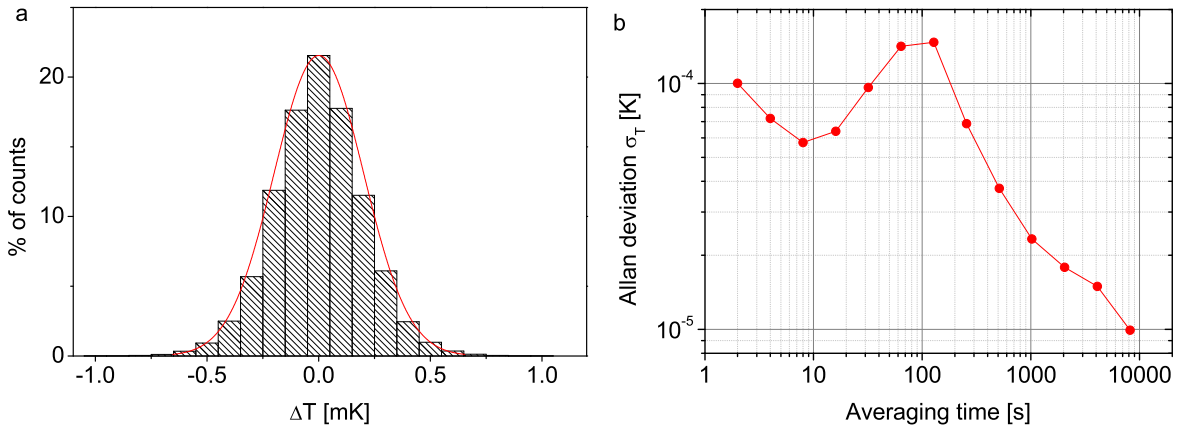

Figure 4.8: Performance of the temperature stabilization of the cryogenic shield. **a,** Histogram of temperature offsets from the set temperature during one refill cycle (1 week). It shows a mostly Gaussian distribution with standard deviation of 0.2 mK. Each bar represents the digital resolution of the thermometer of 0.1 mK. **b,** Allan deviation of the temperature fluctuations. At time scales after 10 s the temperature instability increases with a maximum at 100 s due to the limited response of the actuator and delay in the temperature detection.

trogen gas) and the limited response time of the actuator. These excursions average out on the way to the top of the outer shield. However, as the thermal transfer is assumed to be dominated by thermal conduction through the support structures (see Sec. 4.1.1), the performance of the inloop sensor will be used to determine the impact of the observed temperature instability on the silicon cavity temperature.

The transfer function $F(s) = \tilde{T}_1/\tilde{T}_3$ has been experimentally evaluated performing a temperature step of 0.1 K after the system has reached a state close to thermal equilibrium. In this measurement no temperature sensor was attached to the cavity and the temperature has been calculated from a virtual beat frequency with a hydrogen maser (see Sec. 6.2). Knowing the beat frequency where the silicon cavity has its zero-crossing of thermal expansion, the cavity temperature can be calculated according to Eq. 3.10. The initial linear frequency of the silicon cavity laser was about 0.650 mHz/s (hydrogen maser $\approx$ 2 µHz/s), which corresponds to a temperature drift of about 2 nK/s at an initial temperature offset 0.1 K below $T_0 = 124.2$ K. The temperature on the cooling shield was increased by ΔT=0.1 K and the beat signal has been recorded with a frequency counter[15]. The result, given here as temperature offset from the initial temperature $T_1 \approx 124.1$ K, is depicted in Fig. 4.9a. The observed temperature response of the silicon cavity is in good agreement with the calculation in Sec. 4.1.1 indicated by the blue curve. Applying the derived transfer function shown in Fig. 4.4, Fig. 4.9b demonstrates the efficient suppression of temperature fluctuations of the outer shield fluctuations σ_{T_3} to the silicon cavity.

In Fig. 4.10, the resulting fractional length instability of the silicon cavity is plotted for various temperature offsets $|T_1 - T_0|$ from the zero-crossing temperature of

[15]K+K Messtechnik: model FXE

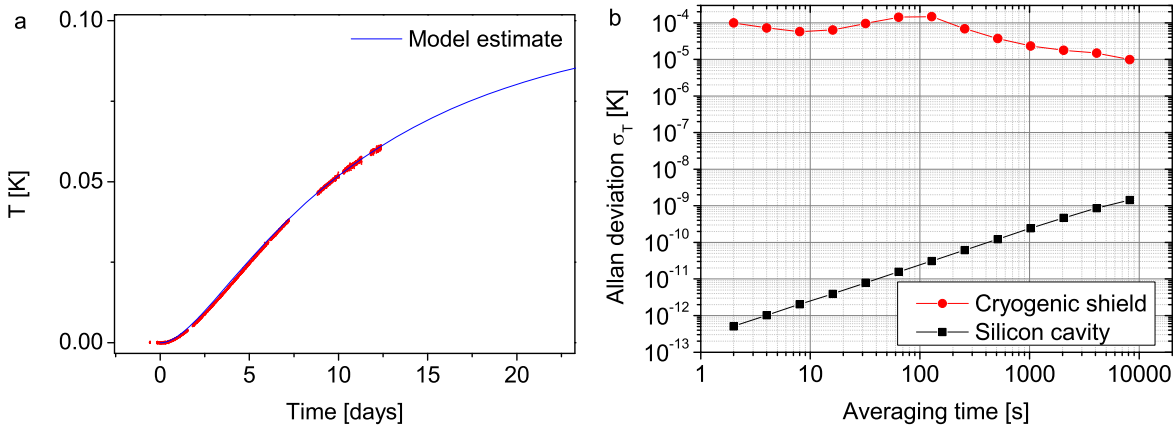

Figure 4.9: **a,** Response of silicon cavity temperature to an increase of the outer shield temperature applied within four minutes. The observed response is in good agreement with the model derived in Sec. 4.1.1. **b,** Damping of temperature fluctuations from the cryogenic shield to the silicon cavity applying the transfer function $F(s) = \tilde{T}_1/\tilde{T}_3$ depicted in Fig. 4.4a. The temperature instability of the silicon cavity is below $\sigma_{T_1} = 1$ nK up to one hour.

the silicon cavity, assuming a constant CTE around the offset temperature. Even if the silicon cavity temperature is offset one Kelvin from T_0, fractional length instabilities σ_y due to thermo-expansive instabilities do not exceed the estimated thermal noise floor of $\sigma_y = 4 \times 10^{-17}$ up to 100 s averaging time.

4.2.2 Seismic noise

Measurement of the vibration sensitivity

The sensitivity of the silicon cavity length to accelerations was analyzed from a beat signal between the silicon cavity stabilized laser and another cavity stabilized laser (reference system 1 in Sec. 5.1.1) when accelerations were actively applied to the silicon system. In three consecutive measurements $l = 1, 2, 3$, the silicon system has been accelerated in each direction, x,y,z, applying a sinusoidal drive signal at a frequency of 6 Hz to the active vibration isolation table. The accelerations were monitored with three piezoelectric accelerometers[16] mounted on the isolation platform and the resulting frequency modulation was recorded with a frequency counter[17] with a gate time of $t_G = 10$ ms. For a correct phase value, a delay of $t_D = 18.1$ ms (39° at 6 Hz) of the analog output of the frequency counter was taken into account[18]. Fig. 4.11 shows the observed frequency modulation of the silicon-cavity-locked laser when a vertical acceleration of $a_z = 0.07$ m s^{-2} is applied. When horizontal directions were excited, the inertia of the setup upon the vibration isolation table caused a wobbling of the platform, which led to a significant coupling to the vertical direc-

[16] PCB Piezotronics Model 393B31
[17] Fluke PM6681
[18] $t_D = 1.05 t_G + 0.00763$, relation derived by measurement.

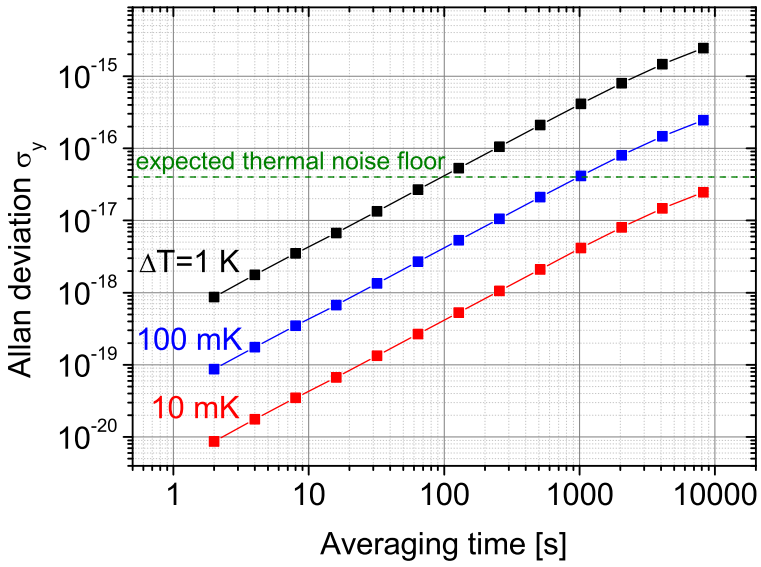

Figure 4.10: Fractional length instability σ_y of the silicon cavity for various temperature offsets $|T_1 - T_0|$ from the zero-crossing temperature, assuming the CTE is constant around the offset temperature (see Sec. 3.2.2).

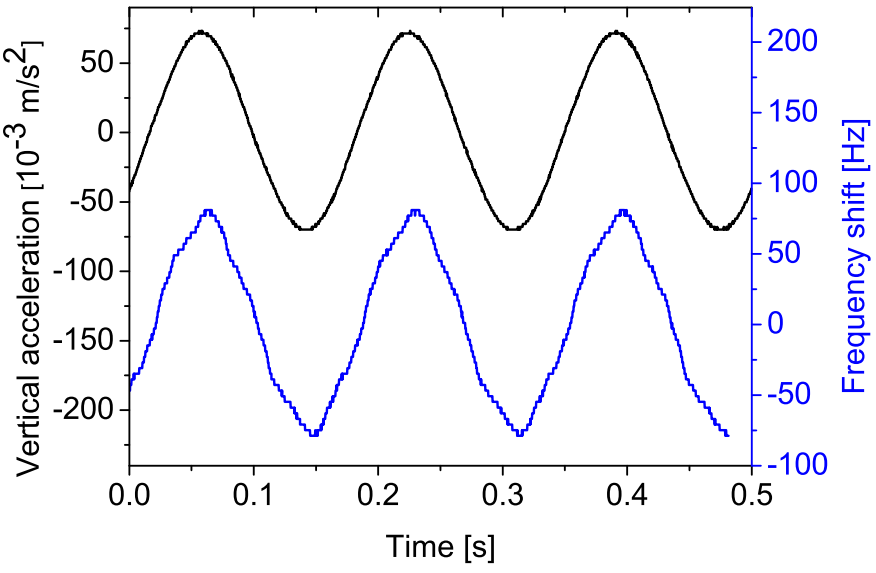

Figure 4.11: Frequency response of the silicon cavity stabilized laser induced by a deliberate vertical acceleration. An acceleration of $a_z = 0.07$ m s^{-2} led to a frequency excursion of 74 Hz, which corresponds to a (fractional) vibration sensitivity of 1 kHz/(m s^{-2}) (5.4×10^{-12}/(m s^{-2})).

Table 4.1: Amplitude of the observed laser frequency modulation f_l in three measurements $l = 1, 2, 3$ due to active excitation of vibrations of Fourier frequency 6 Hz.

Meas. l	a_{lz} [m s^{-2}]	a_{ly} [m s^{-2}]	a_{lx} [m s^{-2}]	φ_{lz} [°]	φ_{ly} [°]	φ_{lx} [°]	f_l [Hz]
1	0.070	0.002	0.002	-7.1	-29.4	156.0	74.0
2	0.018	0.010	0.001	-25.6	-7.3	15.9	9.7
3	0.020	0.001	0.013	11.6	56.2	25.2	41.1

tion. Consequently, amplitude and phase relations of all acceleration components a_{lm} (see Tab. 4.1) had to be taken into account for the analysis following the approach described in [76]

$$f_l = \nu_0 \sum_{m=z,y,x} a_{lm} e^{i\varphi_{lm}} k_m \ . \tag{4.7}$$

For the vertical direction a fractional vibration sensitivity of $k_z = 5.6(3)\times10^{-12}/(\mathrm{m\,s^{-2}})$ was found. The obtained values in the horizontal directions, $k_x = 8.6(4)\times10^{-12}/(\mathrm{m\,s^{-2}})$ and $k_y = 6.9(3) \times 10^{-12}/(\mathrm{m\,s^{-2}})$, are slightly higher.

According to the simulation results in Sec. 3.3.1, the vertical sensitivity corresponds to a vertical shift of the ring position of 1 mm. However, the dependency of the vertical vibration sensitivity of the silicon cavity on rotation about its symmetry axis was not yet known when mounting the silicon cavity. The angle between the mirror flats, which indicates one of six $\{1\bar{1}0\}$ planes (see Sec. 3.3.3), and the closest support point was arbitrarily chosen to $\approx 10°$ in the experiment. In contrast – as shown in Fig. 3.7 of Sec. 3.3.1 – the rotation effect on the vibration sensitivity has three rotational symmetries only. In consequence, the rotation angle is not definite and may correspond to values of $20°$ or $40°$ ($100°$ or $80°$, respectively within $120°$). Assuming $20°$, the observed vibration sensitivity k_z agrees well with the calculated value of $k_z = 6.3 \times 10^{-12}/(\mathrm{m\,s^{-2}})$ (see Fig. 3.7). Since the obtained values were still reasonably small, the position of the cavity was kept unchanged for the experiment.

The obtained sensitivities for the horizontal directions, k_x, k_y, are on the same order as the vertical vibration sensitivity. The slight discrepancy of k_x and k_y may result from small, different offsets of the cavity mirrors to the center of the spacer end-facets. It is furthermore imaginable, that the horizontal forces at the support points are unequal and depend on the direction of the acceleration with respect to the tripod mount.

Measurement of seismic noise

To estimate the impact of vibrational noise on the laser performance of the silicon cavity locked laser, the seismic noise on the vibration isolation platform has been in-

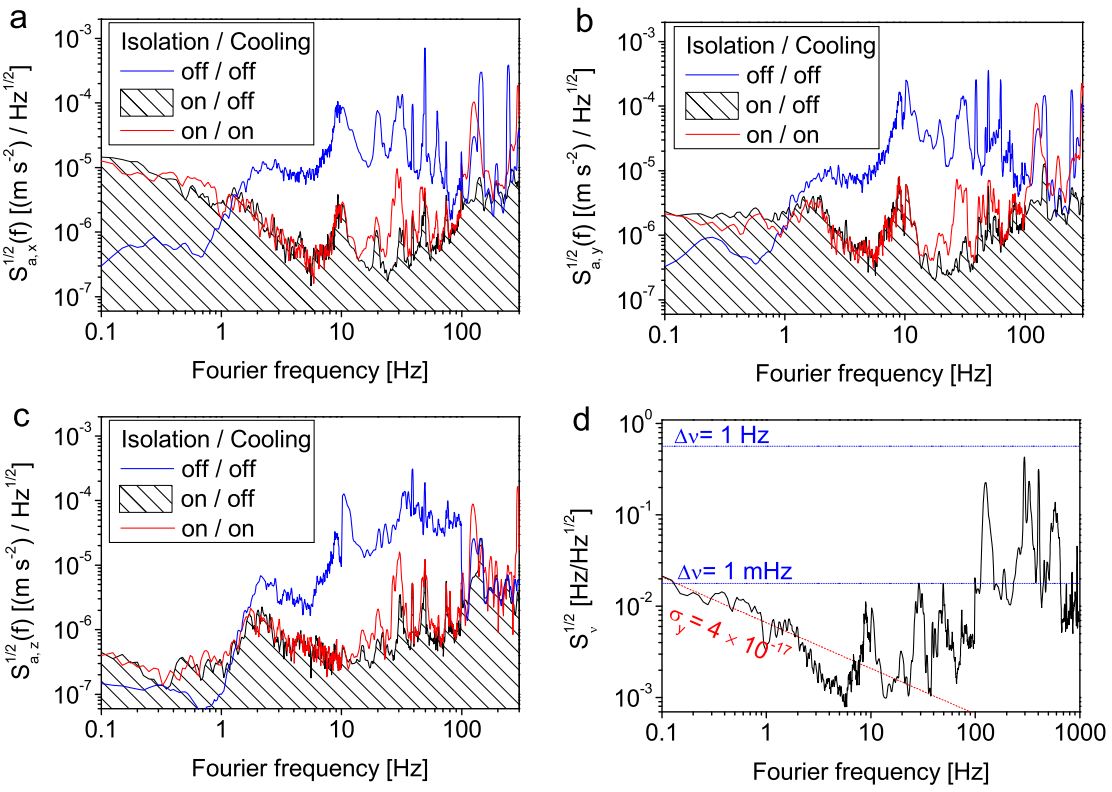

Figure 4.12: Seismic noise measurements for the two horizontal directions (**a,b**) and the vertical direction (**c**) on the vibration isolation platform. **d,** Calculated PSD of frequency fluctuations $\sqrt{S_\nu(f)}$ derived from the seismic noise spectra and the corresponding vibration sensitivity when cooling is accomplished.

vestigated in all three directions, employing high-sensitivity seismometers[19]. Each measurement was performed with deactivated and activated cooling operation to reveal the effect of the cooling mechanism on the seismic noise. Fig. 4.12a-c show the obtained data from the measurements. First, when the cooling is inactive, the measurements show that the vibration isolation suppresses vibrations from its support table in any direction between one and two orders of magnitude in a frequency interval of 1 Hz – 100 Hz. This leads to a PSD of acceleration noise $\sqrt{S_a(f)}$ in the low 10^{-6} (m s^{-2})/$\sqrt{\text{Hz}}$.

Salient higher accelerations on the lab table around 10 Hz are effectively suppressed in the vertical direction. However, in the horizontal directions the isolation is less effective. Most likely, accelerations around this frequency are conducted from the environment along the gas flow lines, which are damped in the vertical direction only (see Sec. 4.1.1). Setting the cooling operation active had no impact on the vibrational level up to $\approx$ 20 Hz. Between 20 Hz and 100 Hz the seismic level partially increases but moderately, still on a level of 10^{-5} (m s^{-2})/$\sqrt{\text{Hz}}$. Above Fourier frequencies of 100 Hz the vibration isolation platform is out of servo bandwidth and

[19]Geospace GS1

whistling from the flowing cool nitrogen gas in the lines causes large increases of acceleration at a few distinct frequencies. However, phase modulation sidebands from this "acoustical" noise do not contain considerable power thus are not expected to deteriorate laser performance significantly.

To estimate the impact of vibrations on the laser performance, the vibration spectra and the observed vibration sensitivities (see Sec. 4.2.2) have been used to calculate the expected PSD of frequency fluctuations S_ν according to

$$S_\nu(f) = \left(S_{a,x}k_x^2 + S_{a,y}k_y^2 + S_{a,z}k_z^2\right)\nu_0^2 \,. \tag{4.8}$$

The result is depicted in the lower right of Fig. 4.12d. The plot shows that vibration induced frequency noise would not prevent a thermal noise limited laser performance for Fourier frequencies up to 10 Hz.

4.2.3 Vacuum pressure

Besides the geometrical spacing of the cavity mirrors the refractive index n of residual gas between the mirrors determines the optical length of the resonator. For light of $\lambda = 1.5$ µm the refractive index of air depends on the pressure p according to [88]

$$n - 1 \approx \left(2.7 \times 10^{-7}/\text{mbar}\right)\, p \,. \tag{4.9}$$

The requirements to the quality of the vacuum stability are very stringent: A change in the vacuum pressure of only $\Delta p = 2 \times 10^{-10}$ mbar would cause a fractional length change of $\Delta L/L \approx 5 \times 10^{-17}$, which is on the order of the expected thermal noise floor of the silicon cavity.

The vacuum pressure in the apparatus was about 5×10^{-9} mbar, measured with a wide range vacuum gauge[20], and thus the vacuum pressure has to be maintained on the 10% level. However, monitoring the vacuum pressure indicated serious vacuum problems. Fig. 4.13a shows a time record of the getter pump current. Various abrupt increases of the getter current, from now on denoted as "spikes", are found. They occur with high constancy of period and amplitude, the bigger ones less frequent than the smaller one. These increases of current correspond to abrupt increases of vacuum pressure, as confirmed by the vacuum gauge. As an example, Fig. 4.13b shows the vacuum pressure as a function of time when one of the largest spikes is occurring. The pressure increases rapidly to 7.6×10^{-7} mbar, in good agreement with the pressure estimate from the getter current read out[21]. According to Eq. 4.9, this causes a (fractional) frequency shift of the laser locked to the silicon cavity of $\Delta\nu \approx 40$ Hz ($\Delta\nu/\nu \approx 2 \times 10^{-13}$). Besides these large spikes, which occur every 4 – 5 hours, the smaller spikes are classified with respect to the corresponding frequency excursion $\Delta\nu$ as follows: $\Delta\nu \approx 3$ Hz occurring every second hour, $\Delta\nu \approx 1$ Hz occurring twice per hour, and $\Delta\nu \approx 0.3$ Hz sporadic and most often.

[20] Vacom Atmion

[21] According to the manufacturer, vacuum pressure can be calculated from getter current by $(p/\text{mbar}) = (I/\text{A})^{0.8}/2500$ in the interval 10^{-9} – 10^{-6} mbar.

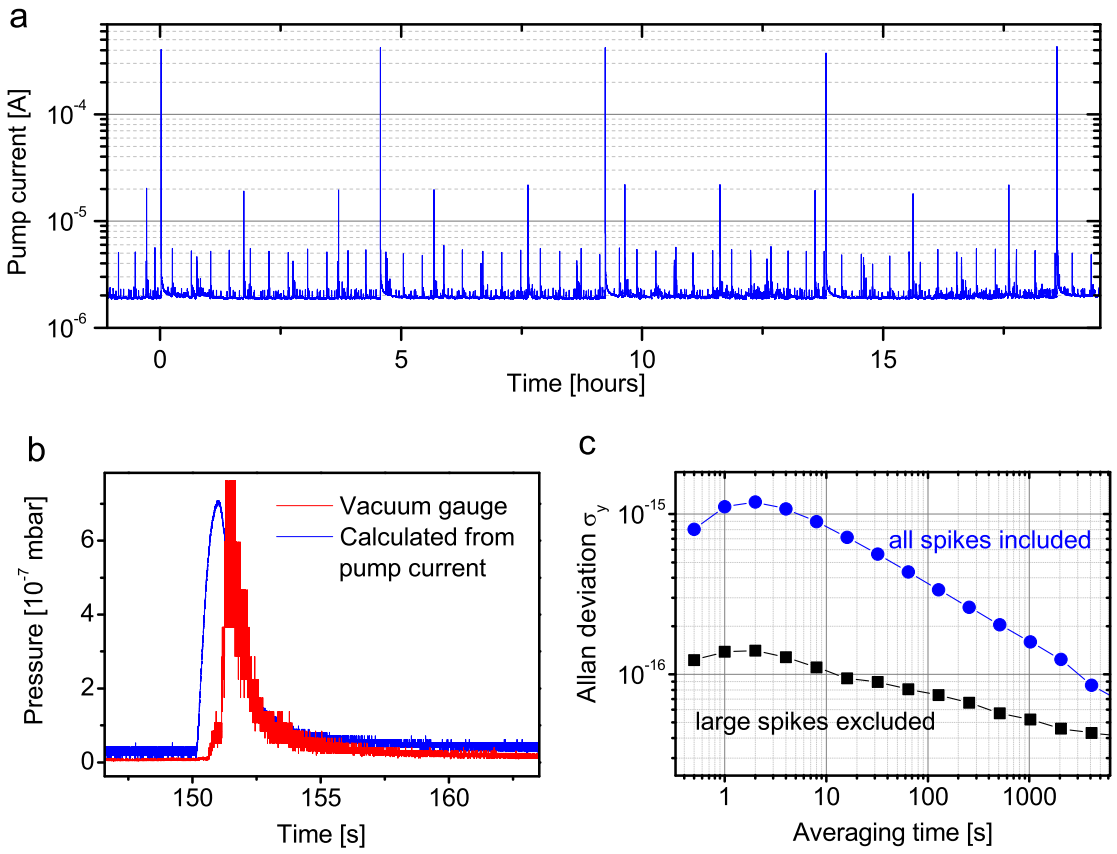

Figure 4.13: **a,** Time record of the pump current of the ion getter pump. The spikes indicate sudden increases of the pressure in the vacuum chamber. **b,** Observed increase of pressure measured with a vacuum gauge (red trace), which is in good agreement with the calculated value from the pump current read out. The increase of pressure of 7.6×10^{-7} mbar would cause a fractional length shift of the cavity of 2×10^{-13}, corresponding to a frequency shift of the cavity-locked laser of ≈ 40 Hz. **c,** Fractional length instability of the resonator determined from vacuum pressure induced length changes. The blue circles show the OADEV calculated from the pump current data shown in Fig. 4.13a). The squares show the OADEV of the same data, but with the large spikes removed.

Fig. 4.13c shows the impact of these pressure bursts to the fractional cavity length and thus to the fractional frequency instability of a cavity-locked laser, calculated from the getter current data shown in Fig. 4.13a. One can see that the vacuum instability can pose a serious limitation to the performance of the laser system. Even if one excludes the large excursions from the data, the instability is above a level of 1×10^{-16} at 1 s averaging time, reaching the expected thermal noise floor of the silicon cavity for averaging times beyond 1000 s.

The causes of these vacuum problems have not yet been identified for sure. A problem with the ion getter pump was excluded, as the spikes still occurred when the pump was shut down for several hours. Most likely, the vacuum problem arises from small real or virtual vacuum leaks along the gas conduction lines, as these spikes can be stimulated by shaking the conduction lines and both period and amplitude show a slight dependency on their position.

4.3 Suppression of residual amplitude modulation

As mentioned in Sec. 2.2, the advantage of the PDH-technique over other laser stabilization techniques is the detection in the RF, making the detection insensitive to DC noise. However, a variety of effects can induce amplitude modulation (AM) at the PDH detection frequency Ω. If in-phase with the phase modulation (PM), the AM induces a DC shift $\Delta\epsilon$ to the demodulated error signal (see Eq. 2.16). Compensating this offset, the PDH control loop would then pull the laser frequency from the center frequency cavity resonance. A time dependency of this AM, denoted as residual amplitude modulation (RAM), then causes a degradation of the laser stability.

RAM can be quantified as the ratio of amplitude of the AM $\Delta\epsilon = (P_{\text{max}} - P_{\text{min}})/2$ to the average power $P_0 = (P_{\text{max}} + P_{\text{min}})/2$. From the PDH error signal (see Eq. 2.16) and the parameters of this work ($\beta = 1.08$, $\Delta\nu_{\text{FWHM}} = 3.2$ kHz) one finds a frequency shift of

$$\Delta f = -\frac{\Delta\epsilon}{\mathcal{D}} = \frac{\Delta\epsilon\Delta\nu_{\text{FWHM}}}{-8P_0J_0(\beta)J_1(\beta)} = 1.2\,\text{kHz}\frac{\Delta\epsilon}{P_0}\,. \tag{4.10}$$

Thus, for thermal noise limited stabilities of $\sigma_y = 4\times10^{-17}$ ($\sigma_\nu = 8$ mHz), RAM must be reduced to a level below 10^{-5}.

A vast number of effects can induce RAM. For instance, parasitic etalons between any reflective surfaces within the optical setup can cause imbalances of magnitude and phase relations of the carrier and the sidebands, which are sensitive to temperature, mechanical vibrations, or the laser frequency [89]. Hence, care was taken in the optical setup to avoid surfaces normal to the laser beam and anti-reflection coatings were employed. In particular, temperature-dependent birefringence variations of the modulator crystal produce RAM, if the input light polarization is not perfectly aligned to one of the principal axes of the electro-optic crystal [90]. The differential propagation time in the principal axes induces a phase shift between the two optical field components, giving rise again for AM due to imbalances between carrier and sidebands, if the subsequent polarizer is not perfectly aligned to one of the principal axes. Hence, in commonly employed free-space modulators, care is taken

with the alignment of the input and output polarizers to match a principal axis of the crystal. However, instabilities of the alignment and RAM arising from spatial inhomogeneities of the modulation field or the crystal itself, intra-crystal etalons or scattering, and fluctuations of the RF power, make it virtually impossible to sufficiently suppress RAM in free-space modulators to match the requirements set by the setup.

In this work, a fiber-coupled $LiNbO_3$ waveguide[22] has been used for phase modulation in combination with an active RAM cancellation system. The scheme of the RAM cancellation procedure is similar to the one presented for free-space modulators [90] and has already been applied with great success in the group of Jun Ye at JILA in Boulder, CO.

The control mechanism is explained in detail in appendix A. Basically, by applying a DC bias voltage in addition to the modulation signal, polarization modulation induced amplitude modulation can be controlled in its magnitude to a high degree. As this amplitude modulation is in phase with the PDH signal, this servo allows to suppress critical RAM of any origin, applying AM with opposite amplitude for compensation.

Employing a waveguide electro-optic crystal brings along various advantages in contrast to a free-space EOM. Due to the small beam diameter the interaction volume within the crystal is well defined, reducing the impact from spatial inhomogeneities to RAM generation. Furthermore, the modulation voltage to achieve the same optical phase shift is orders of magnitude lower. In the employed modulator, a voltage of $V_\pi = 3.5$ V is required to induce an optical phase shift of 180°. This facilitates the control of the phase modulation with respect to modulation depth, modulation frequency, and servo feedback. A misalignment between the principal axes of the crystal and the polarization maintaining input / output fibers of typically $\alpha = 0.5 \ldots 3°$ degrees cannot be avoided. Therefore, without further measures, fiber-coupled phase modulators generally exhibit a relatively large polarization modulation related RAM, typically on the order of $\Delta P/P_0 = 10^{-2}$. However, in the sense of the presented approach, this disadvantage at first glance rather enlarges the dynamic range of the cancellation system.

As shown in Fig. 4.5, RAM was detected behind the output polarizer of the EOM, employing a polarization independent beam splitter. The demodulation phase was adjusted for a maximum sensitivity to polarization modulation induced RAM, i.e. minimizing the signal and then switch the phase by $90°$. Care was taken in the signal processing and filtering, to prevent down-mixing of higher order AM. The error signal was fed to a PI servo amplifier, which supplies an appropriate output signal fed to the EOM for RAM compensation. The servo bandwidth was a few kilohertz. Phase modulator and polarization maintaining fibers were all temperature stabilized within 0.1 K to reduce temperature induced variations of birefringence.

To determine the performance of the RAM cancellation system, the error signals in the RAM and PDH detection were recorded when the laser light was non-resonant with the silicon cavity. As the frequency instability of the unstabilized sili-

[22] Photline MPX-LN-0.1, x-cut, y-prop, z-field

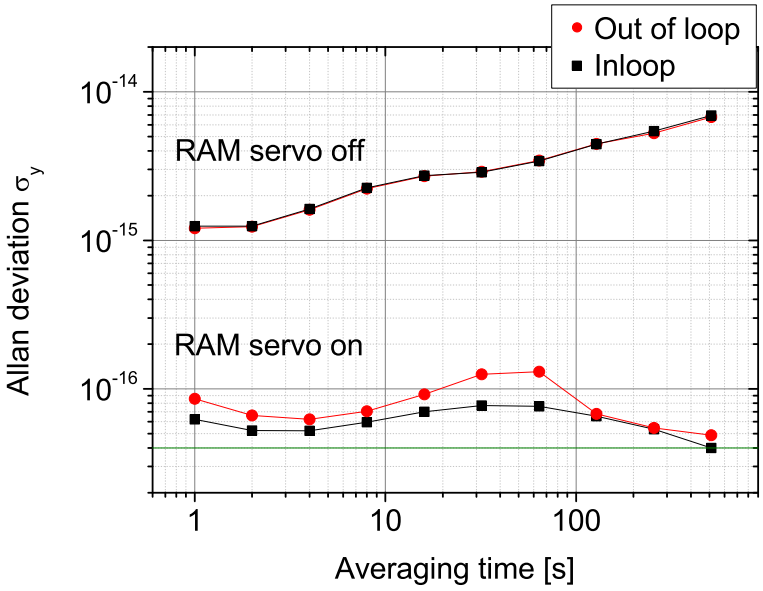

Figure 4.14: Performance and efficiency of the active RAM servo control. The plots with red circles show the RAM induced limitation to the achievable fractional laser stability expressed in the OADEV for the cases the RAM servo is activated or deactivated. Detection limit was below 10^{-17}. The green line indicates the estimated thermal noise floor of the silicon cavity of $\sigma_y = 4 \times 10^{-17}$.

con laser was not sufficient to avoid sporadic coupling of light to the cavity, light of another cavity-stabilized laser has been utilized. The results are depicted in Fig. 4.14, showing the corresponding frequency instability calculated from the observed baseline instability and the slope, i.e. 12 kHz/V, of the error signals. In the case the RAM servo is not activated, RAM would limit the fractional frequency stability of the laser above 10^{-15}. Note that this result already represents an optimized performance. The modulator and the input and output fibers were already temperature stabilized, shifting RAM instabilities to longer time scales. The active servo control improves both the inloop and remote stability by more than one order of magnitude and would enable laser instabilities close to the thermal noise limit below 10 s. Below 100 s, the out-of-loop performance is slightly higher than the inloop performance, indicating non-common RAM from residual etalons in the two branches. In the inloop performance, a conspicuous increase with maximum around 50 s was observed. It may result from an electronic locking offset, as it was observed that the inloop error signal correlated with power fluctuations of the input light, which was delivered with 20 m long non-polarization maintaining fibers to the input polarizer of the EOM. In a previous inloop measurement, where the laser light of the silicon cavity laser had been employed, the increase did not appear.

Further investigations would be needed to determine the currently limiting effects. Problems might also arise from inter-dependencies in birefringence related

RAM generation in the crystal and the polarization maintaining output fiber, reducing the degrees of freedom in the servo control [91]. Thus, it might be helpful to reduce the fiber length to the first polarizer.

However, the present performance of the RAM servo is only a factor of ≈ 1.5 above the expected thermal noise limit of the silicon cavity. Due to the low finesse of the silicon cavity mirrors at TEM_{00}-mode (see Sec 3.3.4), the mirrors of the silicon cavity will be exchanged in the future yielding a cavity linewidth of below 2 kHz. This upgrade already represents an adequate reduction in the sensitivity to RAM. As a final remark, it is important to note that the measurement of the out of loop performance of RAM cancellation excludes effects that occur on cavity resonance only. A coupled cavity-system consisting of the silicon cavity and an external low reflective surface can introduce a significant phase shift to the carrier light, pulling the laser frequency from the cavity resonance, even with perfectly compensated RAM.

Chapter 5

Frequency stability of the silicon cavity stabilized laser

The frequency stability of the silicon cavity stabilized laser has been evaluated for timescales ranging from a second up to months, employing several reference oscillators with operating frequencies from the visible spectrum to the microwave regime.

To determine the short-term stability of this unique system, two conventional high-performance reference laser systems at 1.5 µm have been employed, allowing to perform a three-cornered hat comparison as described in Sec. 2.4. The results of the analysis are presented in Sec. 5.1.

For longer time scales above 100 s, these reference oscillators are not suitable anymore as the frequency instabilities of the ULE-cavity stabilized lasers suffer from long-term frequency deviations. However, various oscillators with excellent long-term stability are available at PTB. For time scales between 100 s and 10 000 s, the $^{171}Yb^{+}$ ion clock has been utilized [4, 92]. For time scales of 10 000 s and beyond, a hydrogen maser operated in the microwave regime has been employed, which was furthermore referenced to a caesium fountain clock [93]. Albeit the operating frequencies of these oscillators or frequency standards are widely separated, the spectral gap to the silicon-cavity laser can be bridged utilizing a femtosecond frequency comb as transfer oscillator [72] (see Sec. 6.2). The results of the frequency comparisons are illustrated in Sec. 5.2.

5.1 Short-term instability

The most crucial noise sources that can affect the short-term performance of the laser locked to the silicon cavity are summarized in Fig. 5.1. Although the performance of the RAM cancellation (see Sec. 4.3) should be further improved, it turned out that in particular the instability of vacuum pressure (see Sec. 4.2.3) represents a vast limitation to the achievable laser stability to a level which is presumably above $\sigma_y = 1 \times 10^{-16}$ for time scales of 1 s – 10 s. The best region to observe fractional frequency instabilities below the 10^{-16} level – which is of major importance to prove that the silicon cavity provides an ultra-low thermal noise floor as expected from theoretical

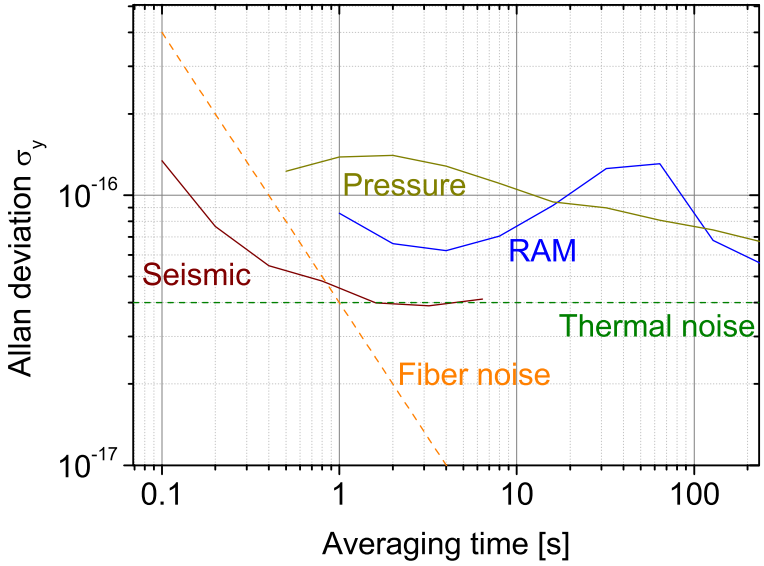

Figure 5.1: Significant noise contributions that affect the short-term stability of the laser locked to the silicon cavity.

estimates (see Sec. 3.2.1) – is at very short time-scales below 1 s. The performance of the fiber noise cancellation employed for the dissemination of the stable laser light does not support thermal noise limited instabilities of $\sigma_y = 4 \times 10^{-17}$ below 1 s, as the white phase noise averages down with $\sigma_y(\tau) = 4 \times 10^{-17}/(\tau/\mathrm{s})$ only. However, as explained in Sec. 2.3, another measure of frequency instability, the modified Allan deviation $mod\sigma_y$, shows a lower dependency on white phase noise, averaging down with $mod\ \sigma_y \propto \tau^{-3/2}$. For instance, employing a high-resolution frequency counter with internal gate time of 1 ms to calculate $mod\ \sigma_y$, fiber noise will average down to $mod\ \sigma_y = 4 \times 10^{-17}$ within 100 ms, instead of 1 s as with the Allan deviation σ_y.

Beyond these aspects, the examination of the frequency instability of the silicon cavity stabilized laser is quite challenging as no reference oscillators with lower frequency instabilities as expected from the silicon laser are available. Nonetheless, as explained in Sec. 2.4, the frequency instability of an outstanding oscillator can be determined in a three-cornered hat comparison, employing two reference oscillators with frequency instabilities not too far from that of the oscillator of examination. For a robust result, the references should be as independent as possible keeping path lengths to the point where the frequency comparison is performed as short as possible. As a large spectral separation would require the employment of a frequency comb, which could introduce additional noise contributions corrupting the independence of the compared oscillators, a direct frequency comparison between three infrared lasers was implemented.

Two ULE-based ultra-stable laser systems have been employed for the comparison, of which one was set up at PTB as a transportable laser system. A second laser became available when a state-of-the-art reference cavity including the vacuum setup was transported from the JILA in Boulder, Colorado, to PTB in Braunschweig and set up by the colleagues from JILA/NIST.

The two systems will be introduced in the beginning of this section, along with the setup of the three-cornered hat comparison. Afterwards, the results of the frequency comparison are presented.

5.1.1 Reference lasers and three-cornered hat setup

The first reference system (Ref. 1) is designed as a transportable laser system set up by Thomas Legero [94]. It employs a relatively short reference cavity with length of 10 cm. The thermal noise of this cavity machined entirely from ULE glass is expected to limit the Allan Deviation at $\sigma_y \approx 7 \times 10^{-16}$. The support points of the horizontally mounted resonator are optimized for inherent vibration immunity utilizing FEM simulation. For PDH-locking, the laser light of a distributed feedback (DFB) fiber laser[1] is phase modulated using a free-space phase modulator. The relatively high cavity-finesse of 316 000 (TEM_{00}-mode) reduces the sensitivity to time-dependent RAM by parasitic effects which made an active RAM cancellation unnecessary.

The second reference system (Ref. 2) was sent from the JILA in Boulder, CO, to PTB and set up by Michael Martin. It employs another ULE cavity with horizontal mounting configuration. The mirror substrate material is fused silica and spacer length is 25 cm. A thermal noise floor of $\sigma_y \approx 2 \times 10^{-16}$ is expected. An Er-doped fiber laser is stabilized to the fundamental transverse mode of the resonator, which shows a comparatively low finesse of 80 000. Thus, an active suppression of RAM as employed for the silicon system (see Sec. 4.3) was mandatory to reduce time-dependent RAM from the utilized fiber-EOM[2].

Standard non-polarization maintaining single-mode optical fibers with length of 10 m (30 m for Ref. 2) deliver the frequency-stable light of each laser system to a central light processing unit, which is located in the same room as the silicon system and Ref. 1. Fig. 5.2 shows a sketch of the three-cornered hat setup containing this unit for superimposing the stable light of the three lasers on a photo detector as well as the subsequent signal processing of the beat signals. In a first step, a fraction of the incoming light is reflected back to each laser system employing 50/50 fiber-splitters and fiber-based Faraday rotator mirrors for fiber noise cancellation. To minimize noise from the subsequent unstabilized optical lengths, all fiber splitters are placed in an airtight box (see photograph in Fig. 5.2). In addition, to best maintain the performance of the silicon system and Ref. 2, both light signals share the same input-splitter, which is subsequently superimposed with the light of Ref. 1 in a third fiber-splitter. The light of all three lasers is detected on an InGaAs photo detector and amplified. The frequencies of the observed beat notes were within 100 MHz – 400 MHz, with $\nu_{\text{Silicon}} > \nu_{\text{Ref. 2}} > \nu_{\text{Ref. 1}}$, providing signal-to-noise ratios above 45 dB (RBW = 100 kHz). To meet the requirements to the input frequency range of the employed high-resolution frequency counter[3], each beat signal was mixed down with a suitable radio-frequency. Each beat signal was filtered out with phase-locked-loop-based tracking oscillators with a locking bandwidth of 1 MHz.

[1] Koheras Adjustik
[2] Eospace, Model PM-0M4-PFA-PFA-S
[3] K+K Messtechnik: model FXE

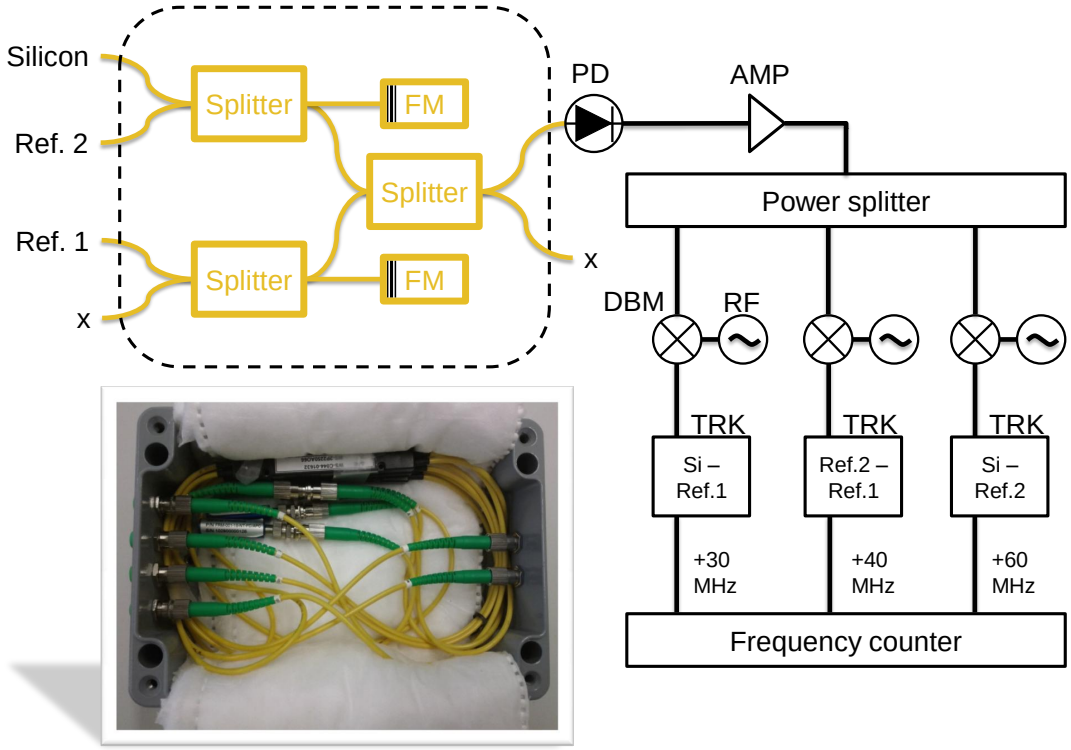

Figure 5.2: Sketch of the three-cornered hat setup. The photograph shows the unclosed fiber setup for superimposing the laser light of the three lasers. FM: Faraday mirror, PD: Photo detector, AMP: Power amplifier, DBM: Double-balanced mixer, RF: Radio-frequency, TRK: Tracking oscillator.

5.1.2 Three-cornered-hat comparison

The individual instability of each laser has been determined in an extensive three-cornered hat (TCH) comparison (see Sec. 2.4), analyzing a full day record of frequency data obtained in phase-averaging mode with a gate time of 100 ms[4]. This mode of counter operation corresponds to an overlapping Λ-mode counting scheme and was chosen in order to evaluate the modified Allan deviation [38, 95]. Fig. 5.3a shows the full data set which reveals that the silicon stabilized laser suffers from the vacuum problems described in Sec. 4.2.3. Within 24 hours, 8 abrupt increases of vacuum pressure occurred which led to frequency excursions of about 50 Hz (see Fig. 5.3b). A closer look in the data shows a medium-sized excursion of 2 Hz (see Fig. 5.3c), of which 28 occurred within 24 hours.

Including the large perturbations in the analysis would have concealed the performance of the silicon laser between these excursions. One could analyze the instability for a time interval of about 3 hours between these perturbations. Instead, the full data set was split into 144 data sets with duration of 10 minutes each. This approach allows to exclude compromised data sets from the analysis while exploiting most of the data for large statistics, which is desirable for a robust three-cornered hat analysis. On the example of an unperturbed data set, Fig. 5.4 illustrates the three-cornered hat procedure which has been performed for all data sets. From the frequency data of the three beats (Fig. 5.4a) the relative instabilities expressed in the modified Allan deviation are calculated (Fig. 5.4b). The resulting individual instabilities from this single data set – including or excluding correlation analysis according to [42] (full symbols or framed symbols, respectively) – is depicted in Fig. 5.4c. For the two reference systems, both results are in very good agreement. However, in case of the silicon cavity, simply applying Eq. 2.33 led to negative variance estimates which occurred for short and long averaging times. Thus, the correlation analysis was included for the full TCH analysis, which was performed by Christian Grebing. The obtained instability curves for each of the 144 data sets are depicted in Fig. 5.5. Data sets that contain a large frequency excursion of about 50 Hz are highlighted in pink color, and those with medium-sized excursions of about 2 Hz are colored dark yellow. It shows that these data sets are clearly distinguishable from the remaining data sets that do not contain one of these frequency excursions. Rejecting only 8 data sets with large spikes from the TCH analysis, the average instability value of the individual instabilities of the three lasers has been calculated. The result is depicted in Fig. 5.6 and the error bars represent the sample standard deviation. First, with short-term stabilities of up to $mod\,\sigma_y = 6 \times 10^{-16}$ and $mod\,\sigma_y = 3 \times 10^{-16}$, respectively, both reference lasers perform close to their estimated thermal noise limit, which is given by $mod\sigma_y \approx 6\times10^{-16}$ and $mod\sigma_y \approx 2\times10^{-16}$ in the modified Allan deviation (see Tab. 2.1). The silicon cavity stabilized laser shows fractional frequency stabilities of $mod\,\sigma_y \approx 1 \times 10^{-16}$ for averaging times between 0.1 s – 1 s, and partially surpasses the estimated thermal noise floor of a corresponding state-of-the-art room-temperature resonator ($mod\,\sigma_y = 1\times10^{-16}$, see Sec. 3.2 and Tab. 2.1 in Sec. 2.3). The correlation analysis showed that average covariances are at least a factor of 10

[4] internal counter gate time: 1 ms

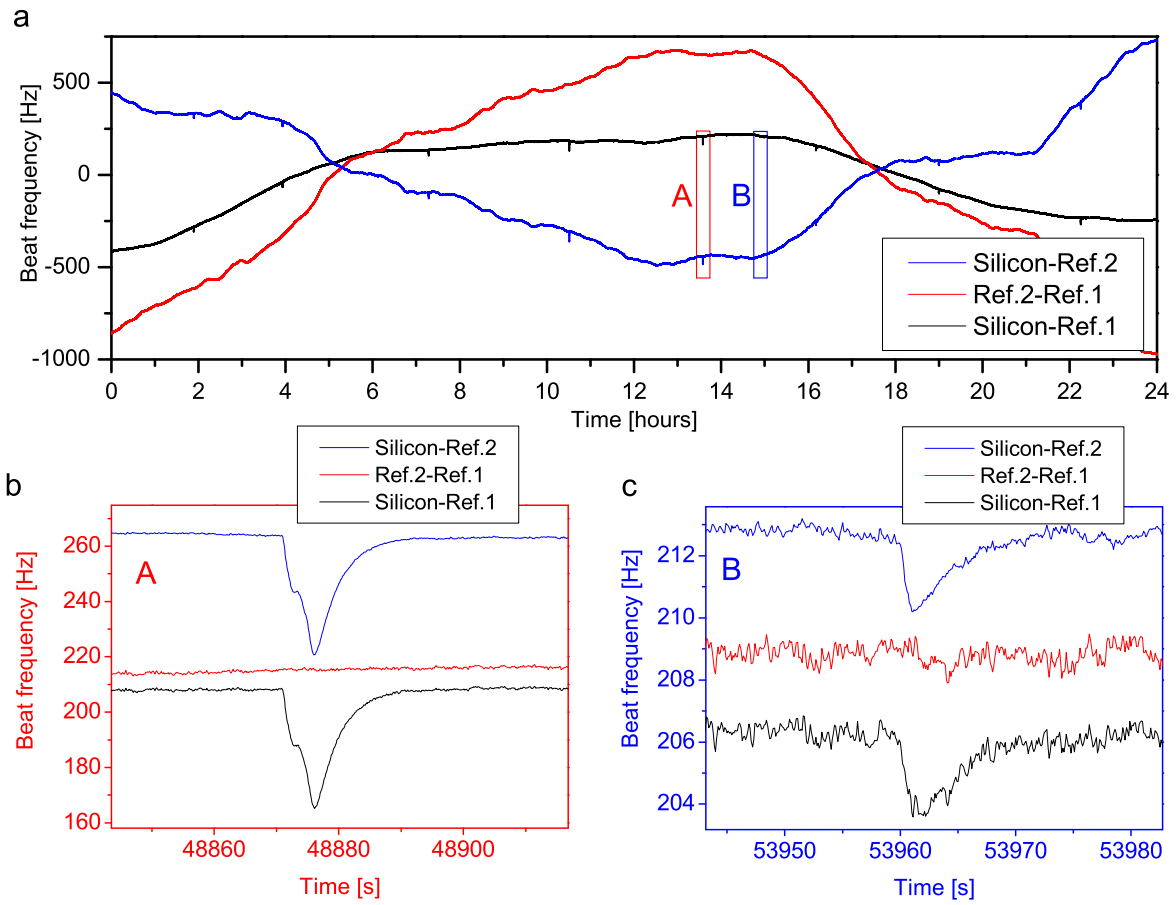

Figure 5.3: Frequency data of the relative beats between the three infrared lasers. **a,** Full day record of frequency data. A linear fit function has been subtracted to remove linear drift (Silicon – Ref. 1: -5.4 mHz/s, Ref. 2 – Ref. 1: -209.6 mHz/s, Silicon – Ref.2: 204.2 mHz/s). **b,** (**c,**) Frequency excursion of ≈ -50 Hz (-2 Hz) of the silicon cavity stabilized laser caused by an increase of vacuum pressure which repeated every three to four hours (once an hour). Both excursions last ≈ 10 s after maximum frequency shift. For illustrative reasons, frequency offsets have been removed in both cases.

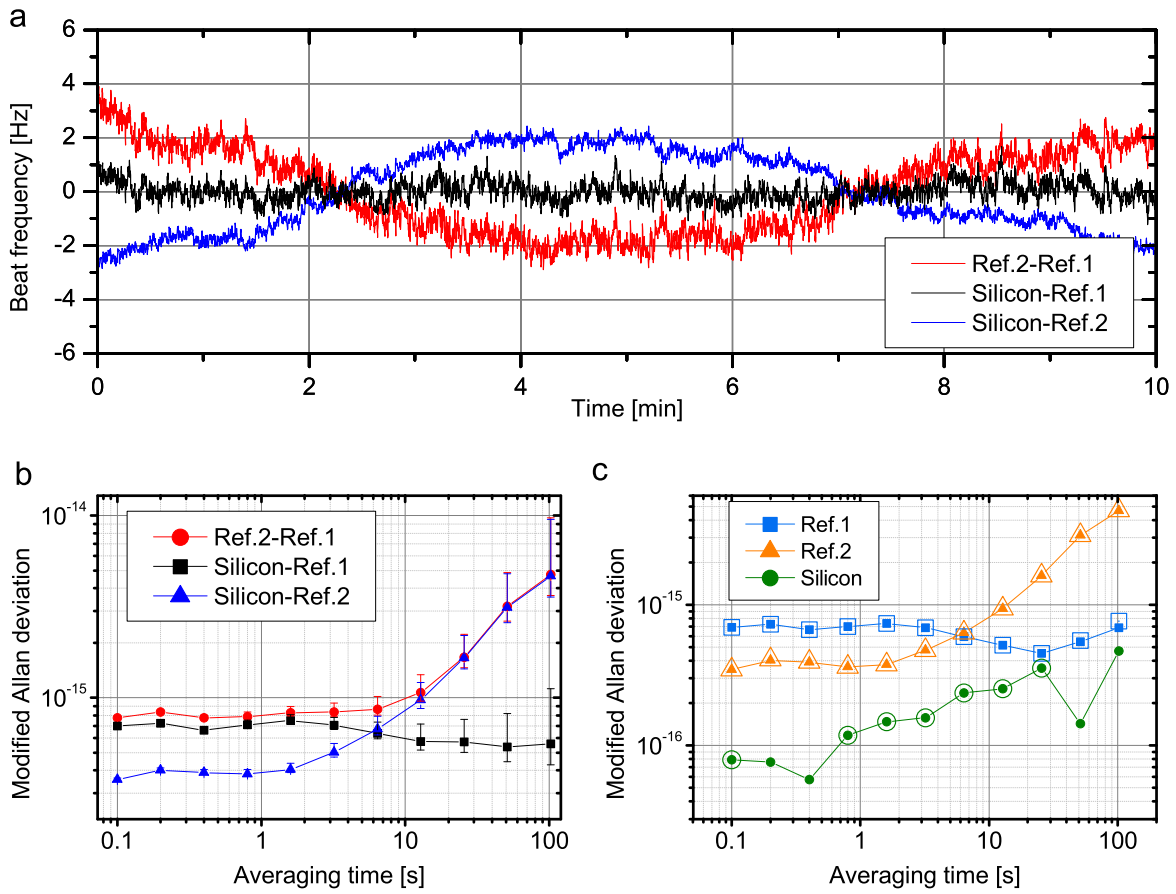

Figure 5.4: Three-cornered hat analysis on the example of a single data set. **a**, Frequency trace of a data set with duration of 10 minutes. **b**, Frequency instability of the three relative beats in Fig. 5.4a expressed in the Modified Allan deviation. **c**, Frequency instabilities of the three lasers derived from the three-cornered hat analysis (see Sec. 2.4) for the relative instabilities shown in Fig. 5.4b. If correlations are not considered according to [42], the estimates for the silicon cavity stabilized laser may become negative (full symbols: with correlation analysis, framed symbols: without correlation analysis.)

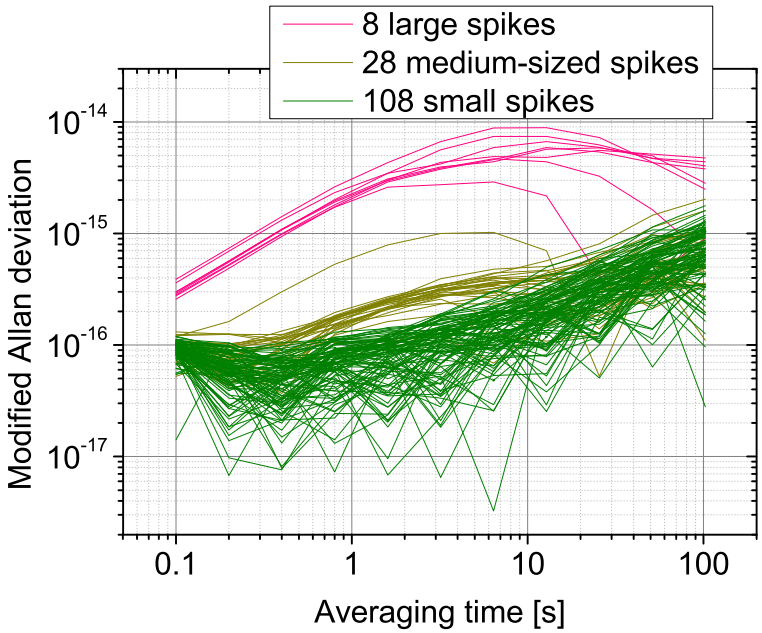

Figure 5.5: Three-cornered hat analysis considering correlations according to [42] for all 144 data sets with duration of 10 minutes each. 8 data sets contain large frequency excursions caused by the vacuum problem (see Fig. 5.3b) and are shown in pink color. Furthermore, 28 additional curves (dark yellow) can be distinguished from the remaining data (dark green), which attribute to the medium-sized frequency excursions originating from smaller abrupt increases of vacuum pressure (see Fig. 5.3c).

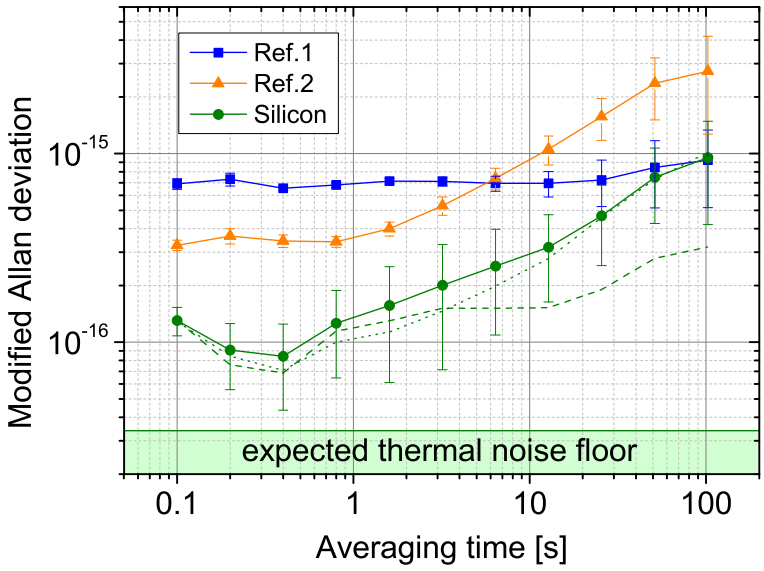

Figure 5.6: Average instability of each infrared laser derived from three-cornered hat analysis of 136 data sets with duration of 10 minutes each. 8 data sets have been rejected for the analysis. The error bars represent the sample standard deviation of the mean values. The green-dotted line indicates the obtained mean value if all data sets with minor abnormalities (28 data sets) are excluded in addition. The green-dashed line shows the obtained mean values, if negative variance are kept in the analysis. The green shaded area represents the estimated thermal noise floor of the silicon cavity.

smaller proving the reliability of the calculated instabilities to the extent given by the error bars. The green-dotted line indicates the result for the silicon laser if the 28 data sets containing the medium-sized spikes are rejected from the analysis in addition, leading to slightly lower instabilities up to 10 s. Between 10 s and 100 s, the instability in both cases "follows" that of Ref. 2, arousing suspicion that the analysis produces unreliable results for higher averaging times.

In later investigations carried out by Christian Grebing, three microwave oscillators with well known performances similarly distributed as in the situation found for the laser comparison have been utilized, revealing a similar instability increase for the best performing oscillator in the utilized TCH analysis which takes into account correlations. As the oscillators can be considered to be highly independent, one would expect that the TCH analysis would reproduce the individual instabilities, no matter if correlations are taken into account or not. However, this was not the case: negative variances occurred when the correlation analysis was not performed. This led to the conclusion, that the occurring negative variances should be interpreted as statistics, which occur as a direct consequence of an increasing uncertainty due to a large gap between the most stable oscillator and the other two references as well as fewer data available for longer averaging times. Thus the negative variances should fully contribute to the statistics, calculating the average variance before taking its square-root to calculate the deviation. Indeed, this procedure led to a better reconstruction of all individual oscillator instabilities. The other way around, this means that the correlation analysis originally used to minimize the impact of correlations incorrectly induced correlations, which led to under- and overestimates of the best performing oscillator.

Performing this alternative analysis for the laser comparison for the case all data sets containing large and medium-sized spikes are rejected, one finds that the instability of the silicon cavity stabilized laser remains at an instability level of $mod\,\sigma_y = 1 \ldots 3 \times 10^{-16}$ for averaging times up to 100 s (see green-dashed line in Fig. 5.6). This result is in good agreement with the observations in the frequency comparison with the $^{171}Yb^{+}$ ion clock (see Sec. 5.2).

5.1.3 Laser linewidth

As in Sec. 5.1.2 the lowest short-term instability was observed in the beat note between the silicon cavity stabilized laser and Ref. 2, one would expect the narrowest optical linewidth between these two lasers. For data acquisition on a FFT-analyzer[5] and a digital oscilloscope, the beat signal was mixed down and drift compensated utilizing a direct digital synthesizer (DDS). The results are depicted in Fig. 5.7. The beat note between the two lasers shows a typical FWHM of 49(4) mHz which is the lowest linewidth reported for any laser system [15]. Assuming a Gaussian line profile and the silicon cavity stabilized laser to be more stable, this gives an upper limit for this laser's linewidth of 35 mHz. Typically, 70% of the power is contained in a Lorentzian with linewidth of the FWHM.

[5]HP 3561A

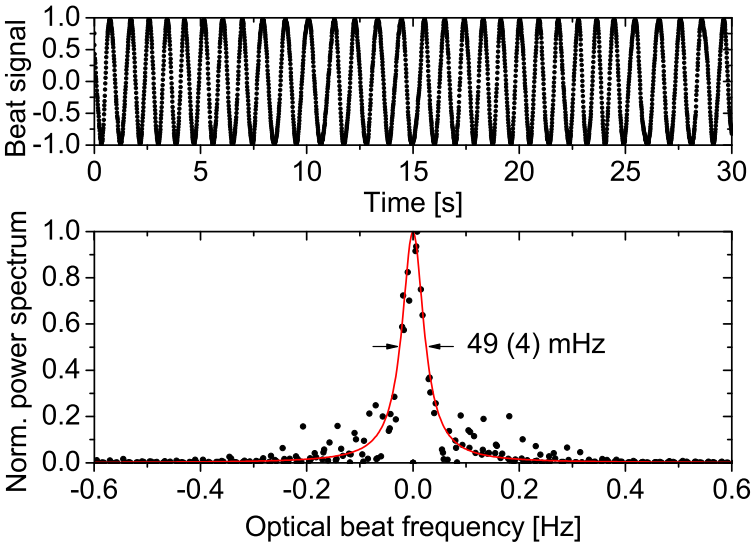

Figure 5.7: Optical heterodyne beat between the silicon cavity stabilized laser and Ref. 2. **Top:** Beat signal mixed down close to DC and recorded with a digital oscilloscope. **Bottom:** Normalized power spectrum of the beat signal. The red trace shows a Lorentzian fit with FWHM of 49(4) mHz on the combined data from five consecutive recordings. A linear drift of 250 mHz/s was removed from the beat signal utilizing a DDS.

5.1.4 Frequency noise spectrum

Fig. 5.8 shows the PSD of frequency fluctuations S_ν between the silicon cavity stabilized laser and Ref. 2 calculated from a time-record of the beat signal with a digital oscilloscope[6]. For low frequencies, the frequency noise spectrum is dominated by flicker frequency noise which is close to the expected thermal noise limit of Ref. 2. For higher Fourier frequencies a minimal white noise floor of low 10^{-2} Hz/$\sqrt{\text{Hz}}$ is reached. Frequency spikes in the acoustic range refer to whistling which originates from the nitrogen gas flow in the flexible vacuum-insulated tubes. They vary both in amplitude and frequency in dependence of the filling level of the nitrogen dewar. However, these spikes are very sharp and therefore have a negligible impact to the performance of the silicon cavity stabilized laser. The spikes around 30 Hz and 50 Hz presumably attribute to a large extent to the seismic noise floor of the silicon system (see Fig. 4.12). The higher impact of vibrational noise than expected from the noise measurement might originate from the fact that the nitrogen gas conduction line has no direct mechanical contact to the vibration isolation, leading to a higher PSD $S_a(f)$ at the cryogenic shield than measured on the isolation table.

[6]LeCroy WaveRunner 620Zi

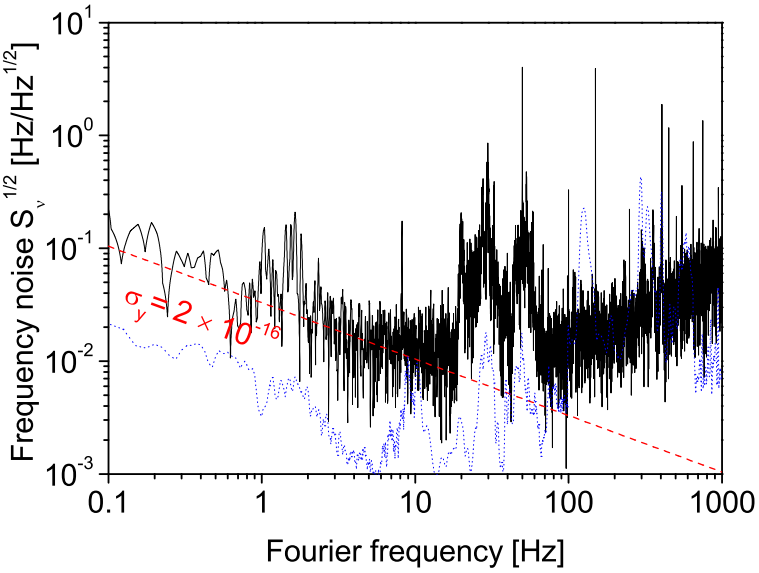

Figure 5.8: Frequency noise spectrum of the beat signal between the silicon cavity stabilized laser and Ref. 2. The red line indicates the theoretical estimate of the thermal noise of Ref. 2. The blue dotted line shows the expected vibration-induced frequency noise of the silicon-cavity laser.

5.2 Long-term instability and linear drift

The long-term performance of the silicon cavity stabilized laser has been determined in frequency comparisons with long-term stable microwave and optical reference oscillators, i.e. an active hydrogen maser and the $^{171}Yb^+$ ion clock at PTB. As the operating frequencies of these oscillators are widely separated, on the order of 10^{14} Hz, the frequencies of the beat notes with the silicon cavity stabilized laser would be too high for direct detection on a photo diode. However, a frequency comparison can be realized utilizing a femtosecond frequency comb which is stabilized to the hydrogen maser (see Sec. 6.2). Each comb mode provides the instability of the hydrogen maser, hence detecting the beat note of the silicon laser with a neighboring comb mode reveals the relative instability between the two oscillators. Furthermore, the frequency comb enables comparison of the two optical oscillators following the transfer oscillator concept [96] (see Sec. 6.2).

The results are depicted in Fig. 5.9. The observed frequency instability against the active hydrogen maser is completely restricted from the performance of the maser up to 10^4 s. In the inter-optical comparison, the instability shows a flicker floor of $\sigma_y = 5 \ldots 6 \times 10^{-16}$ which coincides with the estimated thermal noise floor of the cavity-stabilized laser system employed in the $^{171}Yb^+$ ion frequency standard. Note that for this frequency comparison the large frequency excursions originating from the pressure bursts have been excluded as accomplished in the three-cornered hat comparison (see Sec. 5.1.2). The instability averages down at time-scales > 10 s where the servo lock of the interrogation laser to the Yb^+ ion is in effect. Thus, up to this time scale the observed instability gives an upper limit for the instability of the

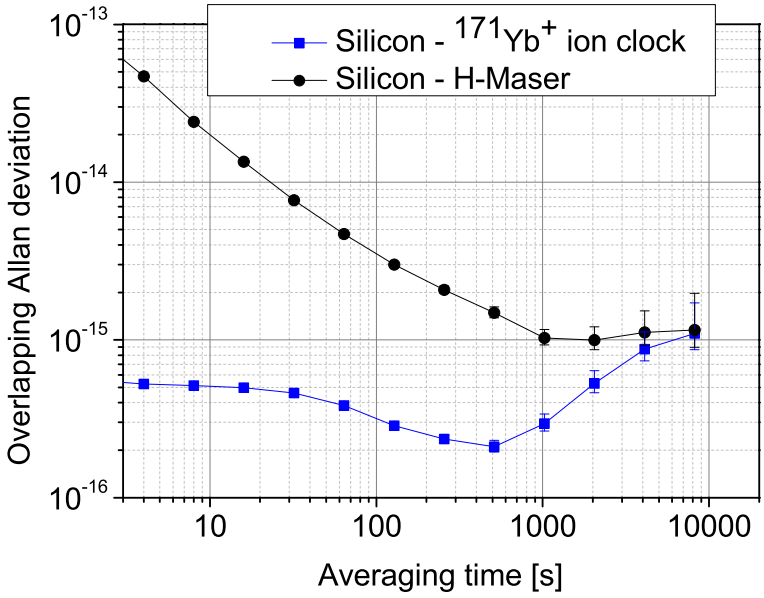

Figure 5.9: Overlapping Allan deviation obtained from frequency comparison with a hydrogen maser (black trace, circles) and the $^{171}Yb^{+}$ ion clock (blue trace, squares). The silicon cavity stabilized lasers matches up with the performance of the ion clock up to a few hundred seconds.

silicon cavity stabilized laser. The observed instability for time scales $> 100\ s$ reveals the instability of the silicon cavity, which reaches a minimum of $\sigma_y(512\ \mathrm{s}) = 2\times10^{-16}$. This result is in good agreement with the derived instability of the silicon cavity laser presented in Sec. 5.1.2, if negative variances are kept within the analysis. The reason for the instability increase of the silicon laser up to the day scale is not yet known. It may be caused by variations of the ambient temperature or slow vibrations on the vibration isolation table.

A hydrogen maser has been employed for characterization of the long-term behavior of the silicon cavity stabilized laser. Fig. 5.10 shows a 60 day frequency record of the beat signal of the silicon cavity stabilized laser with a comb line of the hydrogen maser stabilized femtosecond comb. Frequency excursions visible at these time-scales can be attributed to the silicon system, as the maser provides very low frequency drifts of 4 µHz/s or 0.3 Hz/day with respect to a carrier frequency of 194 THz. The fast increase of the beat frequency in the beginning of the plot results from the silicon cavity being cooled down to its desired temperature of operation at 124.2 K (see Sec. 3.2.2). As no temperature sensor was attached to the cavity, the tuning of the cavity temperature could only be performed observing the beat frequency. Note that the required operating temperature of the cryogenic shield to operate the silicon cavity at 124.2 K differs from the operating temperature found in the thermal-expansion measurement (see Sec. 4.2.1), as in that measurement the passive shield was not employed to shorten the measurement time. As further shown in Fig. 5.10, the silicon cavity temperature decreased below its temperature of minimum length and the cryogenic shield temperature has been tuned in several approximations to

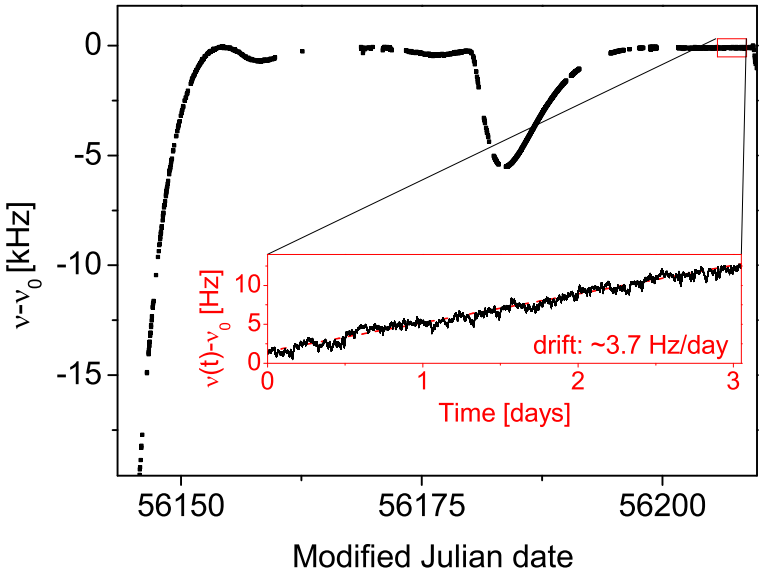

Figure 5.10: Beat frequency of the silicon cavity stabilized laser with a hydrogen maser stabilized femtosecond frequency comb. The inset shows the lowest linear frequency drift of the silicon cavity stabilized laser observed in a period of 3 days against a hydrogen maser. The data has been smoothed with a moving averaging window of 1000 s. The slope of the linear fit gives a drift of 3.7 Hz/day, where the drift of the maser contributes with 0.2 Hz/day (derived from comparison with a caesium fountain clock).

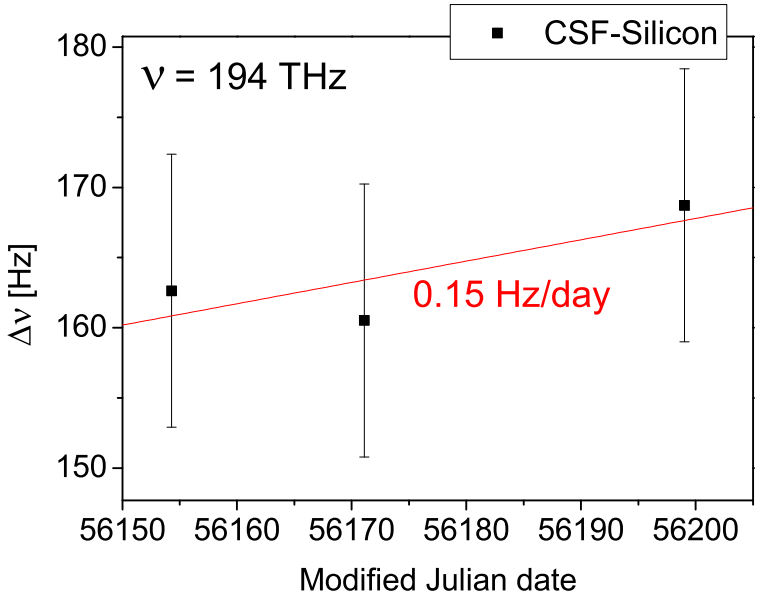

Figure 5.11: Deviation of the minimum eigenfrequency of the silicon cavity when it passes its zero-crossing in thermal expansion. The average frequency drift $\Delta\nu$ of the silicon cavity zero-crossings is 0.15 Hz/day. This value is a factor of two below the drift of the active hydrogen maser.

drive the temperature of the cavity as close as possible to 124.2 K.

A linear frequency drift of 11.1 Hz in three days was observed against the hydrogen maser. Taking into account the drift of the hydrogen maser derived from a frequency comparison with a caesium fountain clock, the absolute value for the silicon cavity stabilized laser is 3.5 Hz/day. This value corresponds to a (fractional) frequency drift of 40.5 µHz/s (2×10^{-19}/s). The demonstrated long-term drift reflects a large improvement compared to conventional room-temperature optical cavities, which suffer from drift rates on the order of 10^{-16}/s [15], induced by restructuring processes in the amorphous glass material. Compared to cryogenic sapphire cavities, the observed frequency drift is a factor of five lower than the average drift observed over a time period of 6 months (3 kHz) [26]. The cryostat is not yet developed to a state where a failure free operation is guaranteed for good, preventing a direct estimation of a systematic long-term drift of the silicon cavity length at very long time-scales, e.g. due to aging of the optical contact of the mirrors to the spacer or imperfections in the crystal structure. Nonetheless, one can draw a conclusion from comparing the frequency values of the silicon cavity stabilized laser with the caesium fountain clock at the point where the coefficient of thermal-expansion of the silicon cavity is zero. The frequency values of the silicon cavity stabilized laser at three crossings are depicted in Fig. 5.11. The average frequency drift was 0.15 Hz/day. This value is half of the drift of the active hydrogen maser, which was 0.32 Hz/day in the same time interval. In fractional units, the drift of the minimum length of the silicon cavity was 9×10^{-21}/s.

As the reliability of the cryostat is continuously improved, e.g. by employing a

computer independent backup for temperature control, it seems feasible that with a silicon cavity a laser system can be realized, which provides ultimate frequency stability at both short and long time-scales.

Chapter 6

Application in optical frequency standards

With fractional inaccuracies of 8.6×10^{-18} [2] and instabilities of $\sigma_y(\tau) = 4 \ldots 5 \times 10^{-16}/\sqrt{\tau/\mathrm{s}}$ [15] optical atomic clocks are the most advanced instruments for measurements of time and frequency. Crucial for the performance of an atomic frequency standard is the quality of the local oscillator that probes the atomic reference. Particularly optical lattice clocks, which would in principle support quantum-projection noise limited instabilities below $\sigma_y = 10^{-17}/\sqrt{\tau/\mathrm{s}}$, suffer from insufficient performance of the interrogation laser [97–99].

This chapter describes the implementation of the silicon cavity stabilized laser system as local oscillator for optical atomic clocks. As absorption restricts the operation of the silicon cavity stabilized laser to the infrared with an optimum transmission at $1.5\,\mu\mathrm{m}$, the concept of an ultra-stable silicon cavity can not be utilized directly in order to improve optical clocks with transition frequencies in the visible part of the optical spectrum. However, with the development of optical frequency combs a powerful technology became available which allows to transfer the stability from an arbitrary wavelength to another covered by the frequency comb [72].

After a brief introduction to the basics of optical frequency standards, the results of the implementation of the silicon cavity stabilized laser system into the ^{87}Sr optical lattice clock at PTB are presented.

6.1 Optical atomic clocks

6.1.1 Principle of optical atomic clocks

Two concepts of optical atomic clocks are currently being investigated in a worldwide effort as a possible successor for the well-established microwave caesium fountain clocks, where the atomic reference is either a trapped ion or an ensemble of neutral atoms trapped in an optical lattice. Various elements with differing dependencies to external perturbations are investigated. On the side of ion clocks, the elements Hg^+, Al^+, Yb^+ and Sr^+ are subject of research, while in neutral lattice

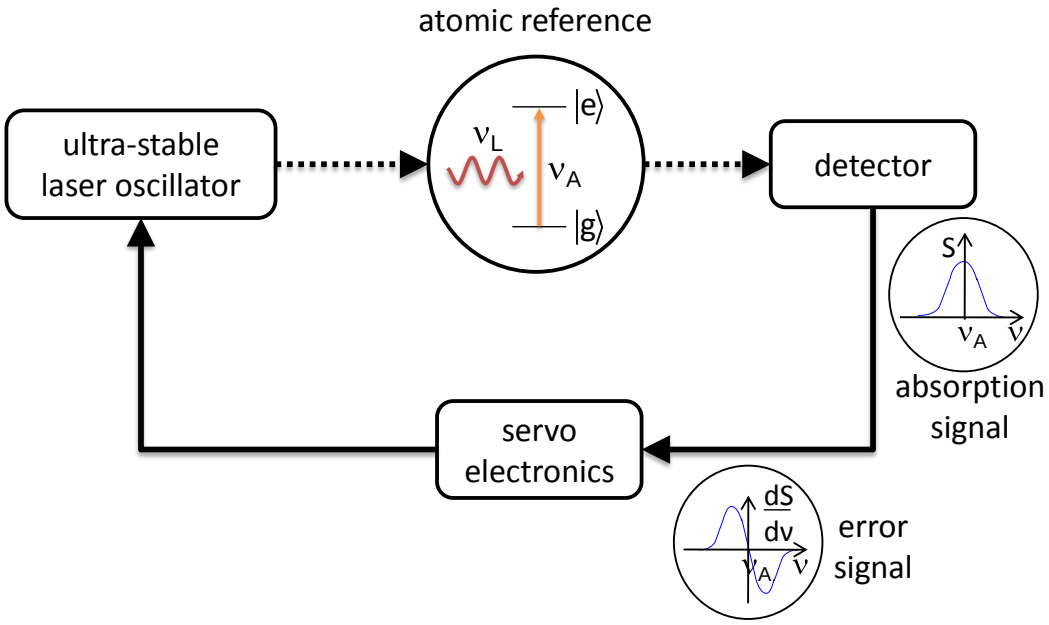

Figure 6.1: Schematic working principle of an optical atomic clock.

clocks the elements Sr, Yb, Mg and Hg are investigated as promising candidates for an optical frequency standard. A schematic of the working principle of an optical atomic clock is depicted in Fig. 6.1. An interrogation laser is used to probe an optical transition of an atomic reference. The detected absorption signal allows to derive the frequency offset of the laser light ν_L from the transition frequency ν_A and thus to steer ν_L to ν_A. An optical, highly stable "clock" frequency is generated this way and its absolute value in Hertz can be traced back to the microwave primary frequency standard utilizing femtosecond frequency combs (see Sec. 6.2). As each clock cycle with duration T_c contains cooling and preparation of the atoms, atomic clocks are operated in a discontinuous mode. Thus, only a fraction of each clock cycle is available for spectroscopy on the atomic transition.

Various effects induce shifts from the ideal, unperturbed resonant frequency ν_A and – if not stable in time – degrade the long-term stability of an optical clock. This problem can be addressed by taking care that the experimental parameters are kept as constant as possible. However, to suit as frequency standard, it is indispensable to determine the unperturbed optical frequency ν_A as accurately as possible. Thus, a quantitative evaluation of the systematic effects is vital to reduce uncertainties.

6.1.2 Stability of optical atomic clocks

The ultimate frequency stability achievable due to the quantum-projection noise limited signal-to-noise ratio (SNR) [100] is given by [33]

$$\sigma_y(\tau) = \kappa \frac{1}{Q} \frac{1}{\mathrm{SNR}} \sqrt{\frac{T_c}{\tau}} \tag{6.1}$$

where the line quality factor $Q = \nu_A/\Delta\nu$ is the ratio of atomic transition frequency and resolved linewidth and κ is a factor close to unity which depends on the interrogation scheme [33]. Single-ion clocks easily reach this limit [2, 92] due to their low signal-to-noise ratio (SNR $= 1$) and a reduction of clock instability is possible only by resolving narrower linewidths. As $\Delta\nu \propto 1/T_p$ ($T_c \approx T_p$ for ion clocks), this sets high demands to the clock laser which needs to provide a sufficient coherence time τ_c, which is approximately related to the frequency instability of the laser by $2\pi\nu_0\sigma_y\tau_c = 1$ [101]. Thus, reducing thermal noise in the optical cavities as limiting factor in the laser stability will allow improvements for single-ion clocks.

The advantage of optical lattice clocks is the large number N of atoms (typically $10^4 - 10^6$) that are probed simultaneously. If there are no correlations between the atoms, the signal-to-noise ratio SNR increases $\propto \sqrt{N}$. This lowers the quantum-projection-noise-limit by two to three orders of magnitude compared to a single-ion clock. However, this level of instability has not yet been demonstrated for any optical lattice clock. The reason originates from the fact that the preparation of the atomic ensemble is much more elaborate than in an ion clock. While an ion generally remains trapped after an interrogation cycle, a neutral ensemble is lost and needs to be recreated. The recurring steps for the trapping of the atoms increase the dead-time T_d where no information of the frequency excursions of the clock laser are obtained. This loss of information leads to a degradation of clock stability due to aliasing of laser frequency noise at harmonics of the cycle frequency $1/T_c$. This so-called "Dick effect" [97, 98, 102] limits the fractional frequency stability of an optical frequency standard to an Allan variance of

$$\sigma_y^2(\tau) = \frac{1}{\tau}\sum_{m=1}^{\infty}\frac{|g_m|^2}{g_0^2}S_y(m/T_c)\ , \tag{6.2}$$

where $S_\nu(m/T_c)$ is the frequency noise PSD of the free-running laser oscillator at Fourier frequencies $f = m/T_c$. The weighting coefficients $\frac{|g_m|^2}{g_0^2}$ are given by

$$g_m = \frac{1}{T_c}\int_0^{T_c} g(t)e^{-2\pi imt/T_c}\mathrm{d}t \tag{6.3}$$

where $g(t)$ describes the sensitivity of the excitation probability to frequency excursions of the probe laser. The shape of $g(t)$ depends on the employed interrogation scheme and is shown in Fig. 6.2a for the commonly used Rabi interrogation. The "pulse like" sensitivity function in the time domain leads to side lobes in the weighting coefficients $|g_m|^2/g_0^2$ in Fourier space (see Fig. 6.2b). The lower the fraction $d = T_p/T_c$, often denoted as "duty cycle" d, the more harmonics of $1/T_c$ rise up.

Due to the lower duty cycle compared to ion clocks, more higher-frequency noise of the local oscillator is inscribed to the clock stabilization of an optical lattice clock. With typical cycle times around 1 s, in particular low-frequency noise is weighted in, in a regime, where thermal noise of the optical reference cavities typically rises

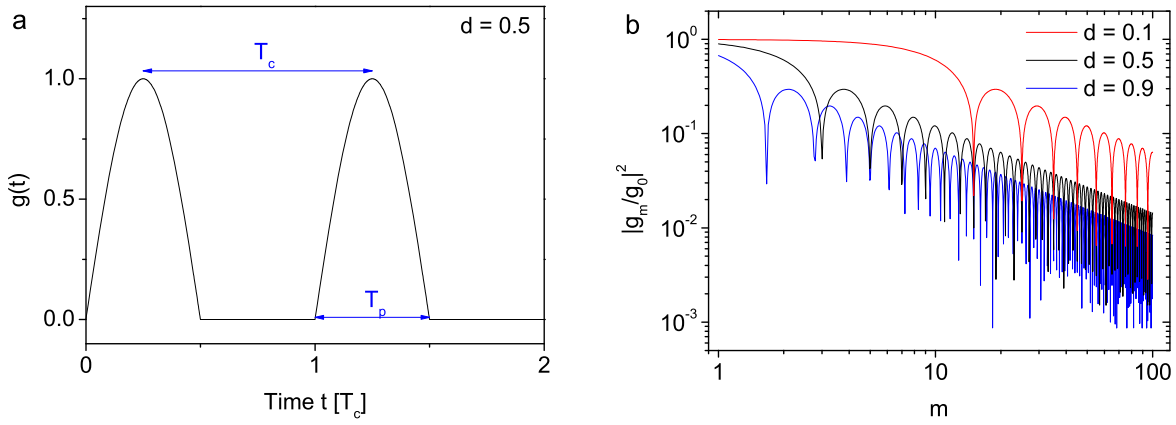

Figure 6.2: Time (**a**) and Fourier-domain (**b**) representation of the Dick sensitivity function for a Rabi-type interrogation scheme. The lower the duty cycle, the more local oscillator noise at harmonics of the inverse cycle time is aliased to the clock stabilization.

up with $1/f$. Note that increasing the duty cycle by increasing the probe time, if supported by the laser, will also lower the Fourier frequencies $f = m/T_c$ at which frequency noise of the local oscillator is weighted in. Hence, thermal noise of higher magnitude at lower Fourier frequencies contribute to the Dick effect. The strength of this effect is depicted in Fig. 6.3. Even with a hypothetical assumption that the probe time could be arbitrarily chosen, the Dick limit from thermal noise of the reference resonator is dominated by the increasing thermal noise of the reference cavity. There exist alternative interrogation schemes such as the Ramsey interrogation, which is less sensitive to low-frequency laser noise, in particular for duty cycles above $d = 0.9$ [103]. However, as duty cycles of that order are still out of reach and assuming that the dead-time cannot be further reduced, currently the only way to improve the stability of optical lattice clocks is to reduce the limitation of ultra-stable lasers from thermal noise.

Although the silicon cavity laser system is not yet limited by thermal noise, the demonstrated laser performance already represents an improvement by an order of magnitude with respect to the local oscillator [13] employed in the ^{87}Sr optical lattice clock [104] at PTB. The instability of the clock laser is limited to a flicker floor of $\sigma_y(1\,\mathrm{s}{-}10\,\mathrm{s}) \approx 2{\times}10^{-15}$, close to the estimated thermal noise floor of $\sigma_y \approx 9{\times}10^{-16}$ of the employed reference cavity. Thus, utilizing the silicon cavity stabilized laser should significantly improve the clock stability.

Bridging the widely separated operation frequencies (Si: 194 THz, Sr: 429 THz) can be accomplished utilizing a broadband femtosecond frequency comb as transfer oscillator. Such transfers have been previously accomplished with success for instabilities in the range of 10^{-15} [105–107]. However, on a level of 10^{-16}, the question arises if the increased complexity decreases the reliability of such a compound system and to what extend the additional pathways and steps in light and signal processing impair the transferred stability.

Such a transfer to the ^{87}Sr optical lattice clock at PTB has been recently accom-

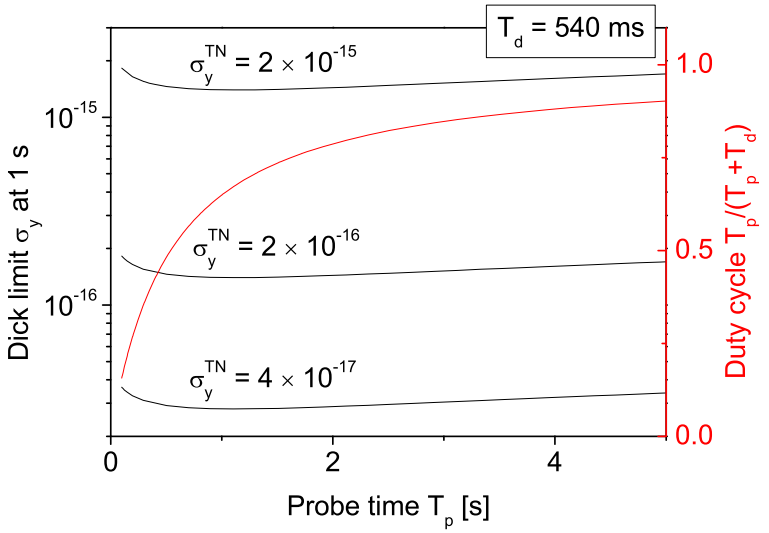

Figure 6.3: Dick limited Allan deviation $\sigma_y(\tau = 1\,\mathrm{s})$ for different thermal noise floors σ_y^{TN} of the local oscillator with respect to the probe time for Rabi interrogation. The dead-time T_d due to preparation of the atoms was kept constant at 540 ms, a typical value in the strontium lattice clock at PTB. Even if the probe time T_p could be arbitrarily chosen to increase the duty cycle, the Dick limit is only moderately decreased and even rises up for duty cycles $d \gtrsim 0.7$ due to the higher thermal noise contributions at lower Fourier frequencies.

plished in a collective effort and the results are presented in [108]. The following sections of this chapter will introduce the transfer oscillator technique and present the improvements on the strontium clock. For more details to the setup of the optical lattice clock see [13, 104, 106, 109, 110].

6.2 Stability transfer to the ^{87}Sr optical lattice clock

Optical frequency combs have become an indispensable tool in optical frequency metrology which links the microwave regime with the optical regime. A frequency comb emits trains of ultra-short laser pulses with durations in the order of femtoseconds, periodically separated by T_{rep}. In the frequency domain, this emission spectrum consists of discrete modes with frequencies

$$\nu_m(t) = m f_{\mathrm{rep}}(t) + f_{\mathrm{ceo}}(t)\ , \tag{6.4}$$

that are given by the mode number m, frequency spacing $f_{\mathrm{rep}}(t) = 1/T_{\mathrm{rep}}$ and carrier envelope offset frequency $f_{\mathrm{ceo}}(t)$. $f_{\mathrm{rep}}(t)$ and $f_{\mathrm{ceo}}(t)$ generally fluctuate in time, but can be detected and servo locked [96, 111] to an RF reference. If the reference frequency can be traced back to the primary frequency standard, this allows to determine the absolute frequency value of an optical frequency ν by measuring the beat frequency Δ between the optical frequency and the nearest comb mode with

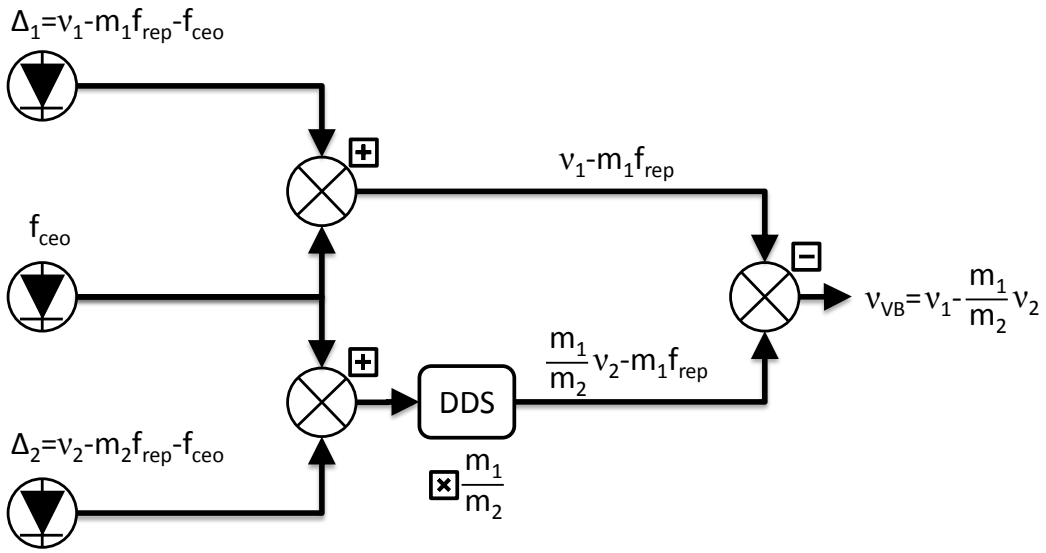

Figure 6.4: Schematic of signal processing for generation of a virtual beat between two optical frequencies ν_1 and ν_2.

mode number m according to

$$\nu = m f_{\text{rep}} + f_{\text{ceo}} + \Delta \ . \tag{6.5}$$

In the ideal case, each comb line provides a fractional frequency stability, which corresponds to that of the used RF reference. Thus, to compare two widely separated optical frequencies ν_1, ν_2 that provide higher stabilities, further measures are needed to avoid being limited by the microwave reference. One approach is to stabilize the frequency comb to one of the optical sources [112]. However, Telle et al. [72] showed that with appropriate signal processing inter-optical frequency comparisons can be performed even with a free-running frequency comb, exploiting the correlations of $f_{\text{rep}}(t)$ and $f_{\text{ceo}}(t)$ with the frequency fluctuations of each optical comb mode. The required processing steps are illustrated in Fig. 6.4. In a first step, each beat signal Δ_1, Δ_2 is fed to a mixer together with the tracked offset frequency f_{ceo}. Taking the sum of the mixer outputs f_{ceo} is removed from both signals. Using a direct digital synthesizer (DDS) the lower-branch signal is multiplied by m_1/m_2 and subtracted from the upper-branch signal. One obtains a signal

$$\nu_{\text{VB}} = \nu_1 - \frac{m_1}{m_2}\nu_2 \tag{6.6}$$

which is independent of f_{rep} and f_{ceo} within the tracking bandwidth of a few Megahertz of the employed RF electronics. This "virtual beat" follows only the frequency excursions of the optical frequencies ν_1 and ν_2, projected to the vicinity of ν_1. Thus, using the frequency comb as transfer oscillator allows to directly measure the instability of two widely separated optical frequencies. Going one step further, it also enables to use the highly stable laser with output frequency ν_2 as reference, locking the second laser with output frequency ν_1 to the virtual beat signal.

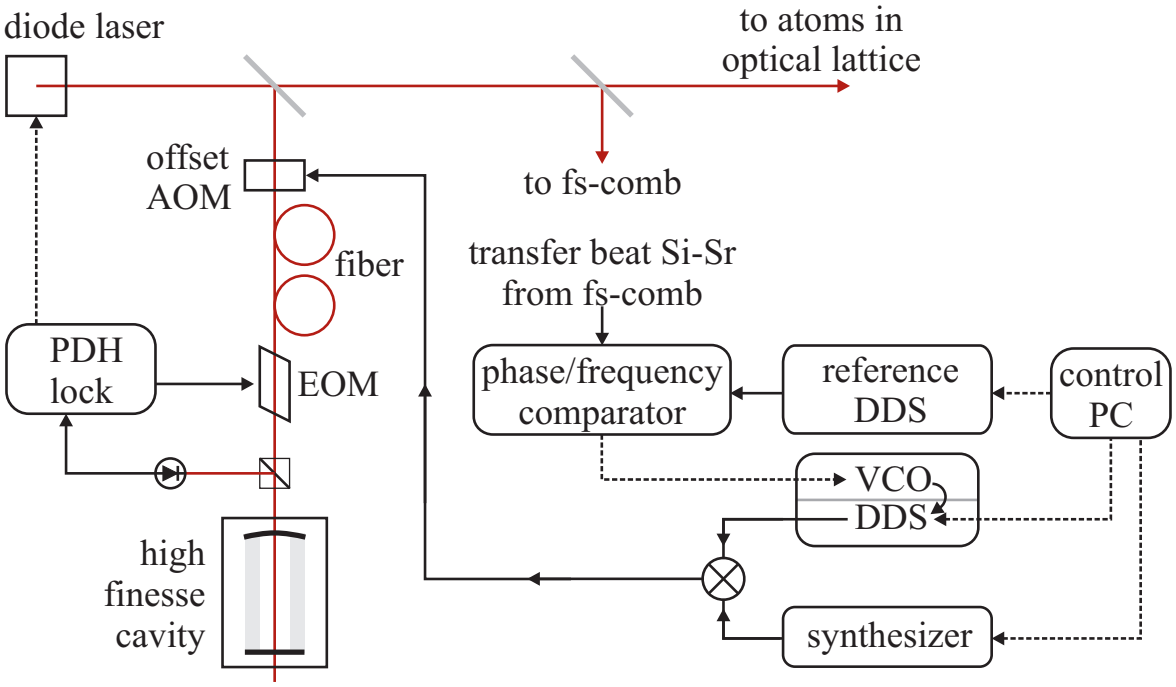

Figure 6.5: Schematics of the lock of the Sr clock laser to its reference resonator (left; PDH: Pound-Drever-Hall; AOM: acousto-optical modulator; EOM: electro-optical modulator) providing a short-term stability of $\sigma_y \approx 2 \times 10^{-15}$ at a few seconds. The RF driving the offset AOM is generated by mixing of two computer controlled sources. To phase lock the clock laser to the master laser, an error signal is generated in a phase/frequency comparator, to which the transfer beat from the femtosecond frequency comb and a stable RF are fed. The figure is taken from [108].

Such a stability transfer has been accomplished to stabilize the clock laser of the strontium lattice clock ($\nu_1 = 429$ THz) to the silicon cavity stabilized laser (ν_2 =194 THz). The setup is depicted in Fig. 6.5. From phase comparison of the virtual beat with a stable RF reference an error signal is generated which is used to steer the radio frequency driving the offset AOM between clock laser and its ULE reference cavity. This radio frequency is the sum of two oscillators [113] that independently provide a drift compensation for the ULE cavity using a DDS frequency generator and stepwise corrections to lock the laser to the clock transition via a conventional frequency synthesizer. The error signal of the phase lock acts on the VCO serving as local oscillator in the DDS generator. To scan the clock laser over or to lock it to the clock transition, the reference DDS of the phase lock is adjusted in addition to the conventional frequency synthesizer by the data acquisition system. The adjustment of the synthesizer frequency serves as feed forward to minimize the necessary adjustments of the drift compensating DDS. The bandwidth of the phase lock was chosen to 500 Hz to suppress higher frequency noise from a limited SNR in the transfer.

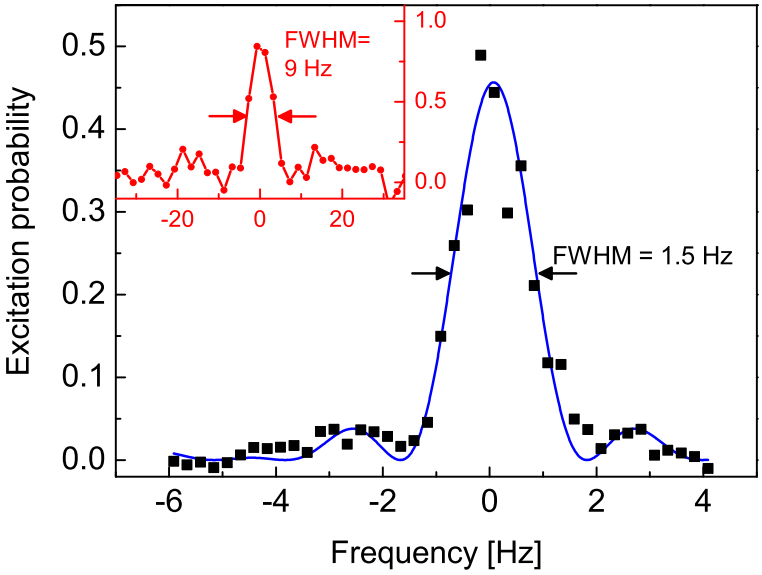

Figure 6.6: Spectra of one Zeeman component of the ^{87}Sr clock transition with the strontium clock laser only (inset, 10 Hz line width, data from Ref. [104]) and with the stability transfer from the master laser stabilized to the cryogenic silicon cavity. The figure is taken from [108].

6.3 Improving the ^{87}Sr optical lattice clock

The performance of the ^{87}Sr lattice clock at PTB has been recently evaluated [104], utilizing an ULE based reference resonator that supports instabilities of $\sigma_y(1\,\mathrm{s} - 10\,\mathrm{s}) \approx 2 \times 10^{-15}$ close to the expected thermal noise limit of $\sigma_y \approx 9 \times 10^{-16}$. With this laser, spectra of the $^1\mathrm{S}_0 - ^3\mathrm{P}_0$ clock transition with a Fourier limited linewidth of 10 Hz and 90 % contrast have been observed (inset in Fig. 6.6). Furthermore, the clock instability has been estimated interleaving two stabilizations on the two Zeeman components $m_\mathrm{F} = \pm 9/2$. The frequency difference averaged down with $5 \times 10^{-15}/\sqrt{\tau/\mathrm{s}}$, meaning that this instability is available to evaluate systematic shifts. If all interrogations are utilized for one stabilization, clock instabilities are expected to be a factor of two smaller, provided frequency shifts of transition are kept sufficiently stable in the long-term (see red curve in Fig. 6.7). With a cycle time $T_c = 630$ ms and a probe time $T_p = 90$ ms, this performance represents the Dick limit from the thermal noise of the local oscillator (see Fig. 6.3).

Activating the transfer lock of the strontium clock laser to the silicon cavity laser has led to significant improvements. Spectra of the transition with linewidth below 2 Hz were observed as shown in Fig. 6.6. Note that an excitation probability close to unity was not observed since the interrogation sequence did not include a clean up of atoms remaining in other than the interrogated Zeeman levels after imperfect spin polarization. For the interleave measurement, spin polarization was improved, and a maximum excitation probability of 80 % was observed with a probe time of 380 ms (corresponding to a Fourier-limited line width of 2.1 Hz). The observed instability was reduced by a factor of 5.5, meaning that the averaging time required

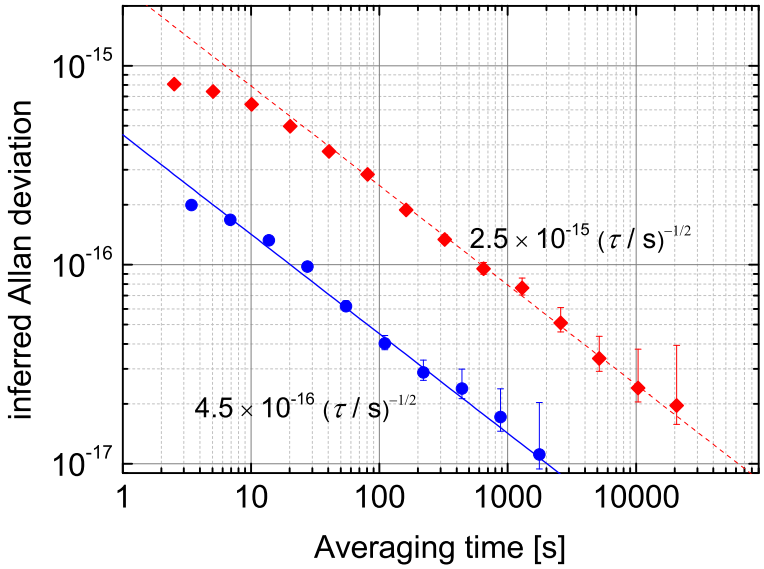

Figure 6.7: Stabilities of the Sr lattice clock inferred from interleaved measurements using the stability of the ULE reference cavity of the Sr clock laser (upper curve, data from Ref. [104]) and with the stability transfer from the silicon cavity stabilized laser system (lower curve). Averaging times to achieve a desired statistical uncertainty are reduced in the latter case by a factor of 30. The figure is taken from [108].

to determine systematic shifts is lowered by a factor of 30. This performance is similar to the best so far achieved values [15, 99]. Inferring a single-stabilization to average down with $4.5 \times 10^{-16}/\sqrt{\tau/\mathrm{s}}$, a statistical uncertainty of 1×10^{-17} is in reach within half an hour.

With the frequency noise spectrum from Fig. 5.8 one derives a Dick limit of $\sigma_y(\tau) = 2.5 \times 10^{-16}/\sqrt{\tau/\mathrm{s}}$ ($T_c = 860$ ms), slightly lower than the inferred clock instability. The origin of the slightly lower performance achieved will be further investigated in the future. Systematic frequency shifts of the atomic transition frequency can not be excluded. Moreover, as revealed in [108], acoustic and thermal influences on the fiber comb setup are expected to limit the performance of the transfer to $\sigma_y = 1 \ldots 3 \times 10^{-16}$ at one second. Thus, in the current setup a degradation of the transferred laser performance can not be ruled out. However, this is not a principle limitation, as further measures with respect to temperature stabilization and acoustic shielding of the fiber comb can be applied.

Chapter 7

Conclusion and Outlook

For more than one decade, Brownian noise in optical reference cavities has limited state-of-the-art ultra-stable lasers to fractional frequency instabilities above $\sigma_y = 2 \ldots 3 \times 10^{-16}$. In this work, an ultra-stable laser system has been developed which significantly reduced this fundamental limitation, demonstrating fractional frequency instabilities below $mod\,\sigma_y = 1 \times 10^{-16}$ between 0.1 s and 1 s. This improvement was enabled by the implementation of a cryogenic reference cavity design, which employs single-crystal silicon as material for spacer and the mirror substrates of the cavity. A low operating temperature of 124.2 K and the superior mechanical properties of silicon reduce the expected thermal noise floor to $\sigma_y = 4 \times 10^{-17}$, a factor of three lower compared to state-of-the-art glass resonators.

The investigations have verified that silicon is not only an adequate material to reduce the thermal noise of a reference cavity. At a temperature of 124.2 K, the thermal-expansion of the silicon cavity is zero, minimizing cavity-length fluctuations caused by temperature instabilities. Benefiting from the relatively high Young's modulus of silicon, the vibration insensitivity of the silicon cavity, despite a doubled length, competes with best values of equally mounted glass resonators [57, 114]. A drift of the minimal cavity length of only 9×10^{-21}/s was observed, demonstrating that a silicon cavity stabilized laser can also provide an excellent long-term stability competing with an active hydrogen maser, if the temperature instability of the silicon cavity is kept sufficiently low.

With the reduction of the thermal noise, formerly covered noise from "classical" sources has become challenging again. The investigations on the setup indicate the challenges that are yet to be mastered to reach the predicted thermal noise floor of $\sigma_y = 4 \times 10^{-17}$. Beginning with the most conspicuous, vacuum problems in the cryostat need to be fixed in order to reduce residual vacuum pressure to 10^{-10} mbar. Residual amplitude modulation was suppressed to a high degree and did most likely not degrade the laser stability below an averaging time of 10 s. In the future, the mirrors of the silicon cavity will be exchanged with a mirror pair that has been found to provide a finesse of 400 000 at TEM_{00}, further reducing the impact of residual amplitude modulation on the laser stability. The locking to TEM_{00} instead to TEM_{01}-mode furthermore prevents implications that might occur in combination with beam clipping. In addition, a higher cavity finesse decreases a line pulling ef-

fect which originates from a coupling of the high-finesse resonator with an extended low-finesse cavity.

Exploiting the dependency of the vertical vibration sensitivity on the mounting position the impact of vibrations on the short-term stability can be further reduced. A second, identical silicon cavity stabilized laser system is currently under development which will allow a better characterization of the first system, and thus, a more effective optimization of both systems.

At this early stage, it has already been demonstrated that silicon is a suitable material for constructing ultra-low thermal noise interferometers. This makes silicon a good choice for other high-precision interferometers that encounter thermal noise such as gravitational wave detectors. As described in Sec. 6.1.2, lowering the thermal noise of optical reference cavities opens a large room for improvements, particularly in optical lattice clocks. On the example of ^{87}Sr optical lattice clock at PTB, it has been demonstrated that the limitation of the operating frequency of the silicon laser to the infrared can be overcome, utilizing a femtosecond frequency comb as transfer oscillator. Although the additional elements increase the complexity and vulnerability of such a compound clock, utilizing the silicon laser led to a significant improvement of the clock performance. Clock instabilities are expected to average down with $\sigma_y(\tau) = 4.5 \times 10^{-16}/\sqrt{\tau/\mathrm{s}}$, competing with the best so far observed instabilities [15].

This performance facilitates the evaluation of systematic effects to push the accuracy of optical atomic clocks. Moreover, it enables applications of optical frequency standards on a new level of precision. For instance, it would be possible to resolve a gravitational red-shift in the earth potential of 10^{-17} – a difference of only 10 cm in altitude – within half an hour of averaging time!

Once thermal noise is the dominating noise process limiting the performance of the silicon cavity stabilized laser, there are various possibilities how to further reduce thermal noise.

First, one can adopt the same strategies that are pursued with conventional room-temperature cavities, scaling up the resonator length and the intra-cavity mode diameter. To give some numbers, realistic cavity parameters ($L = 0.3$ m, $R_1 = \infty$, $R_2 = 5$ m) would half the expected thermal noise floor to $\sigma_y = 2 \times 10^{-17}$. An equal improvement can be realized by operating the silicon cavity at its lower zero-crossing temperature at 20 K (see Fig. 3.2). Of course, an even further reduction of thermal noise can be accomplished operating the silicon cavity at ultra-cold temperatures. However, one will have to face the same implications that occur in cryogenic sapphire cavities with respect to vibrational noise from the employed cryostats.

Of much higher importance is the potential of the current silicon concept with prospect to future improvements in coating technology. As shown in Sec. 3.2, the contributions of the spacer and the substrates of the current silicon cavity to the total thermal noise are more than two orders of magnitude below that of the coatings. Thus, low-noise coatings would have direct impact on the thermal noise floor σ_y of the silicon cavity, scaling down with the square-root of the ratio of the loss-angles of the low-noise coatings and the currently employed Ta_2O_5/SiO_2-coatings. An improvement by a factor of 20 would already open up the avenue to fractional

frequency instabilities in the 10^{-18} regime! Though low-noise coatings would also reduce the efforts for constructing glass resonators that support 10^{-17} instabilities, the 10^{-18}-level is inaccessible for conventional resonators, as the thermal noise contribution of an ULE-spacer alone is above 10^{-17} for lengths up to one meter. Consequently, independently from new developments in coating technology, silicon seems to be the material of choice for the construction of high-end ultra-stable optical reference resonators.

Appendix A

Amplitude modulation from polarization modulation

Consider an electro-optical crystal made from $LiNbO_3$, whose extraordinary axis is perfectly parallel to an applied field E. The indices of refraction of the extraordinary axis n_e and ordinary axis n_o depend both on the crystal temperature T and on the strength of the electric field and are given by [115]

$$n_e(E,T) = n_e(T) - \frac{1}{2} n_e(T)^3 \mathfrak{r}_{33} E \ , \tag{A.1}$$

$$n_o(E,T) = n_o(T) - \frac{1}{2} n_o(T)^3 \mathfrak{r}_{13} E \ , \tag{A.2}$$

where $\mathfrak{r}_{33}, \mathfrak{r}_{13}$ are the electro-optic coefficients. Note that the direction of the principal axes does not depend on the applied field. If there is a misalignment α between the extraordinary axis and the linear polarization of the input light, the two field components E_e and E_o experience a differential phase shift $\Delta\gamma_{e,o}$ when passing the crystal with length L. It is given by

$$\Delta\gamma_{e,o}(T,E) = \gamma_e(T,E) - \gamma_o(T,E) \ , \tag{A.3}$$

$$\gamma_{e,o}(T,E) = \frac{2\pi L}{\lambda} n_{e,o}(T,E) \ , \tag{A.4}$$

and depends on both the temperature and the applied modulation field. The polarization state of the output light relies on the phase shift and is depicted in Fig. A.1. In general, it will be elliptical, which produces AM due to imbalances between carrier and sidebands, if the subsequent polarizer is not perfectly aligned to the extraordinary axis. With free-space modulators, alignment of input and output polarizer can be readily done, suppressing RAM to a high degree. Moreover, as shown in [90], further suppression can be achieved by applying a DC bias voltage in addition to the RF drive voltage. Due to the different electro-optic coefficients $\mathfrak{r}_{33}, \mathfrak{r}_{13}$, at any temperature an appropriate DC voltage can be applied to achieve $\Delta\gamma(T,E) = 0$.

In fiber-coupled waveguides, however, the input and output fibers are firmly mounted, leading to inevitable misalignments of typically a few degrees between the principal axes of the crystal and the polarization maintaining fibers. The large

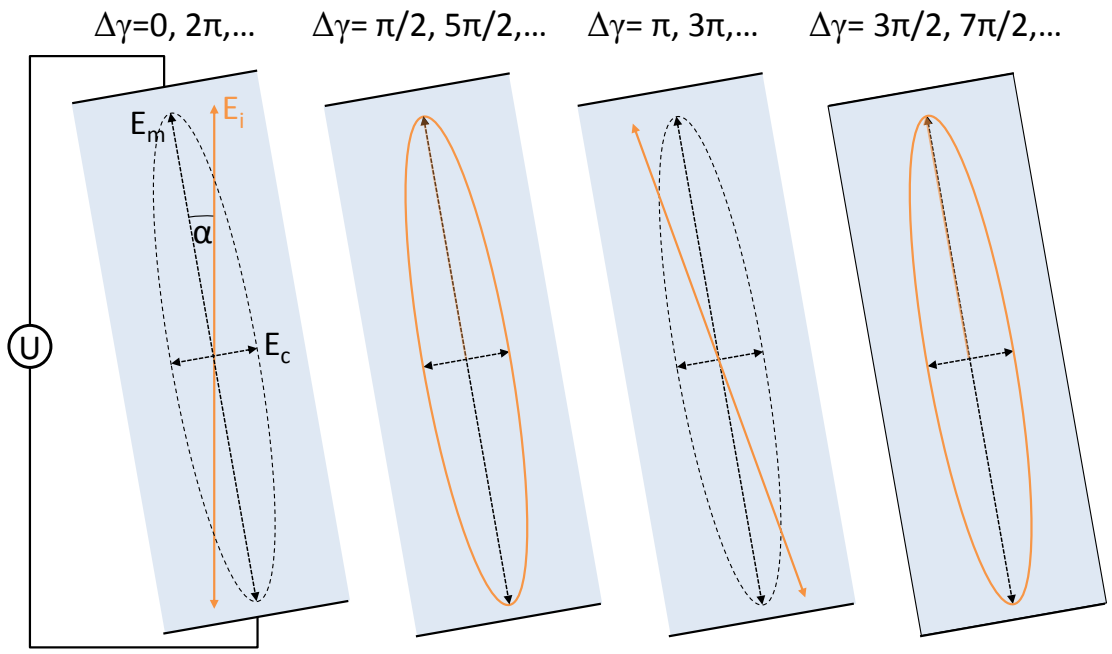

Figure A.1: Polarization states behind an $LiNbO_3$ crystal with misalignment angle α between linear input polarization and the crystal's extraordinary axis. If the phase shift $\Delta\gamma$ between both field components is a multiple of 2π, the output light will have the same linear polarization. In case $\Delta\gamma$ is an odd multiple of π, the output light will be linearly polarized but tilted by an angle $\sphericalangle(E_i, E_t) = 2\alpha$ with respect to the input polarization axis. In between, the polarization state is elliptical.

misalignment implicates a large polarization rotation effect, which produces prominent RAM behind a subsequent polarizer oriented in parallel to the input polarization.

The strength of this effect depends on the DC phase shift $\Delta\gamma_{e,o}$ and the modulation depth β. In dependence of the DC phase-shift, AM of even and odd harmonics of the modulation frequency rise up when increasing the modulation depth. Fig. A.2 illustrates and verifies this effect by measurement at different DC phase shifts: In case A, where the DC bias is set such that $\Delta\gamma = \pi/2$, the modulation signal leads to in-phase AM. Increasing the modulation amplitude (B), the first odd harmonic of Ω_m arises. If the DC bias is set such that the initial polarization is linearly polarized (C,D), the 1f-AM vanishes and there only remains a 2f-AM which does not affect the PDH locking. As the sign of the 1f-AM changes at $\Delta\gamma = \pm\pi/2$, the RAM servo loop will either lock to even or odd multiples of π. The voltage to achieve a phase shift of $\Delta\gamma = \pi$ between the two principal axes was only slightly larger than $V_\pi = 3$ V for phase modulation of the extraordinary beam.

The polarization modulation effect in principle allows to compensate in-phase RAM of any kind that occurs within the RAM detection path. The servo loop will produce a slight DC phase-shift to generate an appropriate amount of AM with opposite amplitude for compensation. Note, that there also exist proton-exchanged $LiNbO_3$ waveguides [116] that do not support light propagation in the ordinary

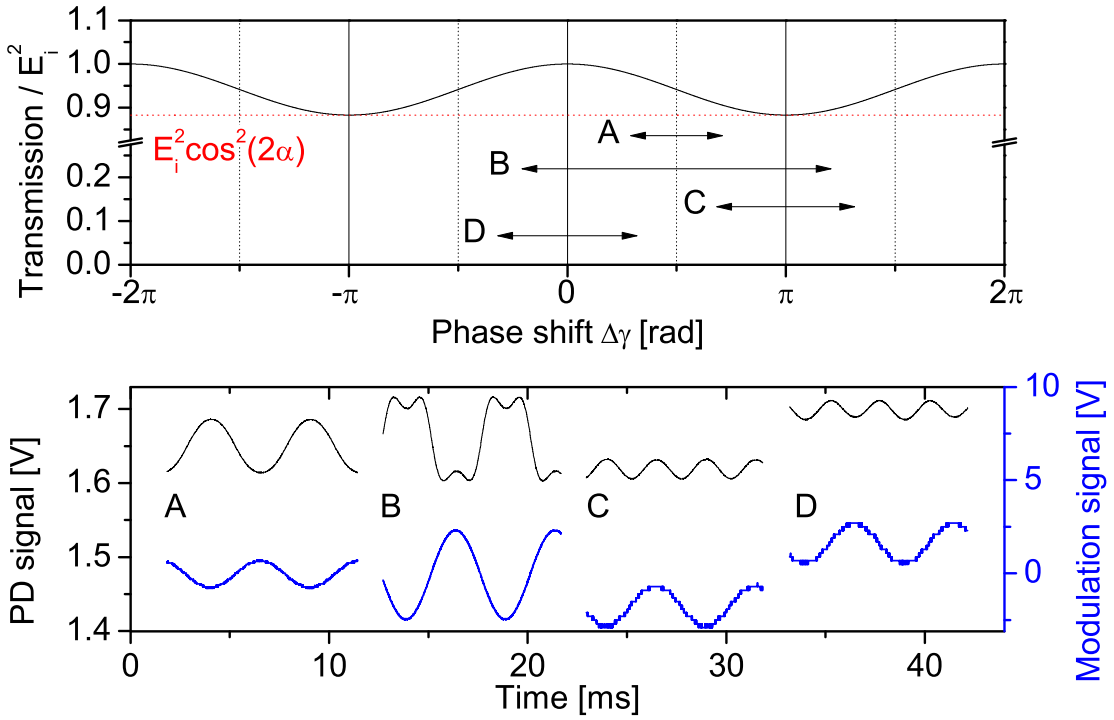

Figure A.2: **a,** Calculated transmitted power of the output polarizer, aligned parallel to the polarization axis of the input light. One expects an output power dependent on the birefringent phase shift $\Delta\gamma$ with maximum $|E_i|^2$ for $\Delta\gamma = n2\pi$ ($n = 0, 1, 2, \ldots$) and minimum $|E_i|^2 \cos^2(2\alpha)$ for $\Delta\gamma = (2n+1)\pi$. Between these two situations, the transmitted intensity varies sinusoidally (shown here for $\alpha = 10°$). **b,** Measured intensity modulation of the employed EOM in dependency of offset voltage and amplitude of the modulation signal.

axis. This suppresses the "out-of-the-box" RAM of these modulators, however, at the expense of losing the ability to cancel RAM from other sources such as residual etalons.

Appendix B

Dimensions of the silicon cavity spacer

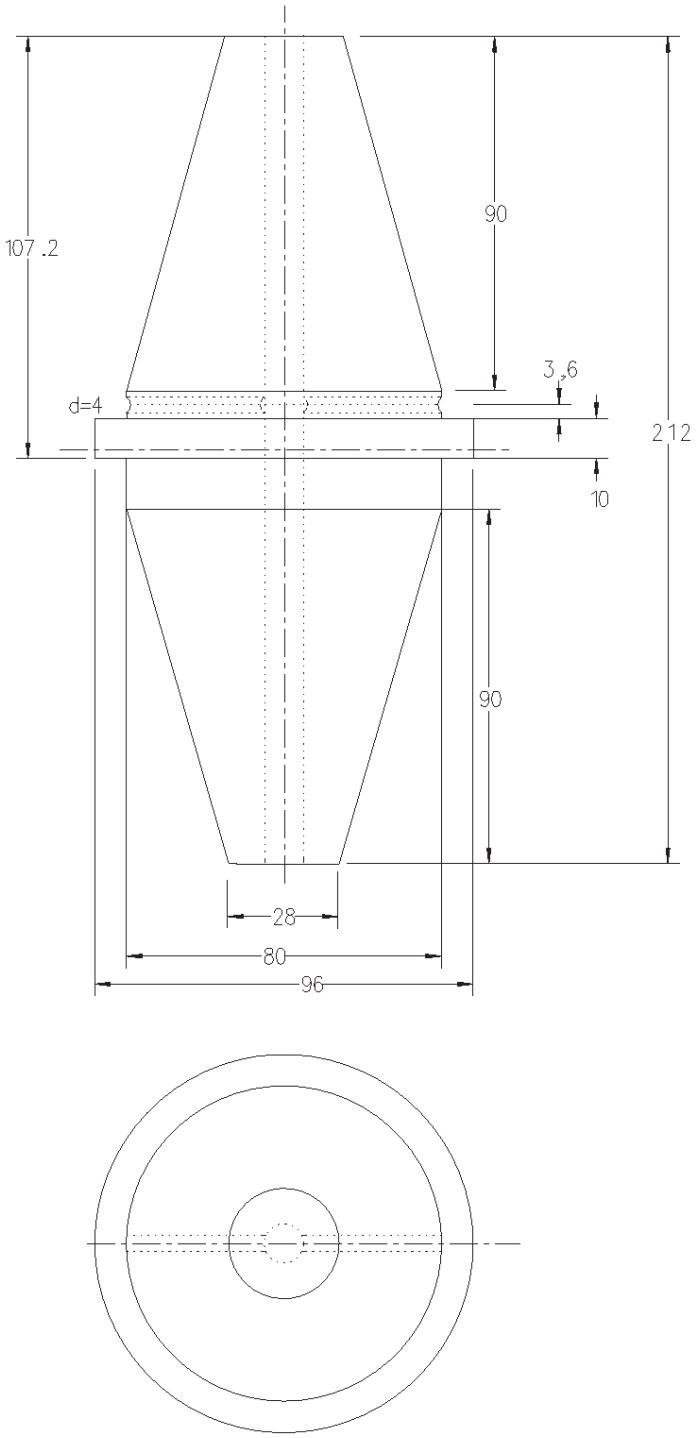

Figure B.1: Dimensions of the silicon cavity spacer given in Millimeters before polishing of its end-facets.

Appendix C

PDH servo amplifier

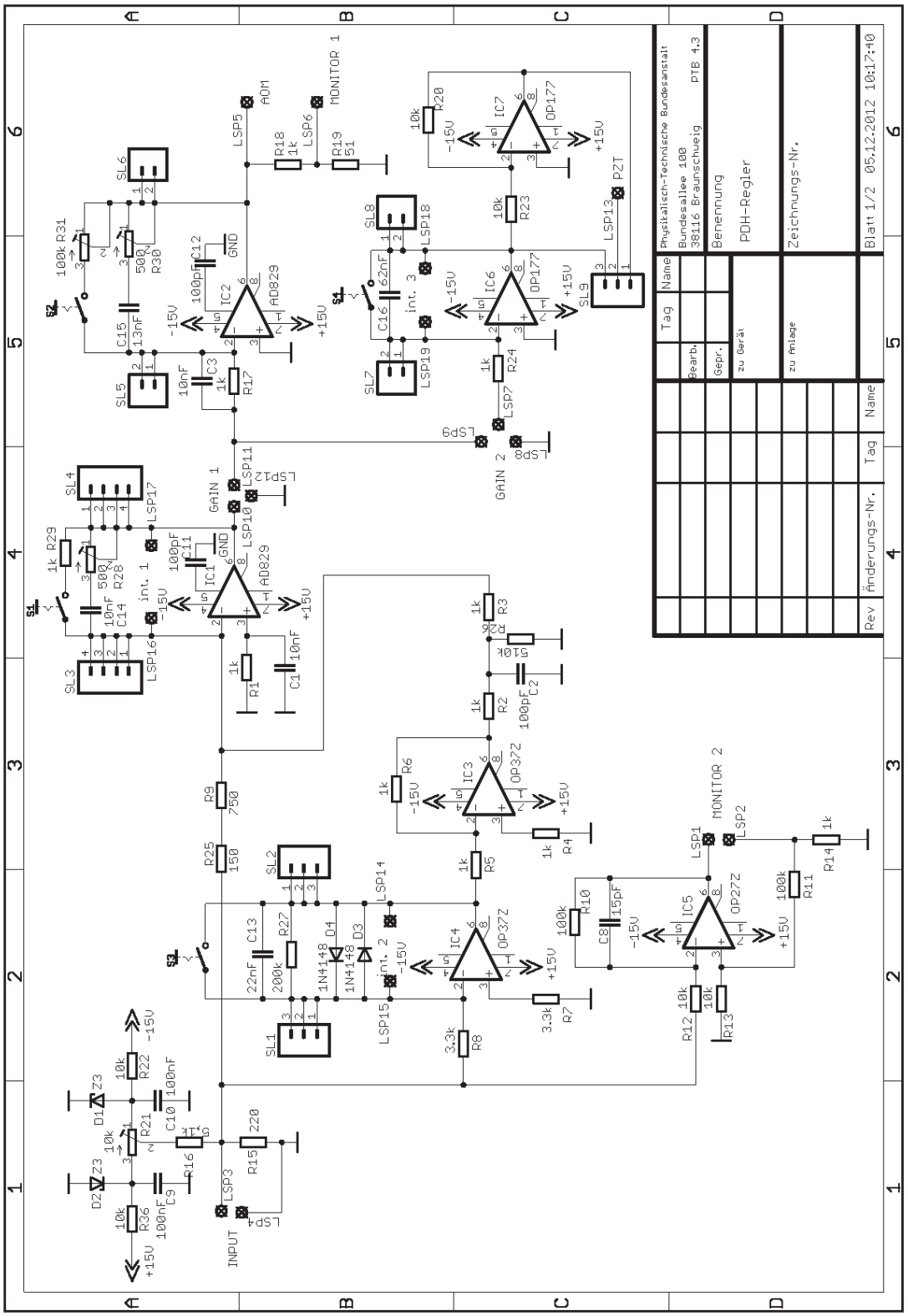

Figure C.1: Layout of PDH servo amplifier.

Bibliography

[1] A. A. Michelson and E. M. Morley, "On the relative motion of the earth and the luminiferous ether," *American Journal of Science - Third Series*, vol. XXXIV, no. 203, pp. 333–345, 1887.

[2] C. W. Chou, D. B. Hume, J. C. J. Koelemeij, D. J. Wineland, and T. Rosenband, "Frequency comparison of two high-accuracy Al^+ optical clocks," *Phys. Rev. Lett.*, vol. 104, p. 070802, 2010.

[3] A. D. Ludlow *et al.*, "Sr lattice clock at 1×10^{-16} fractional uncertainty by remote optical evaluation with a Ca clock," *Science*, vol. 319, pp. 1805–1808, 2008.

[4] N. Huntemann, M. Okhapkin, B. Lipphardt, S. Weyers, C. Tamm, and E. Peik, "High-accuracy optical clock based on the octupole transition in $^{171}Yb^+$," *Phys. Rev. Lett.*, vol. 108, p. 090801, Nov. 2011.

[5] B. Willke *et al.*, "Stabilized lasers for advanced gravitational wave detectors," *Classical and Quantum Gravity*, vol. 25, no. 11, p. 114040, 2008.

[6] B. P. Abbott *et al.*, "LIGO: the laser interferometer gravitational-wave observatory," *Rep. Prog. Phys.*, vol. 72, no. 7, p. 076901, 2009.

[7] W. Marshall, C. Simon, R. Penrose, and D. Bouwmeester, "Towards quantum superpositions of a mirror," *Phys. Rev. Lett.*, vol. 91, p. 130401, Sep 2003.

[8] B. Abbott *et al.*, "Observation of a kilogram-scale oscillator near its quantum ground state," *New J. Phys.*, vol. 11, no. 7, p. 073032, 2009.

[9] C. Eisele, A. Y. Nevsky, and S. Schiller, "Laboratory test of the isotropy of light propagation at the 10^{-17} level," *Phys. Rev. Lett.*, vol. 103, p. 090401, 2009.

[10] C. W. Chou, D. B. Hume, T. Rosenband, and D. J. Wineland, "Optical clocks and relativity," *Science*, vol. 329, pp. 1630 – 1633, 2010.

[11] T. Rosenband *et al.*, "Frequency ratio of Al^+ and Hg^+ single-ion optical clocks; metrology at the 17th decimal place," *Science*, vol. 319, pp. 1808–1812, 2008.

[12] B. C. Young, F. C. Cruz, W. M. Itano, and J. C. Bergquist, "Visible lasers with subhertz linewidths," *Phys. Rev. Lett.*, vol. 82, pp. 3799–3802, 1999.

[13] S. Vogt, C. Lisdat, T. Legero, U. Sterr, I. Ernsting, A. Nevsky, and S. Schiller, "Demonstration of a transportable 1 Hz-linewidth laser," *Appl. Phys. B*, vol. 104, pp. 741–745, Aug. 2011.

[14] D. R. Leibrandt, M. J. Thorpe, and T. R. James C. Bergquist, "Field-test of a robust, portable, frequency-stable laser," *Opt. Express*, vol. 19, pp. 10 278–10 286, April 2011.

[15] Y. Y. Jiang, A. D. Ludlow, N. D. Lemke, R. W. Fox, J. A. Sherman, L.-S. Ma, and C. W. Oates, "Making optical atomic clocks more stable with 10^{-16} level laser stabilization," *Nature Photonics*, vol. 5, pp. 158–161, 2011.

[16] Y. Levin, "Internal thermal noise in the LIGO test masses: A direct approach," *Phys. Rev. D*, vol. 57, pp. 659–663, 1998.

[17] F. Bondu, P. Hello, and J.-Y. Vinet, "Thermal noise in mirrors of interferometric gravitational wave antennas," *Phys. Lett. A*, vol. 246, pp. 227–236, 1998.

[18] G. M. Harry *et al.*, "Titania-doped tantala/silica coatings for gravitational-wave detection," *Class.Quantum Grav.*, vol. 24, pp. 405–415, 2007.

[19] A. E. Villar *et al.*, "Measurement of thermal noise in multilayer coatings with optimized layer thickness," *Phys. Rev. D*, vol. 81, p. 122001, 2010.

[20] W. Peng, M. M. Roberts, E. P. Nordberg, F. S. Flack, P. E. Colavita, R. J. Hamers, D. E. Savage, M. G. Lagally, and M. A. Eriksson, "Single-crystal silicon/silicon dioxide multilayer heterostructures based on nanomembrane transfer," *Applied Physics Letters*, vol. 90, no. 18, p. 183107, 2007.

[21] G. D. Cole, S. Gröblacher, K. Gugler, S. Gigan, and M. Aspelmeyer, "Monocrystalline $Al_xGa_{1-x}As$ heterostructures for high-reflectivity high-Q micromechanical resonators in the megahertz regime," *Appl. Phys. Lett.*, vol. 92, no. 26, p. 261108, 2008.

[22] F. Brückner, T. Clausnitzer, O. Burmeister, D. Friedrich, E.-B. Kley, K. Danzmann, A. Tünnermann, and R. Schnabel, "Monolithic dielectric surfaces as new low-loss light-matter interfaces," *Opt. Lett.*, vol. 33, pp. 264–266, 2008.

[23] G. M. Harry *et al.*, "Thermal noise in interferometric gravitational wave detectors due to dielectric optical coatings," *Class. Quantum Grav.*, vol. 19, pp. 897–917, 2002.

[24] H. Müller, S. Herrmann, C. Braxmaier, S. Schiller, and A. Peters, "Modern Michelson-Morley experiment using cryogenic optical resonators," *Phys. Rev. Lett.*, vol. 91, p. 020401, 2003.

[25] S. Seel, R. Storz, G. Ruoso, J. Mlynek, and S. Schiller, "Cryogenic optical resonators: A new tool for laser frequency stabilization at the 1 Hz level," *Phys. Rev. Lett.*, vol. 78, pp. 4741–4744, 1997.

[26] R. Storz, C. Braxmaier, K. Jäck, O. Pradl, and S. Schiller, "Ultrahigh long-term dimensional stability of a sapphire cryogenic optical resonator," *Opt. Lett.*, vol. 23, pp. 1031–1033, 1998.

[27] J.-P. Richard and J. J. Hamilton, "Cryogenic monocrystalline silicon Fabry-Perot cavity for the stabilization of laser frequency," *Rev. Sci. Instrum.*, vol. 62, pp. 2375–2378, 1991.

[28] C. Swenson, "Recommended values for the thermal expansitivity of silicon from 0 to 1000 K," *J. Phys. Chem. Ref. Data*, vol. 12, pp. 179–182, 1983.

[29] H. Kogelnik and T. Li, "Laser beams and resonators," *Appl. Opt.*, vol. 5, pp. 1550–1567, 1966.

[30] N. Hodgson and H. Weber, *Optical Resonators: Fundamentals, Advanced Concepts, Applications*. Springer, 1997.

[31] E. D. Black, "An introduction to Pound-Drever-Hall laser frequency stabilization," *Am. J. Phys.*, vol. 69, pp. 79–87, 2001.

[32] E. Hecht, *Optics*, 4th ed. Reading MA, Amsterdam, London: Addison-Wesley, 2002.

[33] F. Riehle, *Frequency Standards: Basics and Applications*. Weinheim: Wiley-VCH, 2004.

[34] T. W. Hänsch and B. Couillaud, "Laser frequency stabilization by polarization spectroscopy of a reflecting reference cavity," *Opt. Commun.*, vol. 35, pp. 441–444, 1980.

[35] R. W. P. Drever, J. L. Hall, F. V. Kowalski, J. Hough, G. M. Ford, A. J. Munley, and H. Ward, "Laser phase and frequency stabilization using an optical resonator," *Appl. Phys. B*, vol. 31, pp. 97–105, 1983.

[36] W. J. Riley, *Handbook of frequency stability analysis*. NIST Special Publication, 2008, vol. 1065.

[37] D. W. Allan and J. Barnes, "A modified "Allan variance" with increased oscillator characterization ability," in *Proceedings of the 35th Ann. Freq. Control Symposium*. Ft. Monmouth, NJ 07703: Electronic Industries Association, May 1981, pp. 470–475.

[38] S. T. Dawkins, J. J. McFerran, and A. N. Luiten, "Considerations on the measurement of the stability of oscillators with frequency counters," *IEEE Trans. Ultrason. Ferroelectr. Freq. Control*, vol. 54, pp. 918–925, 2007.

[39] J. Rutman, "Characterization of phase and frequency instabilities in precision frequency sources: fifteen years of progress," *Proc. IEEE*, vol. 66, pp. 1048–1075, 1978.

[40] J. Rutman and F. Walls, "Characterization of frequency stability in precision frequency sources," *Proceedings of the IEEE*, vol. 79, no. 7, pp. 952 –960, Jul 1991.

[41] J. E. Gray and D. W. Allan, "A method for estimating the frequency stability of an individual oscillator," in *Proc. 28th Frequency Control Symp.*, 1974.

[42] A. Premoli and P. Tavella, "A revisited three-cornered hat method for estimating frequency standard instability," *IEEE Trans. Instrum. Meas.*, vol. 42, pp. 7–13, 1993.

[43] P. Tavella and A. Premoli, "Estimating the instabilities of N clocks by measuring differences of their readings," *Metrologia*, vol. 30, pp. 479–486, 1994.

[44] F. Torcaso, C. Ekstrom, E. Burt, and D. Matsakis, "Estimating the stability of N clocks with correlations," *IEEE Trans. Ultrason. Ferroelectr. Freq. Control*, vol. 47, pp. 1183–1189, 2000.

[45] K. Numata, A. Kemery, and J. Camp, "Thermal-noise limit in the frequency stabilization of lasers with rigid cavities," *Phys. Rev. Lett.*, vol. 93, pp. 250 602–1–4, 2004.

[46] V. B. Braginsky, M. L. Gorodetsky, and S. P. Vyatchanin, "Thermodynamical fluctuations and photo-thermal shot noise in gravitational wave antennae," *Physics Letters A*, vol. 264, pp. 1–10, 1999.

[47] Y. T. Liu and K. S. Thorne, "Thermoelastic noise and homogeneous thermal noise in finite sized gravitational-wave test masses," *Phys. Rev. D*, vol. 62, p. 122002, 2000.

[48] N. Nakagawa, A. M. Gretarsson, E. K. Gustafson, and M. M. Fejer, "Thermal noise in half-infinite mirrors with nonuniform loss: A slab of excess loss in a half-infinite mirror," *Phys. Rev. D*, vol. 65, p. 102001, 2002.

[49] V. B. Braginsky and S. P. Vyatchanin, "Thermodynamical fluctuations in optical mirror coatings," *Phys. Lett. A*, vol. 312, pp. 244–255, 2003.

[50] M. M. Fejer, S. Rowan, G. Cagnoli, D. R. M. Crooks, A. Gretarsson, G. M. Harry, J. Hough, S. D. Penn, P. H. Sneddon, and S. P. Vyatchanin, "Thermoelastic dissipation in inhomogeneous media: loss measurements and displacement noise in coated test masses for interferometric gravitational wave detectors," *Phys. Rev. D*, vol. 70, pp. 082 003–1–19, 2004.

[51] M. Evans, S. Ballmer, M. Fejer, P. Fritschel, G. Harry, and G. Ogin, "Thermo-optic noise in coated mirrors for high-precision optical measurements," *Phys. Rev. D*, vol. 78, pp. 102 003–1–10, 2008.

[52] B. L. Lev, A. Vukics, E. R. Hudson, B. C. Sawyer, P. Domokos, H. Ritsch, and J. Ye, "Prospects for the cavity-assisted laser cooling of molecules," *Phys. Rev. A*, vol. 77, no. 2, pp. 023 402–1–13, 2008.

[53] M. L. Gorodetsky, "Thermal noises and noise compensation in high-reflection multilayer coating," *Physics Letters A*, vol. 372, no. 46, pp. 6813 – 6822, 2008.

[54] H. B. Callen and T. A. Welton, "Irreversibility and generalized noise," *Phys. Rev.*, vol. 83, no. 1, pp. 34–40, 1951.

[55] G. M. Harry *et al.*, "Thermal noise from optical coatings in gravitational wave detectors," *Appl. Opt.*, vol. 45, pp. 1569–1574, 2006.

[56] T. Kessler, T. Legero, and U. Sterr, "Thermal noise in optical cavities revisited," *J. Opt. Soc. Am. B*, vol. 29, pp. 178–184, 2012.

[57] J. Millo, D. V. Magalhães, C. Mandache, Y. Le Coq, E. M. L. English, P. G. Westergaard, J. Lodewyck, S. Bize, P. Lemonde, and G. Santarelli, "Ultrastable lasers based on vibration insensitive cavities," *Phys. Rev. A*, vol. 79, p. 053829, 2009.

[58] T. Legero, T. Kessler, and U. Sterr, "Tuning the thermal expansion properties of optical reference cavities with fused silica mirrors," *J. Opt. Soc. Am. B*, vol. 27, pp. 914–919, 2010.

[59] S. D. Penn, G. M. Harry, A. M. Gretarsson, S. E. Kittelberger, P. R. S. J. J. Schiller, J. R. Smith, and S. O. Swords, "High quality factor measured in fused silica," *Classical and Quantum Gravity*, vol. 72, no. 9, p. 3670, 2001.

[60] R. Schnabel *et al.*, "Building blocks for future detectors: Silicon test masses and 1550 nm laser light," *Journal of Physics: Conference Series*, vol. 228, p. 012029, 2010.

[61] F. Brückner, D. Friedrich, T. Clausnitzer, M. Britzger, O. Burmeister, K. Danzmann, E.-B. Kley, A. Tünnermann, and R. Schnabel, "Realization of a monolithic high-reflectivity cavity mirror from a single silicon crystal," *Phys. Rev. Lett.*, vol. 104, p. 163903, 2010.

[62] R. D. Gregory Harry, Timothy P. Bodiya, Ed., *Optical Coatings and Thermal Noise in Precision Measurement*. Cambridge University Press, 2012.

[63] R. Nawrodt *et al.*, "High mechanical q-factor measurements on silicon bulk samples," *Journal of Physics: Conference Series*, vol. 122, p. 012008, 2008.

[64] T. Uchiyama *et al.*, "Mechanical quality factor of a cryogenic sapphire test mass for gravitational wave detectors," *Phys. Rev. A*, vol. 261, pp. 5–11, 1999.

[65] R. Nawrodt, A. Zimmer, T. Koettig, S. Nietzsche, M. Thürk, W. Vodel, and P. Seidel, "High mechanical Q-factor measurements on calcium fluoride at cryogenic temperatures," *Eur. Phys. J. Appl. Phys.*, vol. 38, pp. 53–59, 2007.

[66] K. Yamamoto *et al.*, "Measurement of the mechanical loss of a cooled reflective coating for gravitational wave detection," *Phys. Rev. D*, vol. 74, p. 022002, 2006.

[67] I. W. Martin, "Studies of materials for use in future interferometric gravitational wave detectors," Ph.D. dissertation, University of Glasgow, 2009.

[68] I. Martin *et al.*, "Effect of heat treatment on mechanical dissipation in Ta_2O_5 coatings," *Class. Quantum Grav.*, vol. 27, p. 225020, 2010.

[69] W. A. Brantley, "Calculated elastic constants for stress problems associated with semiconductor devices," *J. Appl. Phys.*, vol. 44, pp. 534–535, 1973.

[70] H. Stoehr, "Diodenlaser mit Hertz-Linienbreite für ein optisches Calcium-Frequenznormal," Ph.D. dissertation, Universität Hannover, Universität Hannover, 2004.

[71] C. J. Glassbrenner and G. A. Slack, "Thermal conductivity of silicon and germanium from 3°K to the melting point," *Phys. Rev.*, vol. 134, pp. A1058–A1069, 1964.

[72] H. R. Telle, B. Lipphardt, and J. Stenger, "Kerr-lens mode-locked lasers as transfer oscillators for optical frequency measurements," *Appl. Phys. B*, vol. 74, pp. 1–6, 2002.

[73] *Transmission of an Optical Carrier Frequency over a Telecommunication Fiber Link*. Optical Society of America, 2007.

[74] M. Notcutt, L.-S. Ma, J. Ye, and J. L. Hall, "Simple and compact 1-Hz laser system via an improved mounting configuration of a reference cavity," *Opt. Lett.*, vol. 30, pp. 1815–1817, 2005.

[75] A. D. Ludlow, X. Huang, M. Notcutt, T. Zanon-Willette, S. M. Foreman, M. M. Boyd, S. Blatt, and J. Ye, "Compact, thermal-noise-limited optical cavity for diode laser stabilization at 1×10^{-15}," *Opt. Lett.*, vol. 32, pp. 641–643, 2007.

[76] T. Nazarova, F. Riehle, and U. Sterr, "Vibration-insensitive reference cavity for an ultra-narrow-linewidth laser," *Appl. Phys. B*, vol. 83, pp. 531–536, 2006.

[77] S. A. Webster, M. Oxborrow, and P. Gill, "Vibration insensitive optical cavity," *Phys. Rev. A*, vol. 75, pp. 011 801(R)–1–4, 2007.

[78] S. Webster and P. Gill, "Force-insensitive optical cavity," *Opt. Lett.*, vol. 36, pp. 3572–3574, 2011.

[79] G. Hartwig, *Polymer Properties at Room and Cryogenic Temperatures*. Plenum Press, 1994.

[80] C. S. G. Cousins, "Inner elasticity," *Journal of Physics C: Solid State Physics*, vol. 11, no. 24, p. 4867, 1978.

[81] C. S. G. Cousins, "Internal strain in diamond structure elements: a survey of theoretical approaches," *Journal of Physics C: Solid State Physics*, vol. 15, no. 9, p. 1857, 1982.

[82] J. W. Ekin, *Experimental Techniques for Low-Temperature Measurements*, 1st ed. New York, Oxford: Oxford University Press, 2006.

[83] Y. S. Touloukian and E. H. Buyco, *Thermal conductivity*. New York: Plenum Press, 1970, vol. 1,2.

[84] W. M. Toscano and E. G. Cravalho, "Thermal radiative properties of the noble metals at cryogenic temperatures," *Journal of Heat Transfer*, vol. 98, no. 3, pp. 438–445, 1976.

[85] J. L. Schiff, *The Laplace Transform: Theory and Applications*. Springer, 1999.

[86] H. Lutz and W. Wendt, *Taschenbuch der Regelungstechnik*. Harry Deutsch, 2005.

[87] L.-S. Ma, P. Jungner, J. Ye, and J. L. Hall, "Delivering the same optical frequency at two places: accurate cancellation of phase noise introduced by optical fiber or other time-varying path," *Opt. Lett.*, vol. 19, pp. 1777–1779, 1994.

[88] K. P. Birch and M. J. Downs, "Correction to the updated edlén equation for the refractive index of air," *Metrologia*, vol. 31, no. 4, p. 315, 1994.

[89] E. A. Whittaker, M. Gehrtz, and G. C. Bjorklund, "Residual amplitude modulation in laser-optic phase modulation," *J. Opt. Soc. Am. B*, vol. 2, pp. 1320 – 1326, 1985.

[90] N. C. Wong and J. L. Hall, "Servo control of amplitude modulation in frequency-modulation spectroscopy: demonstration of shot-noise-limited detection," *J. Opt. Soc. Am. B*, vol. 2, pp. 1527–1533, 1985.

[91] I. Silander, P. Ehlers, J. Wang, and O. Axner, "Frequency modulation background signals from fiber-based electro optic modulators are caused by crosstalk," *J. Opt. Soc. Am. B*, vol. 29, no. 5, pp. 916–923, May 2012.

[92] E. Peik, T. Schneider, and C. Tamm, "Laser frequency stabilization to a single ion," *J. Phys. B: At. Mol. Phys.*, vol. 39, pp. 145–158, 2006.

[93] R. Wynands and S. Weyers, "Atomic fountain clocks," *Metrologia*, vol. 42, pp. S64–S79, 2005.

[94] T. Legero, "Resonatorstabilisierter Faserlaser als optischer Lokaloszillator für optische Uhren und die optische Nachrichtentechnik," TIB Hannover, Schlussbericht MNPQ-Projekt Nr. 06/07, 2011.

[95] E. Rubiola, "On the measurement of frequency and of its sample variance with high-resolution counters," *Rev. Sci. Instrum.*, vol. 76, p. 054703, 2005.

[96] H. R. Telle, G. Steinmeyer, A. E. Dunlop, J. Stenger, D. H. Sutter, and U. Keller, "Carrier-envelope offset phase control: A novel concept for absolute optical frequency measurement and ultrashort pulse generation," *Appl. Phys. B*, vol. 69, pp. 327–332, 1999.

[97] G. Santarelli, C. Audoin, A. Makdissi, P. Laurent, G. J. Dick, and A. Clairon, "Frequency stability degradation of an oscillator slaved to a periodically interrogated atomic resonator," *IEEE Trans. Ultrason., Ferroelect., Freq. Contr.*, vol. 45, pp. 887–894, 1998.

[98] A. Quessada, R. P. Kovacich, I. Courtillot, A. Clairon, G. Santarelli, and P. Lemonde, "The Dick effect for an optical frequency standard," *J. Opt. B: Quantum Semiclass. Opt.*, vol. 5, pp. S150–S154, 2003.

[99] M. Takamoto, T. Takano, and H. Katori, "Frequency comparison of optical lattice clocks beyond the Dick limit," *Nature Photonics*, vol. 5, pp. 288–292, 2011.

[100] W. M. Itano, J. C. Bergquist, J. J. Bollinger, J. M. Gilligan, D. J. Heinzen, F. L. Moore, M. G. Raizen, and D. J. Wineland, "Quantum projection noise: Population fluctuations in two-level systems," *Phys. Rev. A*, vol. 47, pp. 3554–3570, 1993.

[101] A. E. E. Rogers and J. M. Moran, Jr., "Coherence limit for very long baseline interferometry," *IEEE Trans. Instrum. Meas.*, vol. 30, pp. 283–286, 1981.

[102] G. J. Dick, J. Prestage, C. Greenhall, and L. Maleki, "Local oscillator induced degradation of medium-term stability in passive atomic frequency standards," in *Proceedings of the 22nd Annual Precise Time and Time Interval (PTTI) Applications and Planning Meeting, Vienna VA, USA*, 1990, pp. 487–509.

[103] P. Westergaard, J. Lodewyck, and Lemonde, "Minimizing the Dick effect in an optical lattice clock," *IEEE Trans. Ultrason. Ferroelectr. Freq. Control*, vol. 57, no. 3, pp. 623–628, 2010.

[104] S. Falke *et al.*, "The ^{87}Sr optical frequency standard at PTB," *Metrologia*, vol. 48, pp. 399–407, 2011.

[105] G. Grosche, B. Lipphardt, and H. Schnatz, "Optical frequency synthesis and measurement using fibre-based femtosecond lasers," *Eur. Phys. J. D*, vol. 48, pp. 27–33, 2008.

[106] T. Legero, C. Lisdat, J. S. R. Vellore Winfred, H. Schnatz, G. Grosche, F. Riehle, and U. Sterr, "Interrogation laser for a strontium lattice clock," *IEEE Trans. Instrum. Meas.*, vol. 58, pp. 1252–1257, 2009.

[107] A. Yamaguchi, N. Shiga, S. Nagano, Y. Li, H. Ishijima, H. Hachisu, M. Kumagai, and T. Ido, "Stability transfer between two clock lasers operating at different wavelengths for absolute frequency measurement of clock transition in ^{87}Sr," *Appl. Phys. Express*, vol. 5, p. 022701, 2012.

[108] C. Hagemann, C. Grebing, T. Kessler, S. Falke, N. Lemke, C. Lisdat, H. Schnatz, F. Riehle, and U. Sterr, "Providing 10^{-16} short-term stability of a 1.5-μm laser to optical clocks," *IEEE Trans. Instrum. Meas.*, DOI: 10.1109/TIM.2013.2242597, 2013.

[109] C. Lisdat, J. S. R. Vellore Winfred, T. Middelmann, F. Riehle, and U. Sterr, "Collisional losses, decoherence, and frequency shifts in optical lattice clocks with bosons," *Phys. Rev. Lett.*, vol. 103, p. 090801, 2009.

[110] T. Middelmann, C. Lisdat, S. Falke, J. S. R. Vellore Winfred, F. Riehle, and U. Sterr, "Tackling the blackbody shift in a strontium optical lattice clock," *IEEE Trans. Instrum. Meas.*, vol. 60, pp. 2550–2557, 2011.

[111] S. T. Cundiff and J. Ye, "Colloqium: Femtosecond optical frequency combs," *Rev. Mod. Phys.*, vol. 75, pp. 325–342, 2003.

[112] Y. Nakajima *et al.*, "A multi-branch, fiber-based frequency comb with millihertz-level relative linewidths using an intra-cavity electro-optic modulator," *Opt. Express*, vol. 18, no. 2, pp. 1667–1676, Jan 2010.

[113] S. Falke, M. Misera, U. Sterr, and C. Lisdat, "Delivering pulsed and phase stable light to atoms of an optical clock," *Appl. Phys. B*, vol. 107, pp. 301–311, 2012.

[114] B. Argence, E. Prevost, T. Lévèque, R. L. Goff, S. Bize, P. Lemonde, and G. Santarelli, "Prototype of an ultra-stable optical cavity for space applications," *Opt. Express*, vol. 20, no. 23, pp. 25 409–25 420, 2012.

[115] B. E. A. Saleh and M. C. Teich, Eds., *Fundamentals of Photonics*. Wiley-VCH, 2001.

[116] J. L. Jackel, C. E. Rice, and J. J. Veselka, "Proton exchange for high-index waveguides in linbo[sub 3]," *Applied Physics Letters*, vol. 41, no. 7, pp. 607–608, 1982.

Acknowledgements

Before I switch to my mother tongue, I want to say "thank you" to Jun Ye and his group from the JILA/NIST in Boulder, Colorado, for the fruitful collaboration in the silicon cavity project. I appreciate the effort Michael Martin has made, spending more than a month at PTB in several stays to set up the ultra-stable reference laser system for the frequency comparison. I had a great time with him in the lab and benefited from his large experience and cleverness.

Viele weitere hilfsbereite Personen haben zum Gelingen dieser Arbeit beigetragen, denen ich hiermit meinen Dank aussprechen möchte:

- Allen voran möchte ich Herrn Dr. Thomas Kessler als meinen Gruppenleiter und Betreuer für die tolle Zeit danken, die mir sicher immer in Erinnerung bleiben wird. Gemeinsam haben wir einige Höhen und mehrere Tiefen durchschritten, bis sich dann der große Erfolg einstellte.
- Der von Herrn Dr. Thomas Legero entwickelte ultra-stabile Laser war unentbehrlich für die Charakterisierung des Siliziumresonators. Dafür und für seine stete Unterstützung und Mitarbeit möchte ich ihm danken.
- Herrn Dr. Uwe Sterr sei für seine unermüdliche Hilfsbereitschaft gedankt. Egal wie beschäftigt er grade war, er war immer empfänglich für „dringende " Fragen gewesen und hat mich von so manchem Irrweg weggeführt.
- Herrn Prof. Dr. Fritz Riehle möchte ich für seine Unterstüzung während der gesamten Jahre danken, vor allem für seinen engagierten Einsatz für das Siliziumprojekt.
- Herrn Prof. Dr. Piet Schmidt danke ich für die Übernahme des Referats dieser Arbeit, als auch für sein stetes Interesse, welches er bezüglich dieser Arbeit gezeigt hat.
- Herrn Prof. Dr. Ernst Rasel möchte ich für die Übernahme des Koreferats trotz der aufgetretenen „Terminengpässe" danken.
- Herrn Dr. Harald Schnatz sei mein Dank ausgesprochen für seine zielorientierten Hilfestellungen, die er geleistet hat. Unvergessen bleibt für mich zudem das Glas Wasser und das Kuchenstück, mit denen er mich auf der EFTF 2012 in Göteborg nach „der" Postersession versorgt hat.
- Großer Dank geht an Herrn Dr. Ulrich Kuetgens und Herrn Dieter Schulze, die essentielle Vorarbeiten am Siliziumkristall durchgeführt haben, aus dem später der Siliziumresonator gefertigt wurde.

- Dr. Christian Grebing sei herzlich für sein Engagement bei der Datenauswertung und der weiteren „Three-cornered hat“-analyse gedankt, als auch für die permanente „Pflege“ des Frequenzkammes für die erfolgten Langzeitmessungen gegen Maser und Fontänenuhr.
- Bei den Herren Dr. Christian Lisdat, Dr. Stephan Falke und Dr. Nathan Lemke von der Strontiumgitteruhr möchte ich mich für die tollen Ergebnisse bedanken, die sie mit Hilfe des in dieser Arbeit entwickelten Lasersystems erzielt haben. Allen dreien sei auch für ihre allgemeine Hilfsbereitschaft in so mancher Notsituation gedankt.
- Frau Dr. Gesine Grosche möchte ich für ihre Hilfestellung in vielerlei Angelegenheiten danken, allen voran bezüglich den Aufbau der Faserstabilisierung.
- Herrn Dr. Sebastian Raupach spreche ich für die vielen Leihgaben meinen Dank aus, die so manche spontane Messung ermöglichten.
- Meinen „Mitstreitern“, den Herren Thomas Middelmann, Sebastian Häfner, Stefan Vogt, Max Kahmann und Oliver Appel sei gedankt für die tolle gemeinsame Zeit und Zusammenarbeit.
- Ohne den „elektronischen Support“ durch Herrn Andreas Koczwara, Herrn Mattias Misera und Frau Marion Wengel wäre kein Licht angegangen. Ein besonderer Dank geht an sie.
- Bei den Herren Andre Uhde und Jörn Falke möchte ich mich für die mechanischen Arbeiten und vor allem für die hohe Einsatzbereitschaft bedanken.
- Herrn Dipl.-Ing. Burghard Lipphardt sei für die vielen interessanten Gespräche gedankt, bei denen ich viele hinzugelernt habe.
- Großer Dank geht auch an Herrn Dr. Stefan Weyers für die Versorgung mit Frequenzdaten bezüglich des Wasserstoffmasers.
- Frau Birgit Voss möchte ich für die Übernahme vieler verwaltungstechnischer Angelegenheiten danken.
- Bei Herrn Klemens Budin möchte ich mich für Rat und Tat bedanken, wenn es darum ging größere „Baumaßnahmen“ durchzuführen.
- Zu guter Letzt möchte ich mich bei meiner lieben Familie bedanken für die erfolgte Unterstützung während der vergangenen Jahre. Vor allem aber meiner lieben Frau Corinna bin ich zu tiefstem Dank verpflichtet, die viel Geduld und Verständnis aufgebracht hat und sich bisher alleinig um die Erziehung unserer Tochter kümmern musste. Ich freue mich auf die kommende Zeit mit den beiden.

Curriculum vitae

Christian Hagemann

Contact information
Email: christianhhagemann@gmail.com

Personal information
Gender: Male
Date of birth: 23th of June, 1983
Place of birth: Mölln, Germany
Nationality: German

Education

11/2009 - 02/2013	Doctoral studies in Physics at the Physikalisch-Technische Bundesanstalt (PTB), Braunschweig, research group "Ultra-stable lasers and high performance cavities" (established within the Centre for Quantum Engineering and Space-Time Research (QUEST))
11/2008 - 11/2009	Diploma thesis at Fraunhofer Institute for Applied Optics and Precision Engineering (IOF), Jena. "*Theoretische und experimentelle Untersuchungen an Pumpkopplern für Hochleistungsfaserlaser*"
04/2004 - 11/2009	Diploma studies in Physics, Universität Hamburg
06/2003	Abitur at the Lauenburgische Gelehrtenschule, Ratzeburg

Civil service

08/2003 - 05/2004	Retirement home St. Petri, Ratzeburg

Publications

C. Hagemann, C. Grebing, T. Kessler, S. Falke, N. Lemke, C. Lisdat, H. Schnatz, F. Riehle, and U. Sterr, "Providing 10^{-16} short-term stability of a 1.5-μm laser to optical clocks," *IEEE Trans. Instrum. Meas.*, DOI: 10.1109/TIM.2013.2242597, 2013.

S. Raupach, T. Legero, C. Grebing, Ch. Hagemann, T. Kessler, A. Koczwara, B. Lipphardt, M. Misera, H. Schnatz, G. Grosche, and U. Sterr, "Subhertz-linewidth infrared frequency source with a long-term instability below 5×10^{-15}," *Appl. Phys. B*, pp. 1–6, 2012.

T. Kessler, C. Hagemann, C. Grebing, T. Legero, U. Sterr, F. Riehle, M. J. Martin, L. Chen, and J. Ye, "A sub-40 mHz linewidth laser based on a silicon single-crystal optical cavity," *Nature Photonics*, vol. 6, pp. 687–692, 2012.

J. K. Kim, C. Hagemann, T. Schreiber, T. Peschel, S. Böhme, R. Eberhardt, and A. Tünnermann, "Monolithic all-glass pump combiner scheme for high-power fiber laser systems," *Opt. Express*, vol. 18, no. 12, pp. 13 194–13 203, 2010.